Contribution to the identification of primary ultra high energy cosmic rays using the Pierre Auger Observatory

Ngoc Diep Pham

LAL 10-241
Décembre 2010

THÈSE

Présentée le 17 décembre 2010

par

Ngoc Diep PHAM

pour obtenir le grade de

Docteur ès Sciences
de l'Université Paris-Sud 11, Orsay

Contribution à l'identification de la nature des rayons cosmiques d'énergie extrême à l'Observatoire Pierre Auger

Soutenue devant la commission d'examen composée de :

M.	F. COUCHOT	Président
M.	P. BILLOIR	Rapporteur
M.	M.C. NGUYEN	Rapporteur
M.	P. DARRIULAT	Directeur de thèse
M.	A. CORDIER	Directeur de thèse
M.	A.K. NGUYEN	
M.	M. URBAN	

VIỆN KHOA HỌC VÀ CÔNG NGHỆ VIỆT NAM
VIỆN VẬT LÝ

BỘ GIÁO DỤC VÀ ĐÀO TẠO

LUẬN ÁN TIẾN SỸ

Bảo vệ ngày 17 tháng 12 năm 2010

bởi

PHẠM NGỌC ĐIỆP

Chuyên ngành : Vật lý năng lượng cao
Mã số : 62.44.05.05

Xác định bản chất tia vũ trụ năng lượng siêu cao sử dụng Đài thiên văn Pierre Auger

Hội đồng chấm luận án bao gồm :

Chủ tịch :	François COUCHOT	Phòng thí nghiệm LAL, Orsay
Phản biện :	Pierre BILLOIR	Đại học Paris 6 và Paris 7
	Nguyễn Mậu CHUNG	Đại học Khoa học Tự nhiên
Người hướng dẫn :	Pierre DARRIULAT	Viện KH&KT Hạt nhân Hà Nội
	Alain CORDIER	Đại học Paris-Sud 11
Thành viên :	Nguyễn Anh KỲ	Viện Vật lý Hà Nội
	Marcel URBAN	Phòng thí nghiệm LAL, Orsay

This thesis has been made under joint supervision of Professors Alain Cordier (LAL, Orsay) and Pierre Darriulat (IOP, Hanoi) following the agreement DRI/GI/AV/CJ-26/05/05 between Université Paris-Sud 11 and the Institute of Physics of Hanoi.

Cette thèse a été réalisée sous la direction conjointe des professeurs Alain Cordier (LAL, Orsay) et Pierre Darriulat (IOP, Hanoi) en application de la convention internationale de cotutelle de thèse DRI/GI/AV/CJ-26/05/05 entre l'Université Paris-Sud 11 et l'Institut de Physique de Hanoï.

Bản luận án này được thực hiện dưới dạng hợp tác đồng hướng dẫn bởi GS Alain Cordier (LAL, Orsay) và GS Pierre Darriulat (Viện Vật lý, Hà Nội) theo hợp đồng DRI/GI/AV/CJ-26/05/05 giữa Đại học Paris 11 và Viện Vật lý Hà Nội.

CONTRIBUTION TO THE IDENTIFICATION OF PRIMARY ULTRA HIGH ENERGY COSMIC RAYS USING THE PIERRE AUGER OBSERVATORY

Table of Contents

ACKNOWLEDGEMENTS

First of all, I would like to express my deepest gratitude to Pr Pierre Darriulat who is my "Vietnamese" cosupervisor. He has been spending a lot of his time guiding me and following every progress of the work of the thesis. I would say without his supervision this thesis would not be possible. His idea to make thesis in "cotutelle" is great idea, a very nice system to raise the level of PhD thesis in Vietnam.

Secondly, I am very grateful to Pr Alain Cordier and Pr Nguyễn Ái Việt who quickly supported us right after we had the idea to make the thesis in cotutelle. Being my French cosupervisor Pr Alain Cordier has supported my work and done all his best for me to save time to concentrate on the work with utmost time and effort.

I deeply thank Dr Marcel Urban for his scientific guidance; a lot of work done in this thesis had been inspired by his ideas and the work done at the Auger-LAL group. I enjoyed very much my three month stay every year in the dynamic, friendly and open working environment in his group. The colleagues from the group, Xavier Garrido, Sylvie Dagoret-Campagne, Karim Louedec, Delphine Monnier-Garaigne, Kégl Balázs and Rémi Bardenet, have been very helpful in giving me a hand each time when I had problem.

I warmly thank my colleagues at VATLY, Đỗ Thị Hoài, Phạm Thị Tuyết Nhung, Phạm Ngọc Đồng, Nguyễn Thị Thảo, Nguyễn Văn Hiệp, Phạm Tuấn Anh, Lion Alio, Đoàn Thị The, who have been working with me, gave me a lot of help and support. Their friendship is a source of encouragement for me. I am also grateful for the moral support from Dr Võ Văn Thuận, Dr Đặng Quang Thiệu, the directorial board and colleagues of the Institute for Nuclear Science and Technology where our laboratory is located.

I acknowledge constant support of the scientists from Auger Collaboration, in particular Professors Jim Cronin, Alan Watson, Pierre Billoir and Tiina Suomijärvi. I thank Dr Frédéric Fleuret (École Polytechnique) for taking the time of giving me useful explanation and information about nucleus-nucleus interactions at high energy.

I would like to thank Professors François Couchot, Nguyễn Mậu Chung and Nguyễn Anh Kỳ for accepting to be in the jury for my thesis defense, and in particular the two rapporteurs Pr Pierre Billoir and Pr Nguyễn Mậu Chung who spent a lot of time to read and comment the thesis.

I would like to thank Professors Nguyễn Như Đạt, Nguyễn Đại Hưng and their colleagues of the doctoral school at Vietnam IOP for their support. I also would like to thank colleagues from LAL who have done a lot of administrative work to make my stay at LAL very easy and pleasant.

Financial support from the World Laboratory, Rencontres du Vietnam (bourse Odon Vallet), French CNRS, Région Île-de-France, University Paris Sud, the LIA FVPPL project, Vietnam Atomic Energy Institute and Ministry of Science and Technology (the 760/2008/HD-NDT project) is gratefully acknowledged.

Finally, I am deeply grateful to my wife, my son and other members of my family who are always besides me encouraging and supporting me to do research.

RÉSUMÉ EN LANGUE FRANÇAISE

Bien que la découverte des rayons cosmiques date d'un siècle, ce n'est que récemment qu'on est parvenu à identifier leurs sources galactiques comme étant des restes de jeunes Supernovae (SNR). La difficulté était la déviation de leurs trajectoires dans le champ magnétique du disque de la Voie Lactée, empêchant d'associer leurs sources à des objets célestes connus. C'est l'astronomie en rayons gamma qui a permis de sauter cet obstacle en associant les sources de rayons gamma d'énergies supérieures au TeV à des enveloppes de jeunes SNRs.

Ces découvertes récentes n'ont toutefois pas été capables d'expliquer l'origine de la composante extra galactique des rayons cosmiques, dite d'ultra haute énergie (UHECR), ni d'identifier leurs sources et le mécanisme d'accélération. Ce n'est que tout récemment, avec la construction de l'Observatoire Pierre Auger (PAO), que la physique des UHECR est apparue sous un jour nouveau. Le PAO, avec lequel notre laboratoire est associé, et dans le cadre duquel cette thèse a été réalisée, est un immense réseau de 1600 compteurs Cherenkov (SD, pour détecteur de surface) couvrant une superficie de 3000 km^2 dans la pampa argentine. Il abrite également des détecteurs de fluorescence (FD) qui permettent une détection hybride des grandes gerbes pendant les nuits claires et sans lune. Le PAO a déjà accumulé, pour la première fois au monde, une centaine d'UHECRs d'énergies supérieures à 50 EeV dont l'étude des propriétés est ainsi devenue possible. De fait, deux résultats majeurs ont déjà été obtenus, qui marquent un jalon important dans l'étude de la physique des UHECRs: l'observation d'une coupure dans la distribution en énergie, aux alentours de 100 EeV, associée pour l'essentiel au seuil de photoproduction de pions dans les interactions des UHECRs avec les photons du fond cosmique fossile; et la mise en évidence d'une corrélation entre les directions vers lesquelles pointent les UHECRs et les concentrations de matière extragalactique de l'univers proche, en particulier la région de Cen A.

A plus basse énergie, jusqu'à une cinquantaine d'EeV, le PAO a mis en évidence une augmentation des masses primaires vers le fer quand l'énergie augmente. Cette observation se base sur des mesures de l'altitude à laquelle la gerbe atteint son développement maximal, censée être plus élevée pour les noyaux de fer que pour les protons. Toutefois, les estimations de la masse primaire basées sur la densité de muons au sol se heurtent à des incohérences entre observations et prédictions des modèles conventionnels de développement des gerbes qui empêchent de conclure.

On n'est pas encore parvenu à assembler les pièces de ce puzzle de façon claire et définitive. Une possibilité serait que les UHECR qui pointent vers des galaxies proches, comme CenA, soient des protons et que les autres soient des noyaux de fer. Mais cela reste encore à prouver. Le travail présenté dans la thèse est une contribution modeste à ce programme de recherche. Il met l'accent sur des méthodes d'identification des masses primaires basées sur la mesure de la densité des muons au sol, en particulier sur la méthode des sauts (jump method) qui a été conçue et développée au LAL d'Orsay où une partie importante de la thèse a trouvé son inspiration.

La méthode des sauts identifie la présence de sauts soudains dans les traces des FADC, formant un saut total J, avec celle de muons. La lumière Cherenkov produite par les particules de la gerbe qui traversent les détecteurs du SD est captée par des tubes photomultiplicateurs dont les signaux sont enregistrés en fonction du temps dans des convertisseurs analogue/digital rapides (FADC, 40 MHz). La relation entre le saut total, J, et les propriétés des traces des FADCs montre, en particulier, que pour avoir une chance d'apprendre quelque chose de sensé sur le nombre N_μ de muons qui contribuent à la trace du FADC, il est nécessaire de restreindre l'observation à des détecteurs qui ne soient pas trop proches de l'axe de la gerbe. Une étude séparée des traces induites par des muons et par des électrons ou photons montre que J est approximativement proportionnel à N_μ et à Q (la charge totale), ce qui n'est pas surprenant. En combinant des traces de muons et d'électrons/photons on trouve que J peut être décrit par une expression de la forme $J=\{(43.9\pm0.5)10^{-3}Q+(200\pm2)N_\mu\}10^{-3}$.

Nous étudions ensuite la séparation entre primaires légers (protons) et lourds (fer) à laquelle on peut s'attendre de la mesure des valeurs de J dans les compteurs touchés par la gerbe. Nous remarquons que même si nous connaissions N_μ exactement (ce qui bien sûr n'est pas le cas) la séparation entre fer et proton ne dépasserait pas les 30%, ce qui donne une mesure de la corrélation entre la nature des primaires et la densité des muons au sol. Ceci implique que l'identification des primaires à un niveau de confiance correspondant à trois déviations standard requiert un minimum de cinquante détecteurs dans lesquels on puisse mesurer la valeur prise par J. Une autre remarque est que si l'on connaissait l'énergie des primaires, ce qui n'est pas le cas, non seulement J mais aussi Q et N_J (le nombre de saut dans chaque trace) seraient de bons discriminants entre fer et protons.

Ceci dit, l'énergie des primaires étant inconnue, l'inversion de la relation $J=AQ+BN_\mu$ en $N_\mu=\alpha J+\beta Q$ – dans le but de déduire N_μ de Q et J – n'est pas aussi simple qu'il y paraît. Le problème est que la corrélation qui lie Q à J est si forte qu'il n'y a essentiellement rien à gagner de l'utilisation de la forme binomiale ci-dessus. Un corollaire important de cette forte corrélation est la difficulté qu'il y a à faire la différence entre deux gerbes induites par des protons d'énergies différentes et deux gerbes d'énergies égales, l'une induite par un proton et l'autre par un noyau de fer. Afin de surmonter cette difficulté, il est nécessaire d'utiliser des discriminants indépendants de l'énergie. Deux outils sont utilisés dans ce but : l'utilisation du rapport J/Q comme discriminant et la restriction de l'analyse aux compteurs situés dans une fourchette de distances à l'axe de la gerbe dépendant de $S(1000)$ (la densité au sol de la gerbe à 1 km de son axe, utilisée comme mesure de l'énergie de la gerbe). Des gerbes simulées sont utilisées pour démontrer qu'en principe chacun de ces deux outils est efficace.

Une analyse indépendante de l'énergie est ensuite appliquée à l'étude des gerbes détectées par le PAO, confirmant leur désaccord avec les prédictions des modèles de développement des gerbes et établissant un nouveau et important résultat: ce désaccord ne peut pas être résolu par un simple ajustement de la relation entre $S(1000)$ et l'énergie.

Enfin, la méthode des sauts est appliquée aux UHECRs pointant à 18^o près vers Cen A. Contrairement à une autre analyse utilisant des données hybrides pour

étudier le taux d'élongation, cette analyse préfère une origine protonique pour les gerbes associées à Cen A par rapport à celles pointant ailleurs dans le ciel.

Tout ceci illustre la difficulté qu'il y a à identifier la nature des primaires à partir des données du SD. Le désaccord entre données et prédictions constitue un problème majeur qu'il faut à tout prix résoudre. On ne saurait se satisfaire d'une explication rejetant sur les modèles hadroniques la responsabilité du désaccord si les mécanismes physiques incriminés ne sont pas clairement identifiés. Les programmes de simulation utilisés de façon courante sont d'une complexité telle qu'il est difficile de les utiliser dans ce but. Le souci de reproduire au plus près la réalité physique les a rendus opaques. La seconde partie de la thèse se propose de faire un pas dans la direction de l'élaboration d'un code de simulation simplifié mais transparent dans l'espoir qu'il permette d'éclairer le problème.

La simulation de la composante électromagnétique des grandes gerbes est relativement simple: il suffit, à une excellente approximation, de ne retenir que le rayonnement de freinage et la création de paires comme seuls mécanismes élémentaires et d'ignorer toute particule autre que photon, électron ou positon. Il est aussi facile de décrire les pertes d'énergie par ionisation, ce qui permet un traîtement particulièrement simple du développement de la gerbe qui est présenté et commenté en détail. On obtient ainsi des paramétrisations du profil longitudinal de la gerbe utilisant la forme de Gaisser-Hillas et les valeurs moyennes des paramètres sont évaluées en fonction de l'énergie en même temps que leurs fluctuations. Trois types de primaires sont pris en considération: électrons, photons et pions neutres. Le modèle, par itérations successives, permet d'atteindre simplement aux énergies les plus élevées. Son application à l'effet Landau-Pomeranchuk-Migdal et à l'effet Perkins permettent d'illustrer son efficacité et de montrer que ces deux effets sont, en pratique, d'incidence négligeable sur la physique des UHECRs.

Le développement de la composante hadronique de la gerbe est beaucoup plus difficile à traîter. Il implique la production de muons, essentiellement des pions, dont la composante neutre est purement électromagnétique et par conséquent facile à décrire. Au contraire, le destin des pions chargés dépend de deux processus en compétition: interactions hadroniques avec les noyaux de l'atmosphère et désintégrations faibles en une paire muon-neutrino. Les échelles qui gouvernent ces deux processus sont différentes: la section efficace d'interaction ne dépend que peu de l'énergie mais le taux d'interaction dépend de la pression atmosphérique, c'est-à-dire de l'altitude; au contraire, le taux de désintégration est indépendant de l'altitude mais inversement proportionnel à l'énergie à cause de la dilatation de Lorentz. La méthode itérative utilisée avec tant d'efficacité pour la composante électromagnétique, pour laquelle la longueur de radiation est la seule échelle pertinente, n'est plus praticable.

Le problème essentiel de l'extrapolation des données d'accélérateurs aux grandes gerbes d'UHECRs n'est pas tant l'énergie que la rapidité. De fait, 20 EeV dans le laboratoire correspondent à 200 TeV dans le centre de masse, seulement deux ordres de grandeur au dessus des énergies du Tevatron et un seul au dessus des énergies du LHC. La lente évolution de la physique hadronique en raison directe du logarithme de l'énergie rend peu probable qu'une extrapolation des données des collisionneurs vers les énergies des UHECRs soit grossièrement erronée. Par

contre, en termes de rapidité, les gerbes UHECR sont dominées par la production vers l'avant, une région inaccessible aux collisionneurs. En particulier, il n'existe aucune mesure précise des inélasticités et de la forme du front avant du plateau de rapidité, toutes deux essentielles au développement des gerbes UHECR. Le modèle développé dans la thèse fait de l'inélasticité un paramètre ajustable et la forme du plateau de rapidité est accessible de façon transparente.

Une attention particulière est consacrée aux caractéristiques de la gerbe qui permettent l'identification de la nature des primaires, noyaux de fer ou protons. Ceci concerne essentiellement la première interaction: une fois que le noyau primaire a interagi, le développement de la gerbe ne met plus en jeu que des interactions nucléon-air ou méson-air. Là encore, il n'existe pas de données de collisionneurs permettant de décrire les interactions de noyaux et de pions avec l'atmosphère dans le domaine d'énergie qui nous intéresse. Le modèle utilisé ici permet un accès facile et transparent aux paramètres pertinents.

La présentation qui est donnée du modèle limite ses ambitions à en décrire les traits essentiels, laissant pour une phase ultérieure l'étude de la densité des muons au sol. L'accent est mis sur le développement de ce nouvel outil et sur son adéquation aux problèmes qu'il entend aborder mais son utilisation dépasse le cadre de la thèse et fera l'objet d'études ultérieures.

TÓM TẮT LUẬN ÁN BẰNG TIẾNG VIỆT

Mặc dù đã một thế kỷ qua từ khi tia vũ trụ được phát hiện nhưng chỉ mới gần đây người ta mới xác định được nguồn phát của những tia vũ trụ có nguồn gốc thiên hà. Đó là tàn dư các vụ nổ siêu sao. Những tia vũ trụ này có năng lượng thấp nên quỹ đạo của chúng bị bẻ cong nhiều bởi từ trường do vùng đĩa thiên hà sinh ra khiến cho việc xác định nguồn phát của chúng với các thiên thể đã biết trở nên rất khó khăn. Bước tiến của vật lý tia vũ trụ có được nhờ đột phá của ngành thiên văn học tia gamma, với những đột phá mới người ta xác định được lớp vỏ của các tàn dư vụ nổ siêu sao là nguồn phát tia gamma năng lượng lớn trên TeV.

Tuy nhiên, những tiến bộ trong hiểu biết về tia vũ trụ có nguồn gốc thiên hà cũng chưa đủ để chúng ta có thể hiểu rõ về những tia có nguồn gốc ngoài thiên hà: nguồn phát cũng như cơ chế gia tốc Tia vũ trụ Năng lượng Siêu cao (TVTNLSC). Chỉ mới gần đây, cùng với việc xây dựng Đài thiên văn Pierre Auger (PAO), vật lý TVTNLSC mới có những bước tiến mới. Hiện chúng tôi đang hợp tác Đài thiên văn Pierre Auger và những nghiên của luận án được thực hiện trong khuôn khổ hợp tác này. PAO có một hệ thống đề-tếc-tơ khổng lồ bao gồm 1600 bình đếm Cherenkov nước (hệ đề-tếc-tơ bề mặt), bao phủ trên diện tích 3000 km^2 đặt trên cao nguyên Ác-hen-ti-na. Đài thiên văn vận hành một hệ ghi đo kép bao gồm dãy đề-tếc-tơ bề mặt và đề-tếc-tơ huỳnh quang, mặc dù hệ đề-tếc-tơ huỳnh quang có độ tiếp nhận nhỏ hơn đáng kể so với hệ đề-tếc-tơ bề mặt. PAO đã thu nhận được vài trăm TVTNLSC có năng lượng lớn hơn 50 EeV, đó là một mẫu thống kê TVTNLSC lớn nhất từ trước tới nay, qua đó lần đầu tiên cho phép nghiên cứu tính chất của chúng. Thực tế, Đài thiên văn Pierre Auger đã thu được hai kết quả quan trọng tạo nên bước đột phá trong nghiên cứu TVTNLSC, đó là: khẳng định cắt ngưỡng phân bố năng lượng, trong vùng 100 EeV, do TVTNLSC mất năng lượng khi tương tác với Bức xạ Phông nền Vũ trụ (CMB) sinh ra các hạt pion; và cung cấp bằng chứng về mối tương quan giữa vùng vật chất ngoài thiên hà và hướng đến của các TVTNLSC. Đặc biệt là bằng chứng rõ ràng về mối tương quan với vùng của Cen A.

Tại vùng năng lượng thấp, nhỏ hơn 50 EeV, PAO đưa ra bằng chứng chứng tỏ khối lượng của TVTNLSC có xu hướng nghiêng về phía khối lượng nặng hơn tại vùng năng lượng lớn hơn. Quan sát này dựa trên việc đo độ dày khí quyển tại đó sự phát triển mưa rào tia vũ trụ đạt giá trị cực đại. Những tia sơ cấp có khối lượng nặng hơn (hy vọng chủ yếu là hạt nhân sắt) có vị trí mưa rào phát triển cực đại ở độ cao cao hơn so với proton. Tuy nhiên, những ước lượng dựa vào mật độ muon trên mặt đất lại không thể đưa ra kết luận cuối cùng về vấn đề này vì có sự chênh lệch đáng kể giữa thực nghiệm và dự đoán từ các mô hình phát triển mưa rào tương tác mạnh truyền thống.

Gộp tất cả những điều trên lại, bí ẩn về bản chất TVTNLSC vẫn chưa có lời giải đáp rõ ràng và tin cậy. Một khả năng có thể là các TVTNLSC có hướng đến từ các thiên hà gần, đặc biệt là Cen A, là các hạt proton còn những tia còn lại là hạt nhân nguyên tố sắt. Những nghiên cứu của luận án này đóng góp một phần khiêm tốn vào vấn đề bản chất TVTNLSC. Để xác định khối lượng hạt sơ cấp, chúng tôi tập trung vào những phương pháp phân tích dựa trên mật độ muon trên mặt đất, đặc biệt dựa trên phương pháp gọi là "phương pháp bước nhảy" được phát triển tại LAL–Orsay nơi mà nhiều công việc của luận án bắt nguồn từ đó.

Phương pháp bước nhảy dựa vào sự xuất hiện của những thay đổi đột ngột tín hiệu trong vết của bộ chuyển đổi tương tự số nhanh (FADC). Giá trị bước nhảy tổng, J, của tất cả những thay đổi được dùng để xác định sự xuất hiện của muon. Ánh sáng Cherenkov sinh ra bởi các hạt thứ cấp khi đi vào các bình đếm Cherenkov nước được các ống nhân quang điện ghi nhận. Tín hiệu thu nhận được từ các ống nhân quang điện được các FADC ghi lại sau mỗi 25 ns. Nghiên cứu mối quan hệ giữa tổng bước nhảy J và đặc điểm vết của FADC cho thấy để có thể tìm hiểu về số muon N_μ đóng góp vào vết FADC thì phải giới hạn nghiên cứu tới những bình đếm không quá gần trục mưa rào. Từ nghiên cứu về vết của muon và elelectron/photon cho thấy J xấp xỉ tỉ lệ với N_μ và Q (điện tích tổng của vết). Kết hợp vết FADC của muon và elelectron/photon cho thấy có thể khớp J dưới dạng $J=\{(43.9\pm0.5)10^{-3}Q+(200\pm2)N_\mu\}10^{-3}$.

Chúng tôi nghiên cứu đại lượng phân biệt bản chất tia sơ cấp sử dụng J của những bình đếm nhận được tín hiệu từ mưa rào sinh ra bởi proton và sắt. Chú ý rằng, thậm chí khi biết số muon N_μ một cách chính xác (tất nhiên thực tế không thể có điều này) sự khác biệt giữa mưa rào proton-sắt cũng không bao giờ vượt quá 30%. Giá trị này phần nào phản ánh độ lớn mối tương quan giữa bản chất tia vũ trụ sơ cấp và mật độ muon trên mặt đất. Do đó, để kết luận về bản chất tia vũ trụ sơ cấp với độ tin cậy tới ba độ lệch chuẩn đòi hỏi phải có mẫu đo ít nhất gồm 50 bình đếm. Nếu biết năng lượng của tia vũ trụ sơ cấp thì không chỉ J mà cả Q và N_J (số bước nhảy trong một vết) cũng có thể dùng để phân biệt proton và sắt một cách khá tốt.

Tuy nhiên, thực tế ta không biết chính xác năng lượng của tia sơ cấp, biến đổi từ hệ thức $J=AQ+BN_\mu$ thành $N_\mu=\alpha J+\beta Q$ – với mục đích tính số muon N_μ từ Q và J – là không rõ ràng. Vấn đề ở chỗ Q và J tương quan lớn với nhau và do đó ta không thu thêm được thông tin gì khi sử dụng dạng nhị thức bao gồm cả hai đại lượng này. Hệ quả quan trọng của mối tương quan lớn này là, rất khó có thể phân biệt được hai mưa rào proton có năng lượng khác nhau và hai mưa rào proton và sắt cùng năng lượng. Để vượt qua trở ngại này, việc sử dụng tham số phân biệt không phụ thuộc vào năng lượng là bắt buộc. Với mục đích đó chúng tôi sử dụng hai công cụ: dùng J/Q làm tham số phân biệt và giới hạn việc phân tích của mình với những bình đếm nằm trong khoảng cách đến trục mưa rào phụ thuộc vào $S(1000)$ (mật độ của mưa rào trên mặt đất tại khoảng cách 1 km từ trục mưa rào, đại lượng dùng để xác định năng lượng của mưa rào). Sử dụng số liệu mô phỏng chúng tôi chỉ ra rằng sự hoạt động của hai công cụ này rất thành công.

Phân tích độc lập với năng lượng sau đó được áp dụng với số liệu thực của PAO, nghiên cứu đã khẳng định sự không phù hợp giữa số liệu thực nghiệm và dự đoán từ mô hình mô phỏng và khẳng định một kết quả mới quan trọng: sự không phù hợp này không thể giải quyết bằng cách thay đổi tỷ lệ mối quan hệ giữa $S(1000)$ và năng lượng một cách đơn giản được.

Cuối cùng, phân tích dùng phương pháp bước nhảy sử dụng kiến thức thu được từ những nghiên cứu trên được áp dụng cho các mưa rào TVTNLSC bắt nguồn từ Cen A trong phạm vi 18^o. Khác với một phân tích khác sử dụng số liệu tốc độ phát triển dọc của mưa rào từ bộ số liệu ghi nhận đồng thời bởi cả hai loại đề-tếc-tơ, phân tích của chúng tôi khẳng định những tia vũ trụ đến từ Cen A có khối lượng nhẹ gần với proton hơn khi so với khối lượng trung bình của các tia đến từ toàn bộ bầu trời.

Phân tích sử dụng số liệu của đề-tếc-tơ bề mặt minh họa cho sự khó khăn trong việc xác định bản chất tia vũ trụ sơ cấp. Sự bất đồng giữa số liệu và mô phỏng là một nỗi lo thực sự và cần có nhiều nghiên cứu hơn để giải quyết vấn đề này. Ta không thể thỏa mãn với việc đổ lỗi cho các mô hình sử dụng trong các chương trình mô phỏng mà phải hiểu rõ cơ chế vật lý đóng vai trò trong việc gây ra sự bất đồng. Những chương trình mô phỏng phát triển mưa rào sử dụng theo truyền thống thường phức tạp và thiếu sự rõ ràng làm cho người dùng khó có thể xác định một cách đáng tin cậy các hiện tượng liên quan. Phần còn lại của luận án chúng tôi xây dựng một chương trình mô phỏng phát triển mưa rào tia vũ trụ, khá thô sơ nhưng rõ ràng với mong muốn nhờ đó có thể phần nào làm sáng tỏ bất đồng giữa mô phỏng và thực nghiệm.

Thành phần điện từ của mưa rào được xử lý tương đối đơn giản: với mức độ xấp xỉ tốt, để mô hình một cách đơn giản sự mất năng lượng do iôn hóa, có thể coi bremsstrahlung và tạo cặp là các quá trình cơ bản của mưa rào điện từ và bỏ qua tất cả các hạt có thể sinh ra trong mưa rào trừ electron, positron và photon. Với việc đơn giản hóa này cho phép xử lý ngay được sự phát triển dọc của mưa rào, phần này được trình bày chi tiết và thảo luận trong luận án. Các tham số của mưa rào, cả giá trị trung bình và *rms* của chúng, được tham số hóa theo năng lượng tia sơ cấp sử dụng hàm Gaisser-Hillas. Ba loại tia sơ cấp được xem xét là electron, photon và pion trung hòa. Mô hình này cho phép làm việc với các mưa rào năng lượng siêu cao một cách đơn giản. Để minh họa cho sự tiện lợi này, chúng tôi áp dụng chương trình mô phỏng mưa rào điện từ cho hiệu ứng Landau-Pomeranchuk-Migdal và hiệu ứng Perkins với kết luận rằng cả hai hiệu ứng này thực tế đều nhỏ không đáng kể.

Sự phát triển thành phần tương tác mạnh của mưa rào khó xử lý hơn nhiều. Nó liên quan đến những sản phẩm thứ cấp là các hạt meson, chủ yếu là pion, số phận của chúng được quyết định bởi hai quá trình cạnh tranh nhau: tương tác mạnh với hạt nhân trong khí quyển và phân rã yếu thành các hạt muon. Tỷ lệ điều khiển hai quá trình này khác nhau: tiết diện tương tác phụ thuộc vào năng lượng một cách tương đối yếu nhưng tốc độ tương tác lại phụ thuộc vào áp suất khí quyển, hay độ cao; ngược lại, tốc độ phân rã không phục thuộc vào độ cao nhưng tỉ lệ nghịch với năng lượng (kết quả của việc dãn thời gian Lorentz). Điều này ngăn cản việc sử dụng phương pháp lặp rất hiệu quả trong trường hợp điện từ, ở đó chỉ có chiều dài bức xạ điều khiển động học của mưa rào.

Vấn đề chính trong việc ngoại suy số liệu máy gia tốc cho mưa rào TVTNLSC về mặt năng lượng không lớn hơn nhiều so với vấn đề về rapidity. Thực tế trong hệ quy chiếu phòng thí nghiệm 20 EeV tương ứng với 200 TeV trong hệ quy chiếu khối tâm, chỉ hơn hai bậc so với năng lượng của Tevatron và một bậc so với năng lượng của LHC. Sự tiến triển chậm của vật lý tương tác mạnh theo *logs* khiến việc ngoại suy số liệu gia tốc đối chùm năng lượng thấp tới vùng năng lượng TVTNLSC không thể quá sai. Nhưng dưới dạng rapidity, thành phần đi thẳng (forward production) trong mưa rào TVTNLSC chiếm ưu thế lại là thành phần không truy cập được từ số liệu từ máy gia tốc. Đặc biệt, không có phép đo chính xác nào về độ phi đàn tính (inelasticity) và hình dạng phần suy giảm của phổ phân bố rapidity mà cả hai yếu tố này lại ảnh hưởng nhiều nhất đến sự phát triển của mưa rào TVTNLSC. Mô hình phát triển trong luận án này lấy độ phi đàn tính là một

tham số có thể thay đổi được và hình dạng của phân bố rapidity có thể tiếp cận một cách rõ ràng.

Quan tâm đặc biệt được giành cho những đặc điểm cho phép xác định tia vũ trụ sơ cấp, proton hoặc sắt. Việc xác định này chủ yếu liên quan đến tương tác đầu tiên: sau tương tác đầu tiên của tia sơ cấp tương tác, sự phát triển của mưa rào chỉ liên quan đến tương tác nucleon-không khí và meson-không khí. Tại vùng năng lượng của TVTNLSC lại một lần nữa, chưa có số liệu thực nghiệm về tương tác giữa các hạt nhân và những tương tác tiếp theo như pion-hạt nhân cũng không hề có số liệu thực nghiệm. Những miêu tả hết sức đơn giản sử dụng trong chương trình mô phỏng của chúng tôi cho phép tiếp cận đến các tham số liên quan một cách dễ dàng.

Việc trình bày công việc ở phần này trong luận án giới hạn tham vọng trong việc miêu tả và thảo luận về mô phỏng, còn phần nghiên cứu mật độ muon trên mặt đất sẽ là công việc cho giai đoạn sau. Điều quan trọng ở đây là chúng tôi đã xây dựng nên được một công cụ phù hợp tốt với nhiệm vụ, nhưng để thực hiện nhiệm vụ đó vẫn nằm ngoài phạm vi thực hiện của luận án, và đó sẽ là chủ đề nghiên cứu trong tương lai.

Chapter 1

INTRODUCTION

While there has been a century since the first discovery of cosmic rays, it is only recently that their galactic sources have been identified as young Supernova Remnants (SNR). The difficulty is the bending of cosmic rays in the magnetic field of the disk of the Milky Way, preventing the identification of the sources with known celestial objects. The breakthrough was the advent of gamma ray astronomy, which made it possible to identify the sources of gamma rays having energies in excess of a TeV as being the shells of young SNRs. The link between cosmic rays and gamma rays was provided by neutral pions produced in the interaction of cosmic rays with the interstellar medium in the environment of their sources, followed by their prompt two-photon decay. Several such SNRs have been identified and their high resolution X-ray images have been compared with gamma ray data, confirming their association and establishing young SNRs as the main, possibly single, source of galactic cosmic rays. Moreover, the observation that cosmic rays have their sources in the shells of such SNRs rather than in their centre has given strong support to Diffusive Shock Acceleration (DSA) being the most likely mechanism of acceleration.

These recent discoveries have been unable to clarify the understanding of the extra galactic component of Ultra High Energy Cosmic Rays (UHECR), to identify their sources and to reveal the mechanism of acceleration. The size of existing gamma ray observatories does not allow for the detection of UHECR induced gamma rays, the rate of which is far too small (the UHECR flux is ~1 particle par km^2 per century above 20 EeV). However, if DSA was to subsist as the acceleration mechanism in the UHECR domain, it had become clear that it would require shocks and confinement volumes – size times magnetic field – much larger than those occurring in SNRs, suggesting Active Galactic Nuclei (AGN) and possibly Gamma Ray Bursts (GRB) as the most likely source candidates.

It was not until very recently, with the construction of the Pierre Auger Observatory (PAO), that new light could be shed on the physics of UHECR. The PAO, with which our laboratory is associated, and in the framework of which the present work has been made, is a huge array of 1600 Cherenkov counters, covering 3000 km^2 in the Argentinean pampas. It also includes Fluorescence detectors allowing for hybrid detection, albeit with significantly lower acceptance. The PAO has already collected some hundred UHECRs having energies in excess of 50 EeV, a sample of unprecedented size that allows, for the first time, a study of their properties. Indeed two major results have been obtained, that represent a breakthrough in UHECR physics: the observation of a cut-off in the energy distribution, in the 100 EeV region, essentially associated with pion photoproduction in the interaction of UHECRs with the Cosmic Microwave Background (CMB); and evidence for a correlation between nearby extragalactic matter (at distances not exceeding 75 Mpc) and the directions toward which UHECRs (energies in excess of 60 EeV) are pointing.

The latter implies a comparison with existing galaxy catalogues. In particular, with respect to the most recent AGN catalogue, some 38±7% of the selected UHECRs point to such an AGN within 3.1^{o} while 21% are expected for an isotropic distribution. The correlating fraction was nearly twice as high in 2007, 69±12%, which can only be explained by a large statistical fluctuation. There is clear evidence for an important correlation with the Cen A region.

At lower energies, up to some 50 EeV, the PAO has given evidence for a trend toward higher primary masses when the energy is increased. This observation rests on measurements of the atmospheric depth of the maximum of the shower development (the so-called elongation rate), which is expected to occur at higher altitudes for massive primaries than for protons. However, estimates based on the muon density on ground are inconclusive because they face a significant mismatch between observations and the predictions of conventional hadronic shower development models. Finally, an important comment is that there exist serious arguments suggesting that in the UHECR region, nuclei other than iron and hydrogen should be rare.

Putting all this together makes a puzzle that has not yet received a clear and reliable answer. A possibility is that UHECRs that are seen to point to nearby galaxies, in particular to Cen A, are protons while those that are not are iron nuclei. Indeed, fully ionized iron nuclei are expected to suffer too much bending in the magnetic field of the disk of the Milky Way to allow for an association with their sources. Whatever the explanation, more data and more studies are required in order to answer the questions that are now in front of us.

The present work is a modest contribution to this research program. It focuses on methods relying on the ground muon density for the identification of the primary masses, in particular on the so-called “jump method” that has been developed at LAL-Orsay where part of the present work has found its inspiration. It is organized in six chapters, including the present introduction.

Chapter 2 is an introduction to cosmic ray physics, with emphasis on UHECRs as studied by the PAO. After some generalities on cosmic rays, the main features of the PAO are briefly described and the present status of the identification of the primaries is reviewed.

Chapter 3 is devoted to the jump method. A critical study of its content and of its power at discriminating between iron and proton primaries is presented. The dependence on energy of jump analyses is discussed and an energy-independent analysis is performed, excluding that the mismatch mentioned above between measured and predicted muon densities on ground be the result of a shift in the energy scale.

Chapters 4 and 5 describe simulations that have been made of the shower development mechanism in the spirit of providing simplified but transparent tools for their study. The motivation is the desire to understand what is causing the mismatch between observations of the muon density on ground and the predictions of sophisticated models available in the literature. Chapter 4 concentrates on the development of electromagnetic showers. It implies only two processes, pair creation and bremsstrahlung, and two types of particles, electrons and photons. This simplicity allows for an easy parameterization of the mean longitudinal shower

profile and of its fluctuations. The model is applied to the Landau-Pomeranchuk-Migdal effect and to the Perkins effect, both of which are found of little impact on the UHECR region.

Chapter 5 addresses the much more difficult problem of the development of hadronic showers. The details of the simulation are presented and discussed. The model suffers of many unknowns: the UHECR domain is unexplored by accelerator experiments. The energy domain is one to two orders of magnitude above what current colliders can explore; most collisions are pion-proton rather than proton-proton and essentially no high energy pion-proton data exist; forward production dominates UHECR physics while central production dominates collider physics; finally, UHECR interactions imply nuclei, mostly nitrogen in the atmosphere and possibly iron as primaries, for which no accelerator data are available in the desired energy range. The task of exploiting the simulation model that we have developed is still ahead of us but some preliminary results are presented, illustrating the main features.

Finally a summary and some concluding remarks are presented in Chapter 6.

Chapter 2

COSMIC RAY STUDIES AT THE PIERRE AUGER OBSERVAROTY

2.1 Generalities on cosmic rays

2.1.1 A brief history

At the end of the XIXth century, scientists were puzzled by the spontaneous discharge of their electroscopes, suggesting that some kind of an ionizing radiation was present on Earth. In 1909, Wulf, on the Eiffel tower, noted that the discharge rate was decreasing with altitude. Between 1911 and 1913 the Austrian physicist Viktor Hess (Figure 2.1) performed balloon measurements reaching up to five kilometres in altitude and established the existence of an "unknown penetrating radiation coming from above and most probably of extraterrestrial origin". He shared the 1936 Nobel Prize with Carl Anderson.

In the following years cosmic rays became the subject of intense research, in particular with Millikan (who coined the name in 1925) and Anderson at Pikes Peak. In 1927 the measurement of the east-west asymmetry and of the dependence of the rate on latitude established unambiguously that cosmic rays were charged particles, not photons. In 1938, Pierre Auger (Figure 2.1), using counters in coincidence, discovered extensive air showers (EAS) and understood that they were produced by very high energy (up to at least 10^{15} eV) primaries interacting with the Earth atmosphere.

In the thirties and forties, when accelerators were not yet dominating the scene, cosmic rays became the laboratory for the study of particle physics. Anderson (Figure 2.1) discovered the positron in 1932 and the muon in 1938. Powell and Occhialini discovered the pion in 1947. Then came strange particles: kaons, hyperons and many others. In the fifties, accelerators took over and cosmic rays got studied for their own sake.

For many years following, major effort was devoted to the study of cosmic rays, trying to understand their origin. Ground detectors and large arrays and fluorescence telescopes reached very high energies (John Linsley at Volcano Ranch saw the first 10^{20} eV shower in 1962). Space astronomy has been a break through for the study of low energy cosmic rays, in particular solar energetic particles. A recent example of space measurements in solar astronomy is the NASA's Advanced Composition Explorer which was launched in 1997 to the Lagrange point between Sun and Earth.

In the past 20 years, spectacular progress in astrophysics and long time scales implied in the construction of very high energy accelerators have caused a renaissance of interest in cosmic rays physics under the name of astroparticle physics. In particular TeV gamma ray detectors have been constructed and operated. Their main asset is that they can point to the sources without suffering deflections from magnetic fields.

To study cosmic rays, a new generation of ground detectors was born. Plans to use the whole Earth atmosphere as a radiator observed from space are being implemented and neutrino astronomy is currently being pioneered.

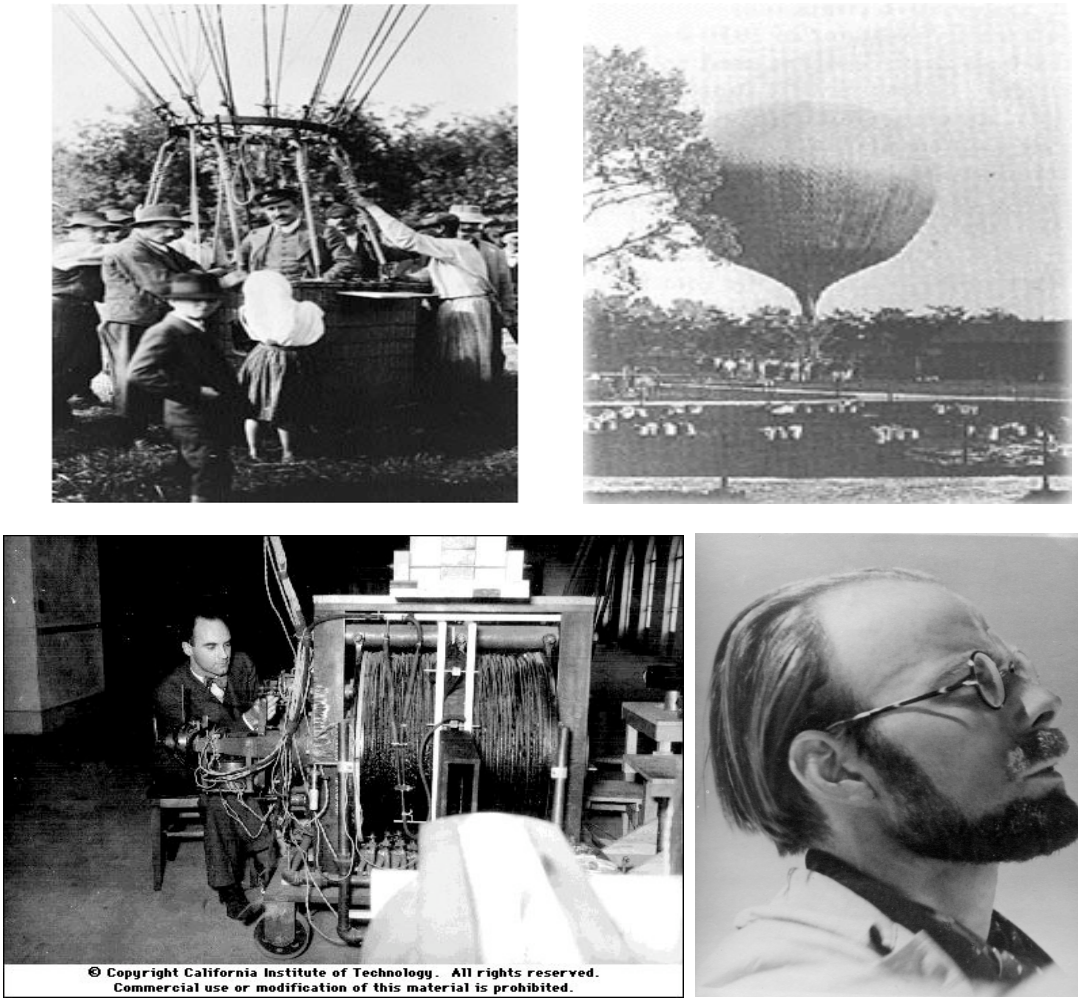

Figure 2.1: The pioneers: Viktor Hess and his balloon (upper panels), Pierre Auger at the Jungfraujoch (lower right), and Anderson with his cloud chamber (lower left).

2.1.2 The main features

Cosmic rays are ionized nuclei that travel in space up to extremely high energies of the order of 10^{20} eV = 16 Joules. There are very few of them but their contribution to the energy density of the Universe is similar to that of the CMB or of the visible light or of the magnetic fields, namely ~1 eV/cm^3. Their power law energy spectrum (Figure 2.2), spanning 32 decades (12 decades in energy), is of the approximate form $E^{-2.7}$.

Whenever they have been measured, cosmic rays abundances are similar to elemental abundances observed in their environment, suggesting that they have been accelerated from interstellar matter. As in any galactic environment, hydrogen and helium dominate, even-even nuclei are naturally favoured and the iron region, which corresponds to the strongest nuclear binding, is enhanced. The main

difference is that the valleys are now filled by spallation reactions on the matter encountered by the cosmic ray during its journey in the interstellar medium, ~7 gcm^{-2} on average.

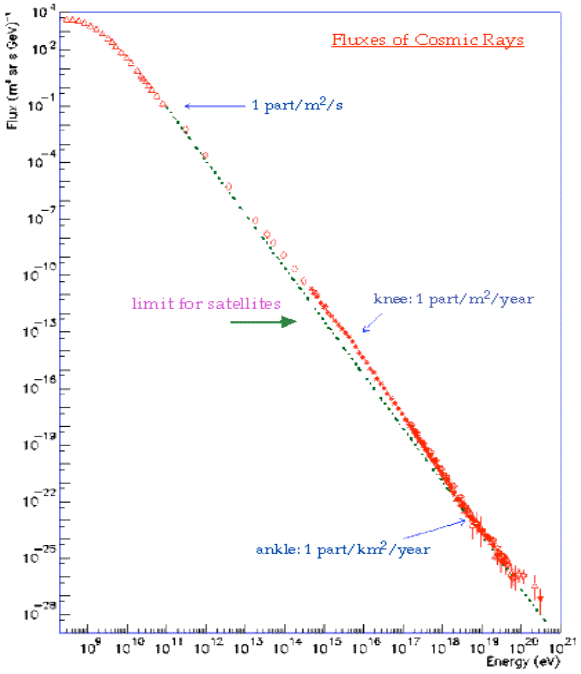

Figure 2.2: The cosmic ray energy spectrum displaying its main features.

While the very low energy part of the cosmic rays spectrum is of solar origin, most of it does not reach the Earth, which is shielded by its magnetic field. The bulk of the energy spectrum on Earth corresponds to an energy density of ~10^{-12} erg/cm^3. Most of it must have a galactic origin because of the magnetic trapping in the Milky Way disk with a galactic escape time of ~3 10^6 y. The cosmic rays power amounts therefore to some ~10^{-26} erg/cm^{3}s which can be compared with the power delivered by SN explosions, ~10^{-25} erg/cm^3 (~10^{51} erg/SN and ~3 SN explosions per century in the disk). Namely cosmic rays carry some 10% of the power delivered by SN explosions.

It is only in the higher energy part of the spectrum that an extra galactic component can be found. Its energy density is estimated to some 2 10^{-19} erg/cm^3 implying a power of ~10^{37} erg/Mpc^3/s. Both active galactic nuclei (AGN) and gamma ray bursts (GRB) stand, from the point of view of energy, as possible sources.

2.1.3 Galactic sources

Particles coming from the Sun reach up to a few MeV and are mostly associated with solar activity and flares. Coronal mass ejections and resulting interplanetary shocks are similarly correlated. On the contrary, galactic cosmic rays are anticorrelated as solar activity increases the Earth magnetic field which acts as a shield.

Contrary to cosmic rays, gamma rays travel straight in the universe and point back to their sources. They are good at detecting the high energy decay photons coming from neutral pions produced in the interaction of very high energy cosmic rays with interstellar matter. Gamma ray astronomy (Figure 2.3) has shown that several sources have an X ray counterpart identified as an SNR (Figure 2.4) and has established this way that most galactic cosmic rays are likely to originate from SNRs.

Figure 2.3: The High Energy Stereoscopic System (HESS, Namibia) includes four telescopes at the corners of a 120×120 m^2 square, operating above 100 GeV. Its field of view is 5^o and its resolution a few arc minutes. To take a picture of the Crab takes only 30 seconds.

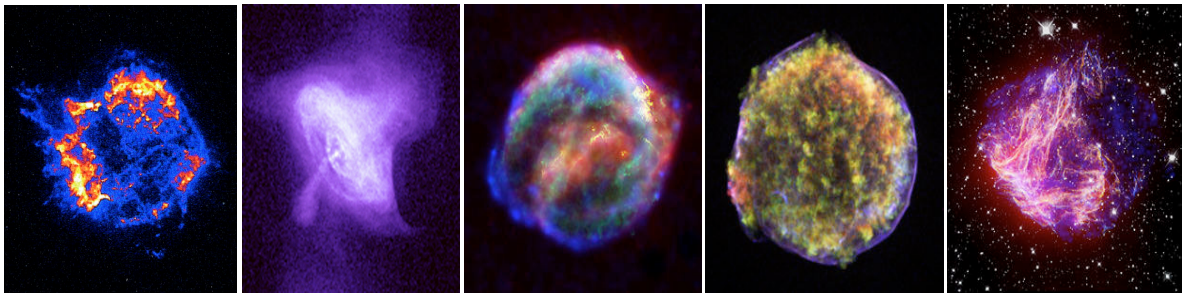

Figure 2.4: Very high resolution X ray images of SNRs (Chandra). From left to right: Cassopieia A, the Crab, Kepler (SN 1604), Tycho (SN 1572) and N49.

There exist two main types of SNRs: Ia and II. Type Ia occurs when a white dwarf, member of a binary, accretes matter from its companion until it reaches the Chandrasekhar mass limit of 1.4 solar masses. The core is fully burned; the SNR shell is nearly empty. Type II occurs when a massive star collapses into a neutron star that remains in the centre, possibly detected as a pulsar, the wind of which gives energy to the remnant (one speaks of a plerion).

Figure 2.5 is an early illustration of the correlation observed between high energy γ rays and X-rays emitted by an SNR source [1], establishing that they come from the shell. The main features of SNR shell structures are reasonably well

understood: the explosion blast wave sweeps up the inter-stellar matter (ISM) in the forward shock. As mass is swept up, the forward shock decelerates and ejecta catch up. Then, the reverse shock heats the ejecta and nuclear reactions produce new heavy elements. Once enough mass has been swept up the SNR enters the so called Sedov phase and slowly dilutes in the ISM. While thermal particles and magnetic field are concentrated in the shell, relativistic particles extend to much larger distances and synchrotron emission is confined to magnetic field regions. The shock structure depends on the SNR age.

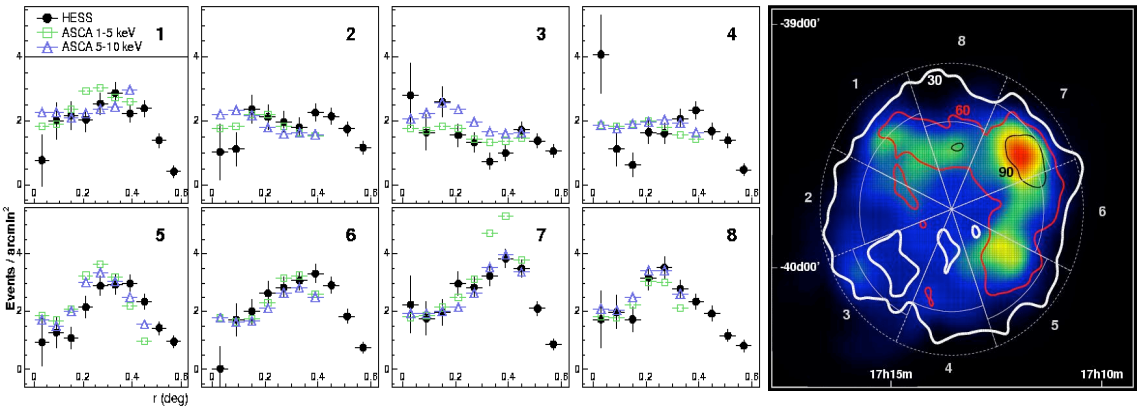

Figure 2.5: Comparison of radial intensity profiles measured in X-rays (ASCA) and γ rays (HESS) in separate octants of SNR RX J1713. The overall correlation coefficient between the two radial distributions is 80%.

2.1.4 Diffusive shock acceleration

The identification of SNRs as sources of galactic cosmic rays has given support to an acceleration mechanism, called diffusive shock acceleration, which is now accepted as the most likely candidate for accelerating cosmic rays. As in a cyclotron the particle is accelerated locally on traversing the shock (equivalent of the gap between the cyclotron dees) and is guided by magnetic fields on either side in such a way as to come back to the shock (equivalent of the cyclotron dipole guide field). However both the acceleration and guiding processes are very different from the cyclotron case. Guiding is provided by stochastic collisionless scattering on magnetic turbulences.

Acceleration is best described in the upstream or downstream frame where the particle happens to be. In such frames, the particle is at rest with respect to the magnetic fields and its energy is therefore conserved. However, whenever – after random walk magnetic bending – the particles returns to the shock and crosses it it gains energy. Indeed, both media move toward each other with a large relative velocity V_{shock}. Each time a cosmic ray particle returns to the shock and crosses it, with the same energy as it had when it last left the shock, it acquires an energy ΔE with $\Delta E/E=V_{shock}/c$ where c is the light velocity. The time between successive encounters is $\Delta t=kE$, with k a constant, and the escape probability, marking the end of the acceleration process, is equal to V_{shock}/c (as is $\Delta E/E$). Calling r the shock compression ratio (the ratio between upstream and downstream densities), the

energy spectrum takes the form $dN/dE \approx E^{-\alpha}$ with $\alpha=(r+2)/(r-1)$. For monatomic gases, $r=4$ and $dN/dE \approx E^{-2}$. The prediction of a power spectrum, with an index not too different from that observed, is a major success of the model.

Quantitatively, good results have been obtained after it had been realized that the magnetic fields in the shock region are much stronger than was originally thought. There exists indeed copious evidence in favour of strong magnetic turbulences and magnetic field amplification in the shock region of young SNRs. For example, RX J1713 (Figure 2.6) shows a variable shock structure implying strong turbulences and magnetic field amplification [2]. Important variations are detected as a function of time, zones of turbulence becoming quiet and conversely on a few years time scale. Evidence for magnetic field amplification is obtained from the ratio of radio to TeV emission as a same distribution of electrons produces synchrotron (radio, X-ray) and TeV Inverse Compton (IC) but synchrotron depends directly on field while IC and pion decays do not. Shock front compression is a revelator of field amplification. Magnetic fields are enhanced by factors of up to hundred, much larger than the factor of 4 associated with the compression factor of an ideal hydrodynamic shock. For example, in Cass A, one observes a strong front compression implying a magnetic field level of 500 μG instead of the 10 μG expected otherwise [3].

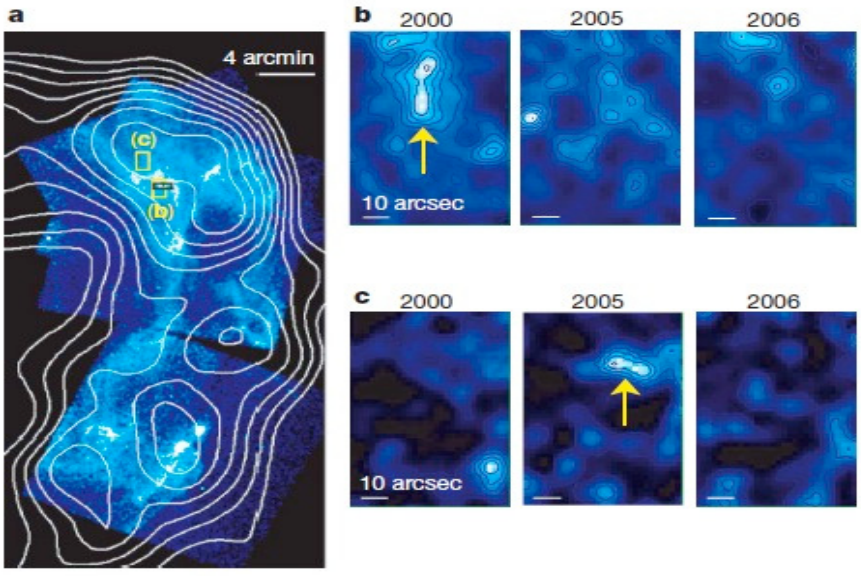

Figure 2.6: Evidence for time varying turbulences in the shell of RX J1713.

Cosmic rays and the magnetized plasma carry similar energy densities: they do interact on each other. Accelerated particles tend to stream ahead upstream, which causes the generation of streaming instabilities and makes the evolution non linear, resulting in a strong amplification of the mean field: the structure of the shock is modified by cosmic ray retroaction. The higher field, in turn, depresses IC with respect to synchrotron emission, implying faster scattering and increased maximum momentum.

Sharply peaked X-rays at forward shock are evidence that the field is large and increases sharply at the shock, implying that diffusive shock acceleration is efficient and nonlinear at SNR outer blast wave shocks. Older remnants do not show such field amplification: the excitation of turbulences decreases with shock velocity, while damping (by non-linear wave interactions and ion-neutral collisions) does not.

2.1.5 Extra galactic sources

Only the higher energy UHECRs are expected to point to their sources within a few degrees but this expectation rests on the assumption that extragalactic magnetic fields do not exceed a fraction of microGauss, which is a priori by no means certain. Their uniform distribution in the sky would then be evidence for their extragalactic origin (otherwise they would cluster around the disk of the Milky Way).

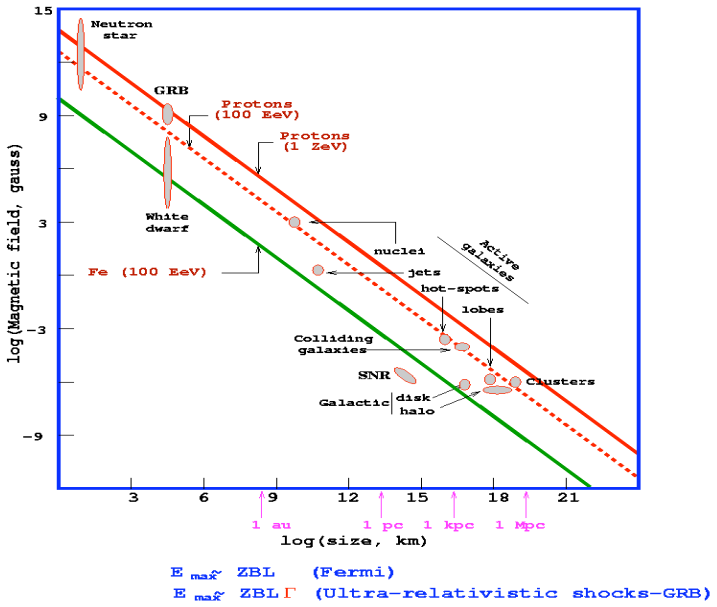

Figure 2.7: Hillas plot for protons (red lines) at 10^{20} eV (dashed) and 10^{21} eV (full). The green line is for 10^{20} eV iron. The size (km) is in abscissa and the field (Gauss) in ordinate.

Very general arguments [4] limit the possible UHECR acceleration sites to a very few. The argument is that, whatever the acceleration mechanism (it is obviously true in the case of diffusive shock acceleration), the product of the size of the site by its mean magnetic field must exceed some value to contain the orbits. This is illustrated in Figure 2.7 that shows as possible acceleration sites AGNs, their jets and radio lobes, GRBs, magnetars (neutron stars having extremely high magnetic fields) and colliding galaxies. For the mechanism of diffusive shock acceleration to be valuably extended to extragalactic cosmic rays, one needs much larger shock sites than provided by SNRs, such as present in colliding galaxies (Figure 2.8).

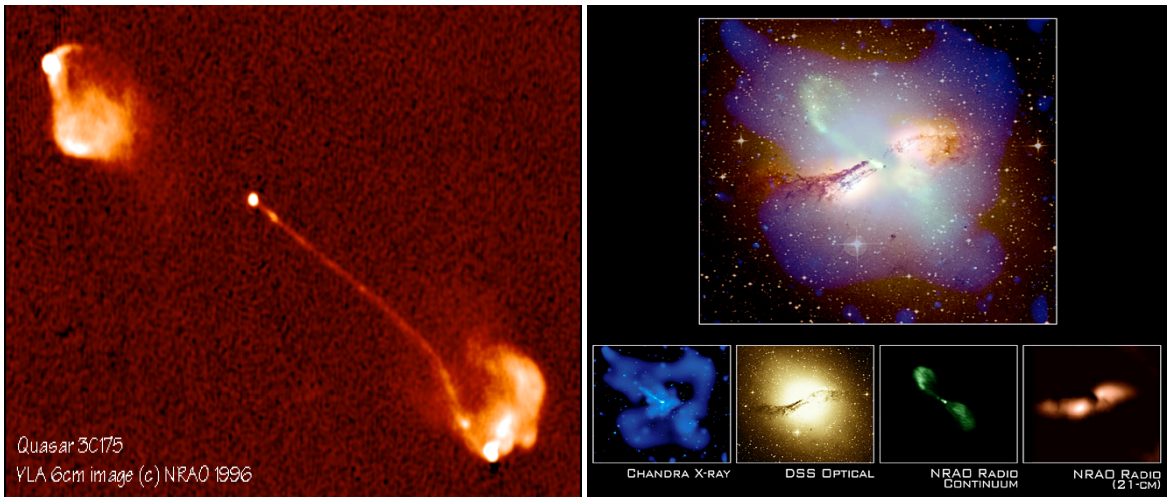

Figure 2.8: Left: Radio image of a quasar. Right: Centaurus A, merging of an elliptical galaxy with a smaller spiral, has an AGN in its centre (the AGN closest to us) and is the site of large shocks.

Recent observations and studies of colliding galaxies and merging galaxy clusters suggest that these were common phenomena in the early denser Universe. Such collisions are now believed to have played an important role in the process of galaxy formation. Galaxy collisions usually do not imply direct star collisions but the strongly increased gravity field enhances the collapse of hydrogen clouds and the formation of new stars, many of which being very massive and therefore having a short life time. Galaxy collisions are sites of very violent events on large scales and are therefore most probably sites of large shocks. AGNs also, in particular their jets, are possible sites for UHECR acceleration. Until recently, it had not been possible to do cosmic rays astronomy because the images of the sources were blurred by magnetic fields. The coming into operation of the Pierre Auger Observatory (PAO) has now made it possible.

2.2 The Pierre Auger Observatory

2.2.1 General description

The Pierre Auger Observatory (PAO) is a hybrid detector covering 3000 km^2 where showers are detected from the fluorescence they produce in atmosphere and by their impact on a ground detector array (Figure 2.9). Its aim is to measure the properties of ultra-high energy cosmic rays (UHECR), i.e. cosmic rays having energy in excess of 1 EeV (10^{18} eV), in particular the angular and energy dependence of their flux and their mass composition, and to elucidate the question of their origin and of the mechanism of acceleration [5, 6].

Construction of the baseline design was completed in November 2008. With stable data taking starting in January 2004, the world's largest data set of cosmic ray observations had been collected already during the construction phase of the Observatory.

When a primary cosmic ray enters the Earth atmosphere, it interacts with it and produces a large number of mesons which, in turn, interact with the atmosphere, and so on until the primary energy is exhausted in ionization losses. The result is a cascade of interactions (Figure 2.10) producing an extensive air shower (EAS). Their longitudinal profile evolves slowly with energy, in proportion to its logarithm, while its energy content, in the form of ionization losses, is proportional to energy.

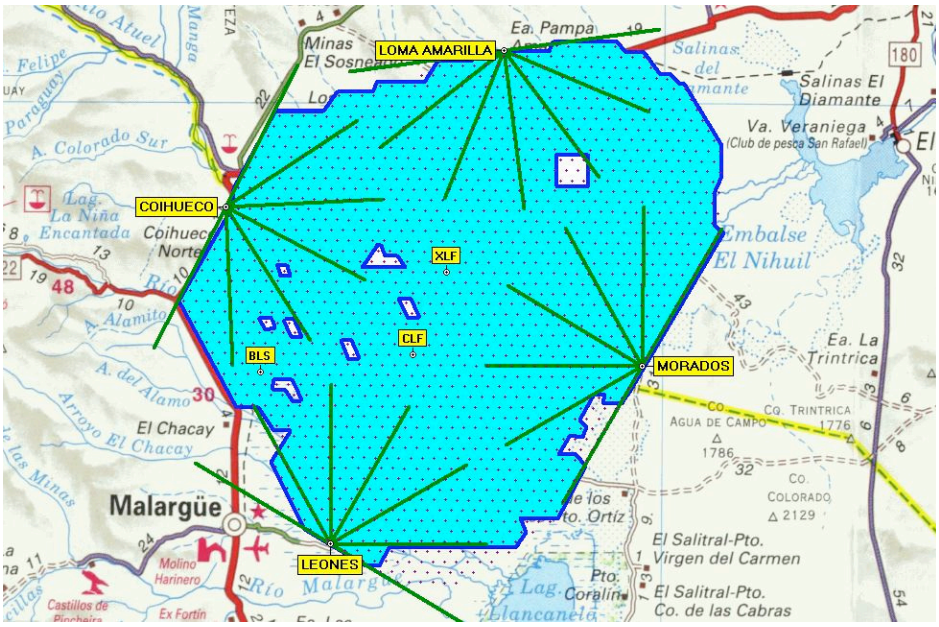

Figure 2.9: Plan view of the PAO.

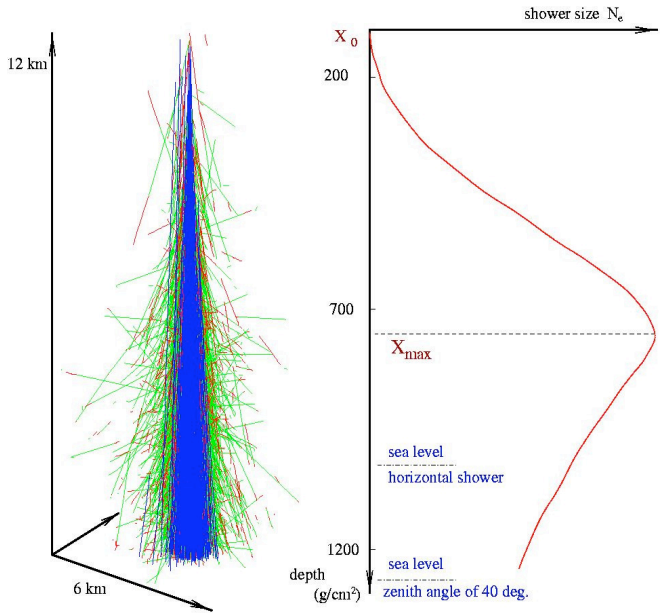

Figure 2.10: Longitudinal development of an extensive air shower [7].

A major fraction of the mesons produced are pions, either neutral or charged. The former decay promptly into two photons and are therefore lost for the development of the hadronic cascade. They generate instead electromagnetic showers consisting mostly of electrons, positrons and photons and developing longitudinally at the scale of a radiation length, twice as short as the interaction length which governs the development of the hadronic cascade. The charged pions will have a chance to decay into a muon-neutrino pair if their decay length, 56 m/GeV, is short enough in comparison with the interaction length. As a result, the muon to electron/photon ratio increases with depth.

Around 30 EeV, the UHECR flux is about 0.2 $km^{-2}century^{-1}sr^{-1}EeV^{-1}$ and drops rapidly at higher energies, implying a very large coverage, but the showers contain billions of particles when reaching ground and cover several square kilometers, allowing for a thin sampling [8]. The PAO covers 3000 km^2 in the Argentinean pampas, of which only 5 ppm are covered by detectors. These include 1600 Cherenkov detectors making up the surface detector (SD), and 24 fluorescence telescopes making up the fluorescence detector (FD). Data are transferred by radio to an acquisition centre which filters them and sends them out for subsequent dispatching to the laboratories associated with this research, including VATLY in Ha Noi.

The SD is described in detail in the next section.

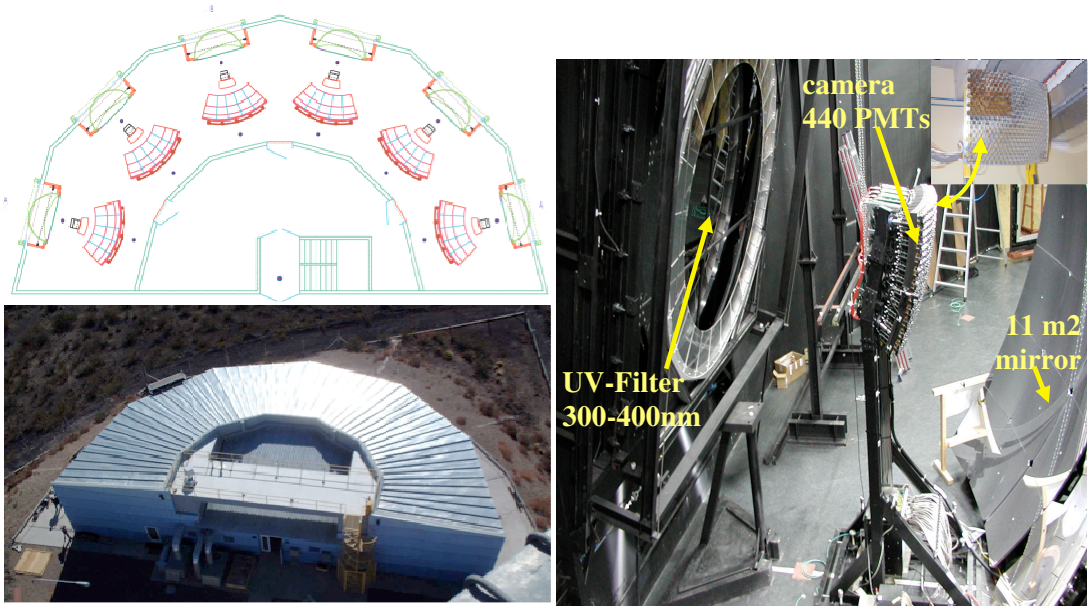

Figure 2.11: Left: A fluorescence station: schematic view (on top) and its photograph. Right: Photograph of an eye.

The FD is organized in four stations of six telescopes each, which overlook the PAO area (Figure 2.11). They measure the fluorescence light (near UV) produced in the interaction between the shower charged particles and the nitrogen molecules of the atmosphere. They can only operate during clear moonless nights, which implies a duty cycle of 13%. Each telescope covers a field of view of 30^o in azimuth and 28.6^o in elevation. After having been filtered, the light is reflected by a

concave mirror onto an array of 440 hexagonal PMT pixels. In principle, a single telescope is sufficient to measure the direction of the shower axis from the measurement of the times at which each pixel is hit. But, in practice, a precise measurement requires either binocular detection or, less demanding, the simultaneous detection of the time at which at least one of the ground Cherenkov detectors has been hit by the shower [9, 10]. The energy is measured from the longitudinal profile [11] which, when accurately and fully measured, provides a direct calorimetric evaluation of the shower energy (the energy carried away by neutrinos and muons penetrating in ground is of the order of 10% and does not much fluctuate from shower to shower). However, in practice, this measurement is difficult: it implies a good knowledge of the air transparency and of the atmospheric Cherenkov light contamination and, most of the time, the shower is only partly contained in the field of view.

2.2.2 The surface detector

The SD samples the footprint of the showers on ground. It is made of a triangular array of water Cherenkov counters having a mesh size of 1.5 km deployed on flat ground at an altitude of 1400 meters above sea level, near the maximum of shower development for the highest energy vertical UHECRs. When reaching ground, showers consist essentially of low energy electrons, positrons and photons as well as of muons having a kinetic energy of a few GeV. In both water Cherenkov counters and scintillator plates, the muon signal is proportional to track length; on average, when averaging over the detector section normal to the direction of incidence, the signal is therefore proportional to the detector volume independently from the angle of incidence. On the contrary, electrons and photons produce small showers at radiation length scale that are fully contained in a water Cherenkov counter but only partially in a scintillator plate. The net result is that they provide a sky coverage twice as large as would be obtained with an array of scintillator plates.

When shower particles are detected in at least three counters, the measurement of the time at which they are hit allows for a precise measurement of the azimuth and zenith angle of the shower axis accounting for the slight curvature of the shower front [12].

The energy measurement is indirect but much easier than in the FD case. It implies the construction of a standard function [12], called lateral distribution function (LDF), which gives the average signal measured in a Cherenkov tank as a function of shower energy, distance to the shower axis and zenith angle. The zenith angle dependence is evaluated under the hypothesis of an isotropic cosmic ray flux. The energy is essentially measured by the normalization of the measured signals to the standard LDF at a distance of 1000 meters from the shower axis (one calls it *S(1000)*).

The choice of such a reference is dictated by two scales: the tank spacing, 1.5 km, and the size of the shower detectable footprint on ground, which increases only slowly, logarithmically, with energy. In practice the influence of the former is dominant. The final energy scale is calibrated [13] using FD data in hybrid events

as illustrated in Figure 2.12. Figure 2.13 summarizes the information gathered by the SD [6], showing both the footprint of the shower on ground and the fit to the LDF. Figure 2.14 shows the first four-fold hybrid event recorded in May 2007 with all FD stations active.

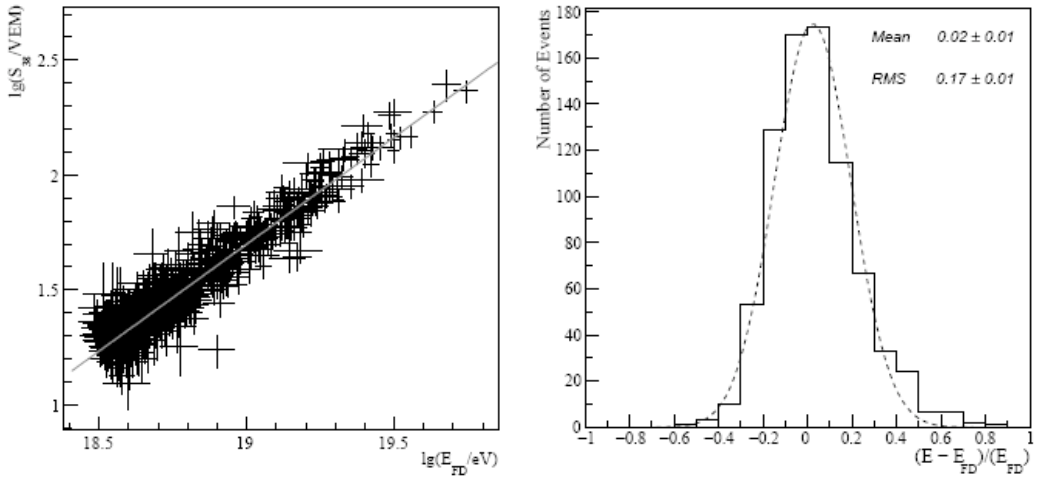

Figure 2.12: Left: Correlation between the decimal logarithms of the energy measured in the FD (abscissa) and of the normalization (ordinate) of the measured SD signals to the value of *S(1000)* (referred to 38° zenith angle for technical reasons) for the 795 hybrid events used in the fit. The line represents the best fit. Right: Fractional difference between the calorimetric energy, E_{FD}, and the energy estimate of the surface detector, *E*, obtained by the calibration curve, for the 795 selected events.

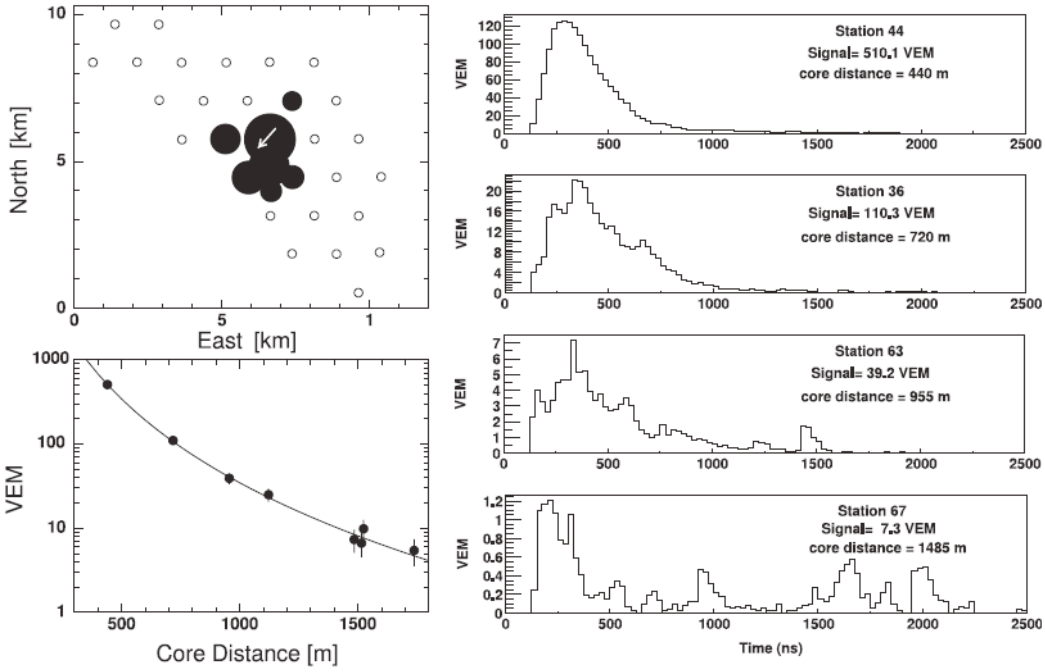

Figure 2.13: Event 211377: a typical event of about 5x10^{18} eV: Top left: The top view of triggered tanks. Lower left: The fit to the LDF. Right: FADC traces from four detectors. The signal sizes are in units of VEM (see Section 2.2.3).

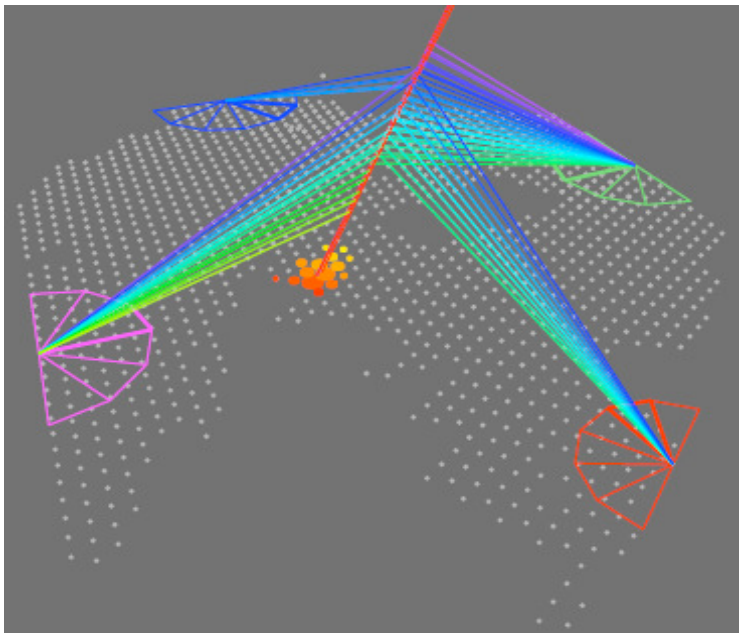

Figure 2.14: The first four-fold hybrid event.

2.2.3 Cherenkov tanks

Each Cherenkov counter is made of a resin tank shaped to host a cylindrical volume of ultra pure water, 1.2 m in height and 3.6 m in diameter (Figure 2.15). The water is contained in a highly diffusive plastic bag fitting closely in the resin tank and the Cherenkov light produced in the water volume is seen by three 9" spherical photocathode photomultiplier tubes (PMT) through high transparency windows. The PMTs are not shielded from the Earth magnetic field but are all oriented in a same way meant to maximize their response [14]. The amplification chain of each PMT is made in two parts: a central foil dynode and a standard linear focus chain of seven dynodes. The charge collected from the last dynode is amplified in such a way as to exceed the anode charge by a factor 32. Both are read under 50 Ω in 10 bits 40 MHz flash analog to digital converters (FADC). The very high dynamical range implied by the steep slope of the LDF near the shower core results in occasional saturation of the dynode signal.

Energy calibration is constantly monitored by recording locally low energy atmospheric muons inbetween triggers. As such muons are mostly relativistic and feed through the tank, their charge spectrum is essentially a replica of the distribution of track lengths across the water associated with the proper (typically cosine square) zenith angle distribution. As small zenith angle muons are an important fraction of the total, they produce a peak in the charge distribution which is used to monitor the energy scale (Figure 2.16).

The unit used is called VEM for Vertical Equivalent Muon and corresponds to the charge associated with a vertical relativistic muon impinging in the centre of the tank. The calibration of the muon peak displayed in Figure 2.16 in terms of VEM units was done once for all using a scintillator hodoscope bracketing a Cherenkov tank from above and below.

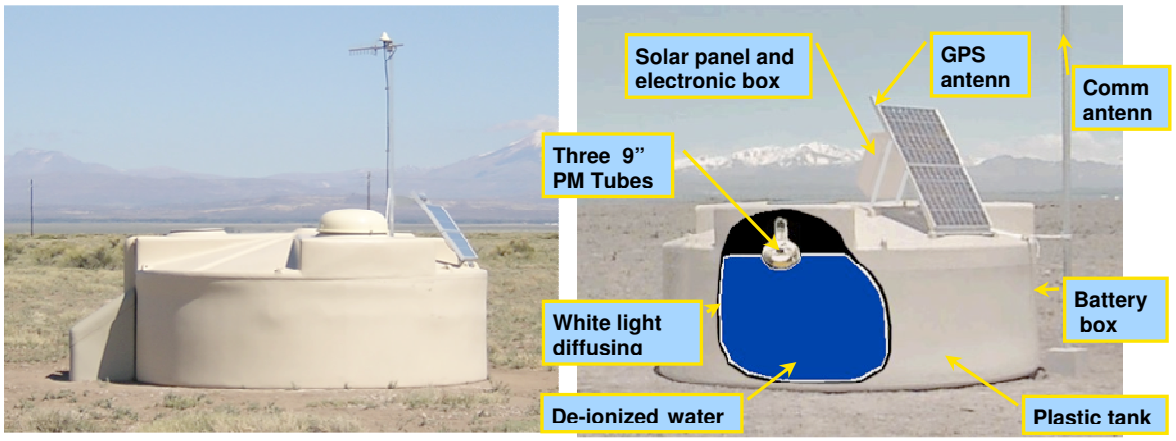

Figure 2.15: Photograph of a Cherenkov tank on site (left panel) and exploded view (right panel).

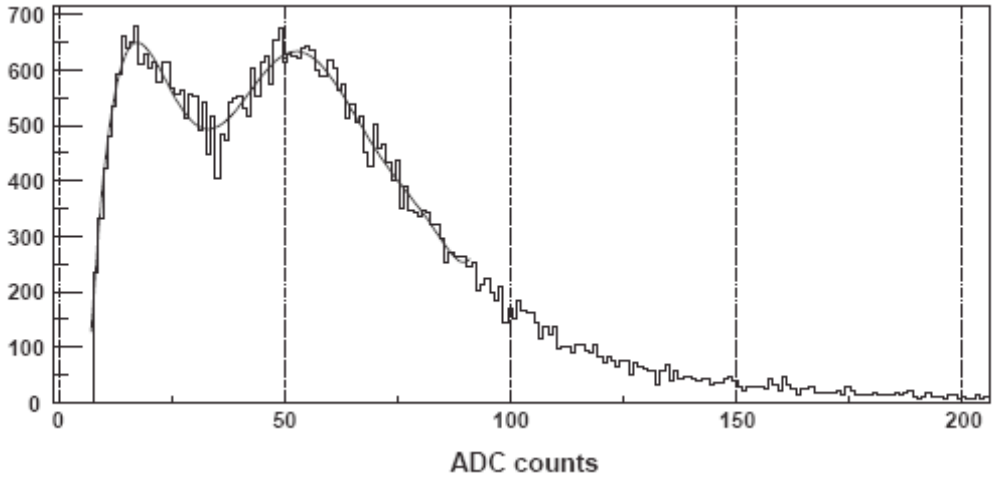

Figure 2.16: Histogram of signals from one PMT in one of the stations of the SD. The peak due to single muons is clearly visible at around 50 ADC channels. The peak at about 20 channels is artificial and is due to the cut made in plotting the data.

Low level triggers are produced locally by each station whenever some conditions are satisfied, such as a three-fold coincidence of signals exceeding 1.75 VEM or a two-fold coincidence of signals exceeding 0.2 VEM per bin in at least 13 FADC bins within a 3 μs window. The main trigger is built centrally from the first level triggers received from the stations by requiring coincidences in time and in space, the latter being done using a hierarchy of concentric hexagons. Higher level triggers have been designed this way to suppress random coincidences and to provide a trigger efficiency close to unity for showers having energy in excess of $10^{18.5}$ eV.

The electronics in each tank is powered using solar panels feeding a 12 V battery and the data are transferred to the central data acquisition system in the 7 GHz band.

2.2.4 Simulations

Analyzing SD data often requires the help of simulations reproducing the shower development and/or the detector response.

The latter is in principle straightforward but, in practice, quite complex. It requires a good knowledge of the water transparency and liner diffusivity (Lambertian and specular) as a function of wave length, of the quantum efficiency of the photocathode, again as a function of wave length, of the collection efficiencies at the first and second dynodes as a function of photon impact, of the PMT gains, of the electronic and thermal noises, of the after-pulsing characteristics, etc [15]. Much effort has been dedicated in the PAO collaboration to produce adequate codes [16].

The former, however, addresses an energy range in which the characteristics of the hadronic interactions of nuclei, baryons and mesons with air are unknown. One needs to rely on hypotheses, some of which are highly conjectural. To quote a few: the adequacy of the Glauber model to mimic nucleus-nucleus interactions, the extrapolation to higher energies of total cross-sections, rapidity and transverse momentum distributions, inelasticities, multiplicities, particle compositions (including resonances) of baryon-air and meson-air interactions, etc. In addition to these fundamental problems, a technical difficulty results from the very large number of shower particles, which precludes following each of them individually in a Monte Carlo code [17, 18]. In order to cope with the need to keep computer time within reasonable limits, various techniques have been developed, such as parameterization of some shower components or the "thinning" method, which consists in following, in a well controlled way, only part of the shower particles. Moreover, a same shower may be used many times by simply changing the location of its impact on ground with respect to the detector array, thereby providing a large sample of simulated events. However, in such a case, attention must be paid to the fact that such simulated events are not at all statistically independent. For example, if the shower starts at significantly lower altitude than average, it has important consequences on several of its properties of relevance to studies of the mass composition of the primary: ignoring it would strongly bias the results of the analysis.

General programs are available to simulate extensive air showers. In particular, CORSIKA [19] and AIRES [20] offer general frames that can accommodate a number of hadronic interaction models. It has been used to generate a library of proton and iron showers covering the energy range from 10^{17} to 10^{20} eV and a range of zenith angles between 0^{o} and 70^{o}.

2.2.5 Energy spectrum and the GZK cut-off

The PAO has already given two particularly important contributions to the physics of UHECRs. One is the evidence for the so-called GZK cut-off, the other is the observation of a correlation between the direction of arrival of the highest energy UHECR and nearby galaxies.

For some time, the differential spectral index of the energy spectrum has been known to change at ~ 3 10^{15} eV from 2.7 to 3.0, this is referred to as the knee, and again back to 2.7 near the upper end of the spectrum, this is referred to as the ankle. The latter is often attributed to the transition from galactic to extra galactic sources, although some models accommodate extra galactic origins below the ankle. Sensible scenarios can be produced which reproduce the data.

Of particular relevance to such scenarios are the interactions of cosmic rays with the cosmic microwave background (CMB), producing either electron-positron pairs or new mesons. Of these, the pion photoproduction threshold is of particular importance and causes the so-called Greisen-Zatsepin-Kuzmin (GZK) cut-off at the end of the spectrum, from the name of the physicists who first predicted the effect [21]. Until recently, the existence of such a cut-off was controversial but the Pierre Auger Observatory has settled the issue and given evidence for it. With a typical interaction length in the few 10 Mpc scale, cosmic rays coming from larger distances cannot make it to the Earth without interacting, and therefore loose energy: their flux is significantly damped and only nearby (<100 Mpc) sources can contribute to the UHECR spectrum.

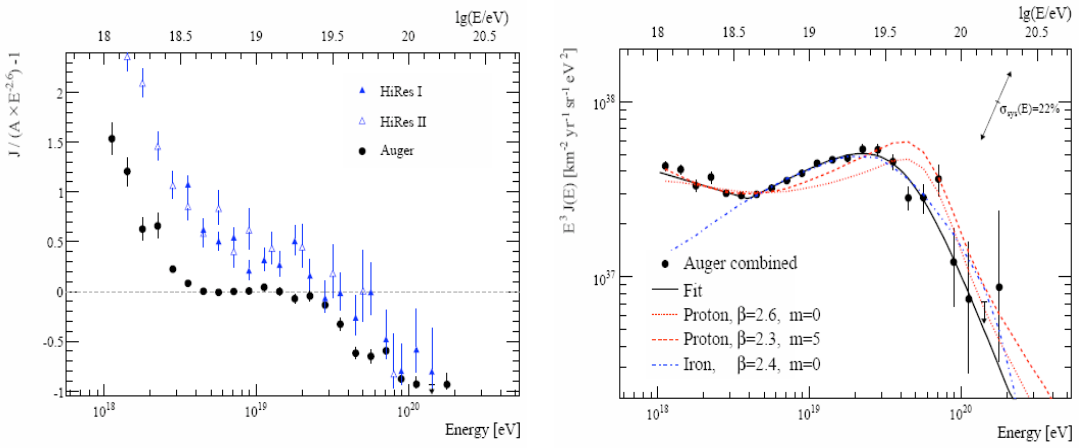

Figure 2.17: Left: Fractional difference between the combined energy spectrum of the Pierre Auger Observatory and a spectrum with an index of 2.6. Data from the HiRes instrument [23] are shown for comparison. Right: Combined energy spectrum compared with several astrophysical models including a pure composition of protons (red lines) or iron (blue line).

The most recent PAO data [22], combining both SD and FD data, are illustrated in Figure 2.17 showing the fractional difference of the spectrum with respect to an assumed flux of spectral index 2.6. Two spectral features are evident: an abrupt change in the spectral index near 4 EeV (the "ankle") and a more gradual suppression of the flux beyond about 30 EeV corresponding to the GZK cut-off.

2.2.6 Correlations with astronomical sources

The large UHECR statistics accessible to the PAO has revealed a correlation with extragalactic counterparts [24]. Of relevance to this study is the fact that the

nearby universe (100 Mpc radius), in which detected UHECRs are confined by the GZK cut-off, is highly inhomogeneous (Figure 2.18). Selecting UHECR having an energy in excess of 6 10^{19} eV and comparing the direction in the sky where they come from with a catalogue of nearby (< 75 Mpc) galaxies, revealed a clear correlation (Figure 2.19). Both numbers corresponded to values giving the best statistical significance to the observed correlation and were in agreement with reasonable expectations based on favoured estimates of the galactic and extra galactic magnetic fields for the former, and on the size of the GZK horizon for the latter. There was an even better correlation with nearby AGNs (of which, however, there exists no complete catalogue). The correlation disappeared when including lower energy cosmic rays (pointing accuracy) or farther away galaxies (GZK cut-off).

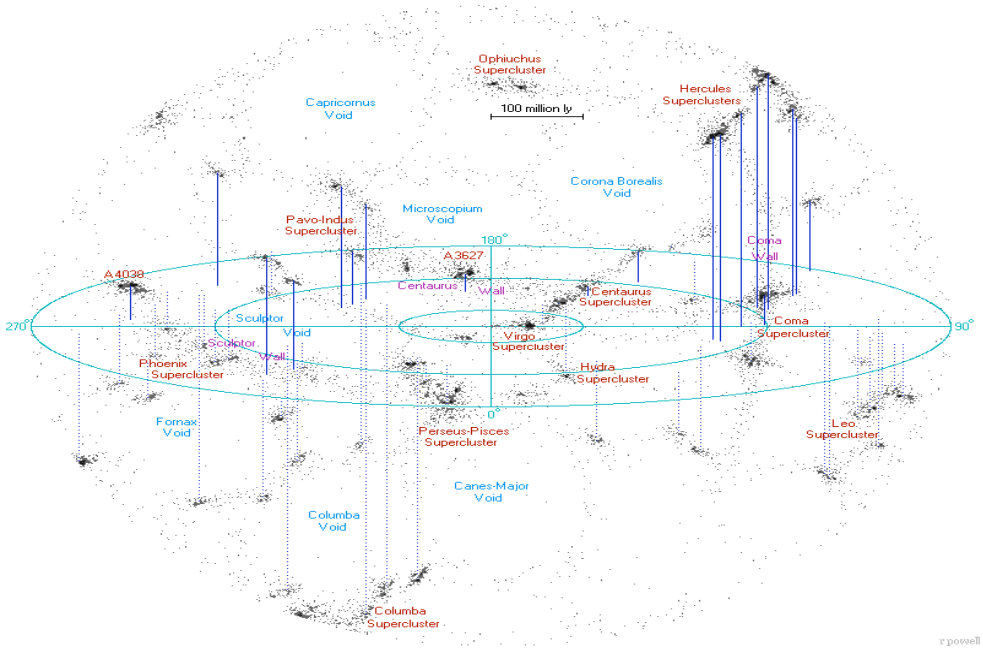

Figure 2.18: The nearby Universe.

An update of these data has been presented recently [25], including data collected through 31st March, 2009 and corresponding to an exposure of 17040 km^2 sr yr (±3%), nearly twice the former value. There are now 31 additional events above the energy threshold of 55 EeV. The systematic uncertainty on energy is ~22% with a resolution of ~17% while the angular resolution of the arrival directions is better than 0.9^o. During the period reported earlier, 18 out of 27 events arrive within 3.1^o of an AGN in the VCV catalogue [26] with redshift less than 0.018 while of the 31 additional events, 8 have arrival directions within the prescribed area of the sky, not significantly more than the 6.5 events that are expected to arrive on average if the flux were isotropic: the degree of correlation with objects in the VCV catalogue has decreased with the accumulation of new data, as clearly illustrated in Figure 2.20.

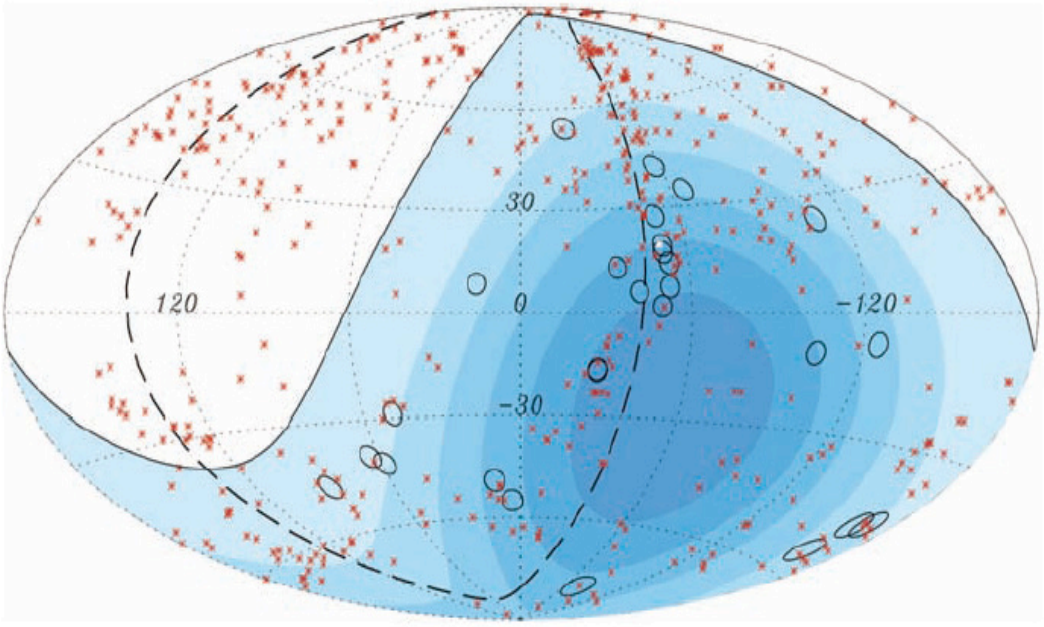

Figure 2.19: Circles of 3.1° are drawn around 27 UHECR detected by the PAO up to year 2007 [22]; red crosses are 472 AGN (318 in field of view) having *z<0.018* (*D<75*Mpc). The solid line shows the field of view (zenith angle < 60°) and the colour tells the exposure. The dashed line is the super galactic plane.

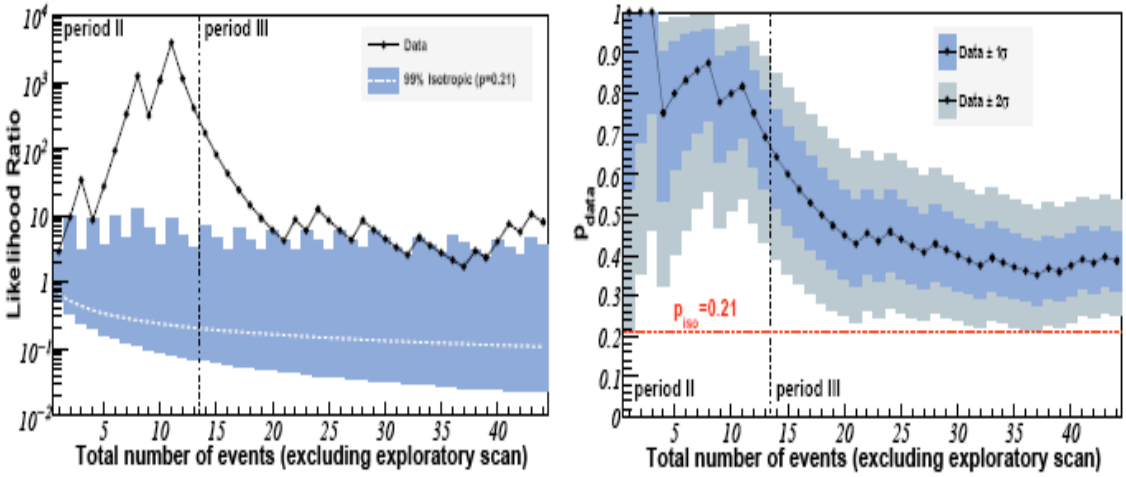

Figure 2.20: Monitoring the correlation signal. Left: The sequential analysis of cosmic rays with energy greater than 55 EeV arriving after 27 May, 2006. The likelihood ratio for the data is plotted in black circles. Events that arrive within $\psi_{max}=3.1^{\circ}$ of an AGN with maximum redshift $z_{max}=0.018$ result in an up-tick of this line. Values above the area shaded in blue have less than 1% chance probability to arise from an isotropic distribution. Right: The most likely value of the degree of correlation with objects in VCV catalogue is plotted (black circles) as a function of time. The 1σ and 2σ uncertainties in the observed value are shaded. The horizontal dashed line shows the isotropic value. The current estimate of the signal is 0.38 ±0.07 [24].

Yet, possible biases have been carefully explored and discarded. In particular, the parameters used to select the data sample (angular separation, maximum red shift and energy threshold) still apply: of the subset of 44 events which had not been used to define these parameters, 17 correlate when using them, a correlation that has less than 1% probability to occur by chance for an isotropic distributions of arrival directions.

2.3 Identification of the primaries

2.3.1 General considerations

Low energy cosmic rays are known to have abundances similar to those found in interstellar matter with a predominance of protons. At UHECR energies, however, the mass composition of primaries is uncertain [27-29]. There are even conjectures suggesting particles other than atomic nuclei to populate the higher energy range. Disregarding such exotic scenarios, the question remains of measuring the mass distribution of the primaries in a range spanning essentially from protons to iron nuclei, higher mass nuclei being much less likely.

The main difference between showers induced by protons and iron nuclei results from the very different natures of their first interaction in the upper atmosphere. The proton shower starts to develop on average after having crossed one interaction length and the depth of its starting point fluctuates with a variance also equal to one interaction length. The iron shower, in an oversimplified picture, may be seen as the superposition of 56 proton showers (protons and neutrons are equivalent at such energies), each carrying 1/56 of the nucleus energy. As a result it starts much earlier, and the location of its starting point fluctuates much less, than in the proton case. From then on proton and iron showers develop in the same way. While such a description is useful to provide a simple qualitative explanation of what is going on, the reality is far more complex and its details are not well understood. Not all nucleons of the colliding nuclei interact the same way. In a simplified picture, some nucleons – one refers to them as wounded nucleons – interact as if they were independent nucleons while the other nucleons – one refers to them as spectator nucleons – are unaffected. This, again, is an oversimplified view of reality. Glauber model [30] provides a recipe to evaluate the number of wounded nucleons.

Nevertheless, as a general rule, in order to distinguish between light and heavy incident nuclei one will aim at measuring quantities that are sensitive to the early shower development. The interest of such measurements is obvious and their importance is increased by the results of the preceding section, some of which may invoke a significant iron population to explain why some of the highest energy UHECR do not seem to point to any known counterpart.

2.3.2 Longitudinal profiles

The fluorescence detector (FD) of the Pierre Auger Observatory can be used to measure with good resolution the shower longitudinal profile and the depth at

which the shower reaches its maximum (X_{max}). At a given energy, the mean and the width of the X_{max} distribution are both correlated with the cosmic ray mass composition [31]. Proton showers penetrate deeper into the atmosphere (larger values of X_{max}) and have wider X_{max} distributions than heavier nuclei.

In practice, however, such a measurement is difficult and a strict selection of useful events is mandatory. A good geometry (average angular resolution of 0.6^{o}) [32] is obtained by requiring the simultaneous detection of shower particles in at least one Cherenkov tank of the SD and by rejecting showers pointing toward the telescope (the time over which pixel hits are recorded must exceed 5 μs). Moreover, the reconstructed X_{max} should be clearly identified and, obviously, lie within the field of view [33]. This is achieved by requiring that the observed profile spans at least 320 gcm^{-2} and that the reduced χ^2 of a fit to a reference profile (showing a maximum) does not exceed 2.5 and is smaller than that of a straight line fit by at least 4 units. Finally, the estimated uncertainties of the shower maximum and total energy must be smaller than 40 gcm^{-2} and 20%, respectively. The uncertainty on the X_{max} measurement is evaluated from stereo events and found to be 21±1.5 gcm^{-2}.

The most recent PAO results [34] are shown in Figure 2.21 together with predictions of popular hadronic models for both protons and iron nuclei. While they show a clear trend towards higher masses, their interpretation is not straight forward. Indeed, in the case of a pure proton-iron mixture, one expects the *rms* value to start rising when evolving from pure proton to pure iron contrary to what is observed in the data. The *rms* value should reach a maximum, some 12% above the iron line, for a ~ (1/3 proton)/(2/3 iron) mixture.

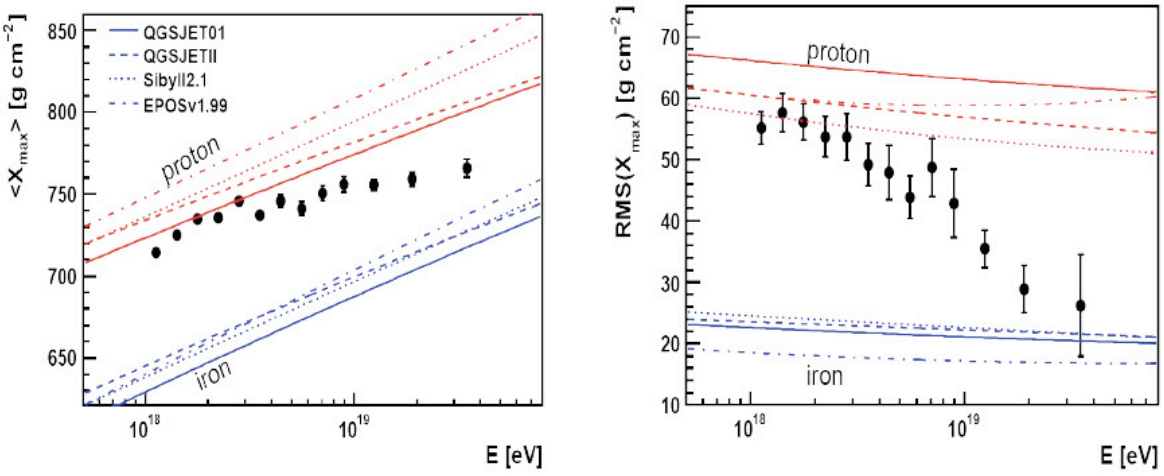

Figure 2.21: $<X_{max}>$ and $RMS(X_{max})$ energy distributions compared with air shower simulations [35] using different hadronic interaction models [19, 20].

2.3.3 Risetime

The time profile of particles reaching ground is sensitive to the shower development as the first portion of the signal is supposed to be dominated by muons which arrive earlier and over a period of time shorter than electrons and photons [36]. A risetime ($t_{1/2}$) is defined for each tank FADC trace as the time to go from

10% to 50% of the total integrated signal. To the extent that both risetime and X_{max} are expected to be sensitive to the primary mass composition, they should display a clear correlation. Evidence for it is obtained by unfolding the dependence of the risetime on zenith angle and distance to the shower axis. This is done by defining a standard function, in the same spirit as was done for the LDF, and using a particular energy (10^{19} eV) as reference – as one uses the particular distance of 1000 meters for *S(1000)* [37]. The resulting quantity, called Δ_i, increases on average with energy as expected for showers developing deeper into atmosphere (Figure 2.22 left) and is indeed clearly correlated with X_{max} [38] as shown in Figure 2.22 right.

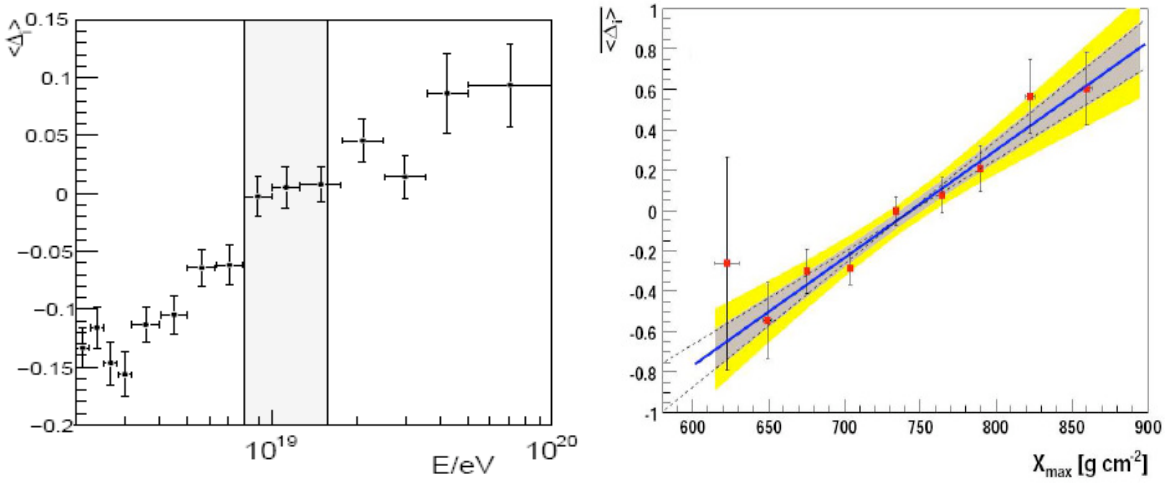

Figure 2.22: Left: SD events; dependence of the mean value of Δ_i on energy. Right: Hybrid events; dependence of the mean value of Δ_i on X_{max}. A correlation is found which is parameterised with a linear fit. The shaded areas show the estimated uncertainty (one and two σ), obtained by fluctuating each point randomly within the measured error bar and repeating the fitting procedure.

One might of course exploit this correlation to calibrate the risetime scale in terms of mass composition but this would not bring additional information – except, to some extent, for what concerns the relative energy dependences of X_{max} and Δ_i.

Another property displayed by the risetime is its dependence on tank azimuth ζ measured around the shower axis, the more so the more inclined is the shower. When an inclined shower reaches ground, the upstream tanks are hit first and the downstream tanks are hit last. The former probe the shower at an earlier stage of development than the latter do. But there is also a pure geometric effect [39] that differentiates between upstream and downstream tanks. The path length for particles to reach an upstream tank from the shower axis is much shorter than that to reach a downstream tank with the result that the former are seen under a larger solid angle than the latter and therefore detect a larger signal. Moreover, as noted earlier, the response to muons – most muons having sufficient energy to feed through the tanks – is independent, on average, from the angle of incidence. On the contrary, that of electrons and photons – generating small showers in water – depends on the angle of incidence in the same way as does the tank section normal to the incoming particle momenta. The net effect is an azimuthal asymmetry of the tank responses around the shower axis, trivially increasing with the distance r of the tank to this

axis. This asymmetry is in particular visible on the azimuthal dependence of the risetime and is observed to reach a maximum for a value θ_{max} of the zenith angle θ which is sensitive to the depth at which the shower density starts declining. In practice a fit of the form $t_{1/2}=(a+b\cos\zeta)r$ allows to measure the dependence on $\sec\theta$ of the asymmetry b/a, which is found to be maximal around $\theta=50^{o}$ independently from energy [38]. This is illustrated in Figure 2.23 where it can be seen that popular hadronic models predict instead an increase with energy of the zenith angle at which the azimuthal asymmetry is maximal. If one were to interpret this result in terms of mass composition, one would conclude that the mean primary masses increase with energy. Indeed, this result is consistent with the FD measurements of the longitudinal profile, suggesting a transition from proton dominance – light nuclei – to iron dominance – heavier nuclei – when the energy increases from 1 to 30 EeV.

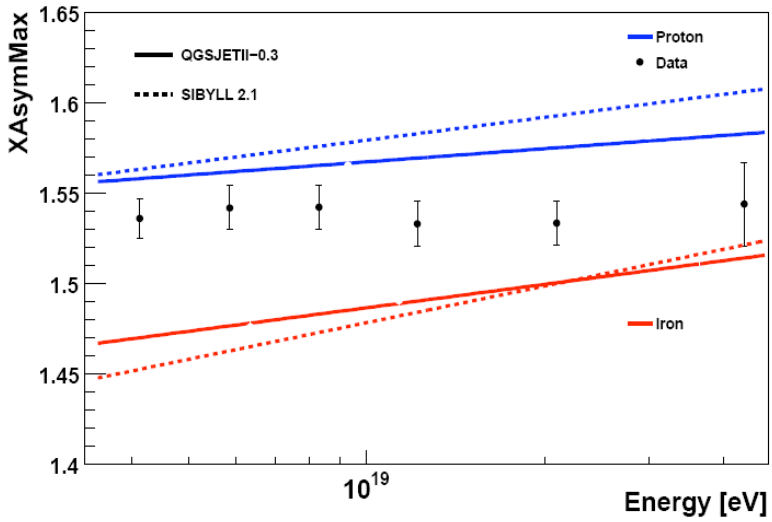

Figure 2.23: Measured dependence of the position of maximum asymmetry on primary energy. Lines correspond to fitted distributions of MC samples for proton (blue) and iron (red) primaries.

2.3.4 Muon abundance

An indicator of the shower age is the relative muon abundance, which increases with age: at a same depth, iron showers are therefore expected to be more muon-rich than proton showers are. While no direct measurement of the muon abundance has yet been made, numerous attempts at measuring quantities closely related to the muon abundance have been explored. Such is the risetime, which was presented in the preceding section.

Other approaches include attempts at identifying muons from sudden jumps [40] in the FADC traces (the "jump method") and a direct evaluation of the muon signal by subtraction of the electron-photon contribution from the FADC trace [41]. This latter method implies that the electron-photon signal (i.e. the contribution given by electrons and photons to the FADC traces) is a function of energy, zenith angle and depth (measured with respect to X_{max}) having a zenith angle dependence obtained from the hypothesis that the bulk of detected showers are isotropic and an

energy dependence known from hadron models. Under such assumptions, the muon abundance is the only unknown. When measured relative to that predicted for proton primaries, it is 1.53+0.08 (stat.)+0.21 (syst.). Pure iron composition would predict a lower factor, of the order of 1.3.

Additional evidence is obtained by the analysis of hybrid events [42] where the longitudinal profile is used to choose between a proton and an iron hypothesis, whatever is best, and to then predict the amplitude of the signal on ground (Figure 2.24).

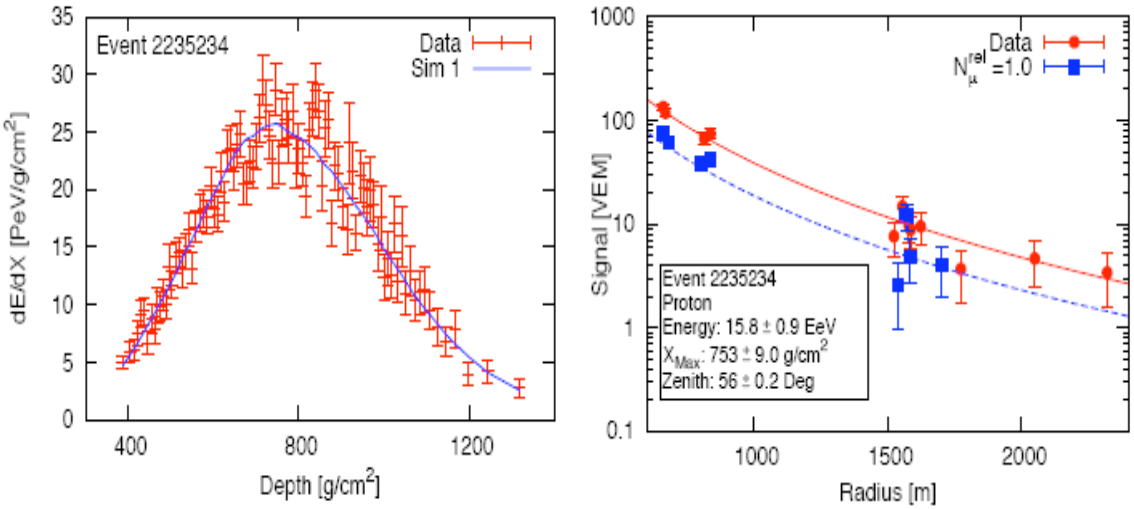

Figure 2.24: Measured longitudinal (left panel) and lateral (right panel) profiles for one of the hybrid events. The best-matching simulation is shown as squares and dashed line in the lateral distribution while the measured SD signal (circles, full lines) is more than twice as large.

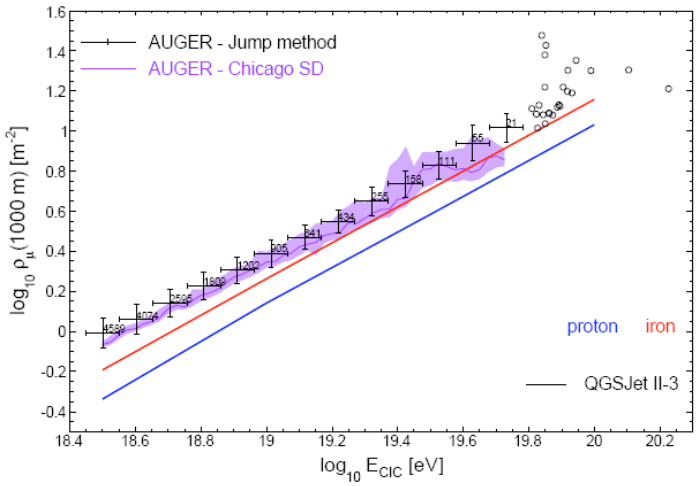

Figure 2.25: Results of earlier studies on primary composition.

A similar conclusion is also reached from analyses of the FADC traces such as done with the jump method: the muon abundance inferred from such analyses is significantly larger than that predicted for iron by popular hadronic models. Figures 2.25 and 2.26 summarize the results. A possible interpretation is to dispose of the

problem by blaming it on a 30% underestimate of the FD energy scale, as illustrated in Figure 2.26. Even so, measurements exceed the expected muon abundance for iron. Moreover, a recent energy independent analysis [43] would rather suggest that the hadronic models used in the simulation predict too steep a muon lateral distribution function. This is indeed another way to increase the amplitude of the muon component in the *D* range explored by the SD. Moreover it would explain why the azimuthal asymmetry of the risetime gives results in agreement with the FD X_{max} measurement, as both probes the longitudinal profile independently from the lateral distribution function.

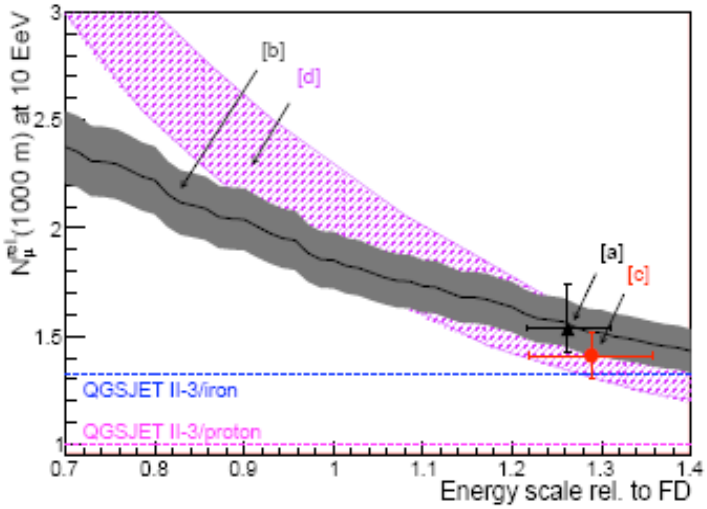

Figure 2.26: Number of muons at 1000 m relative to QGSJET-II/proton vs. the energy scale from different SD analyses (see text). The events have been selected for $\log_{10}$(E/eV) = 19.0 ± 0.02 and $\theta \leq 50^o$. According to the tested model, iron primaries give a number of muons 1.32 times bigger than that from protons (horizontal lines in the figure).

2.3.5 Summary

In summary, the mass composition of UHECR primaries remains an open question. Major progress has been achieved in the analysis of FD data where a rigorous treatment of possible biases and systematic uncertainties is now available. The results are consistent with the predictions of hadronic models and, in such a picture, provide evidence for a transition from proton-like to iron-like primaries over the energy range covered by the PAO, say 1 EeV to 30 EeV where the GZK threshold becomes effective. This conclusion is also reached, with lesser accuracy, by the analysis of the azimuthal risetime asymmetry in the SD, an analysis sensitive to the depth at which the longitudinal shower profile starts declining. Yet, SD analyses that are sensitive to the amplitude of the muon signal can only be made consistent (barely) with the predictions of hadronic models at the price of a 30% increase of the energy scale. A possible cause might be the inadequacy of hadronic models to reproduce the lateral distribution function of muons. Another possible cause might be the inadequacy of the detector simulation to describe the response to muons.

Chapter 3

JUMPS AS AN IRON-PROTON DISCRIMINATOR

3.1 Introduction

3.1.1 Aim

The aim, in the present section, is to use the PAO surface detector to obtain independent information on the nature of UHECR primaries. While the correlation data (between UHECRs and AGNs) suggest that they are dominantly protons at the highest energies [44], the elongation rate data [45] suggest that they are somewhere between protons and iron at energies just below. The hope to contribute independent information from the SD is based on the idea that the number of muons reaching ground should be a valuable discriminator between light and heavy primaries [46].

Many approaches are being used to attempt an evaluation of the number of muons per FADC trace, that is per Cherenkov tank, of the Auger SD and consequently to obtain independent information on the nature of the primaries. Of particular interest to the present section is the so-called jump method [47], which has been developed at LAL-Orsay.

An important difference between the different methods is the amount of reliance that they imply on the shower models used to predict the muon abundance.

An extreme view is to have full confidence in the simulated data; the problem is then to find the best discriminator between simulated proton and iron data, it is a purely mathematical problem. Such an extreme view is adopted, for example, by the Catania team [48], who are using neural networks to address the issue.

Another approach is to rely as little as possible on the simulation of the detector response, which is obviously very complex. Attempts at measuring the muon fraction by disentangling muon signals directly from the FADC traces fall in this category [49]. However, this approach cannot be completely independent from simulation: a shower development model must always be used to differentiate between different primaries.

Both views are useful and cannot be compared, it makes no sense to say that one is better than the other, one needs to master both to reach reliable conclusions, they are complementary. A convincing conclusion on the nature of the primaries requires giving strong arguments for the validity of the simulation. The multiplicity of approaches being currently explored, to the extent that they are converging, is a step in this direction.

Most methods [50] rely more or less heavily on the validity of the simulation depending on the details of how they are applied. The case of the jump method [47] is of particular interest in this context. The method is briefly summarized below.

3.1.2 Jump method

In the FADC trace (averaged over three PMTs) of each tank hit by a shower, a quantity J, called the total jump, is defined as the sum of all differences (jumps) in excess of 0.5 VEM between the content of a 25 ns time bin and its predecessor. There are N_J occurrences of such differences per trace. The total charge, Q, is the sum of the contents of all time bins. While J and Q are measured in VEM units, N_J has no dimension.

In principle, J receives contributions from both muons and electrons/photons. Details on these individual contributions are given in Section 3.2. Evidence that it receives significant contributions from muons is obtained from the presence of a clear shoulder in the distribution of the individual jumps, both in real and simulated data. A comprehensive analysis of the underlying physics is given in Reference 47 with the result that J is related to the number of muons, N_μ , as shown below:

$$J = A J_{low} + B\, N_\mu \qquad (3.1)$$

with $A = C_{em}(v_1)/C_{em}(v_2)$

and $B = \varepsilon_\mu(v_1)\{1-[C_{em}(v_1)\varepsilon_\mu(v_2)]/[\,C_{em}(v_2)\varepsilon_\mu(v_1)]\}$

Here, both A and B are constants. The quantity J_{low} is defined as J, the only difference being the use of a lower threshold ($v_2 = 0.1$ *VEM* instead of $v_1 = 0.5$ *VEM*). The quantities C_{em} and ε_μ can be understood as average electromagnetic contamination and muon selection efficiency respectively. They are obtained from the simulated data. Relation (3.1) may be written, equivalently, as

$$N_\mu = A_1 J + A_2 J_{low} \qquad (3.1')$$

with $A_1^{-1} = B = \varepsilon_\mu(v_1)\{1-[C_{em}(v_1)\varepsilon_\mu(v_2)]/[\,C_{em}(v_2)\varepsilon_\mu(v_1)]\}$

and $A_2 = -AA_1 = -A_1\, C_{em}(v_1)/C_{em}(v_2)$.

Here, again, A_1 and A_2 are constants. In Reference 47, Relation (3.1') is replaced by a proportionality relation

$$N_\mu = \alpha J \qquad (3.1'')$$

where α is parameterized as a function of energy E, zenith angle θ and distance to the shower core D.

Relation (3.1'') allows for an evaluation of the number of muons having hit a given Cherenkov tank from a measurement of J. For a given value of J, the width of the N_μ distribution defines the accuracy with which this can be done. If one trusts the simulation, one simply needs to look for the best possible parameterization of α as a function of E, θ and D and compare the real data with simulated protons and iron data separately. One may, however, wish to face the possibility that the numbers of muons predicted by the simulation be not quite right, in which case Relation (3.1) is more appropriate to the extent that it does not merge the electron/photon and muon contributions in a single parameter but keeps them separate. In particular, and such is our approach in the present work, it allows for a parameterization based not only on the simulated data but also, simultaneously, on

data made up from the simulated data and containing either no muon at all or twice as many muons than normal.

3.1.3 General comments

Having addressed in Section 3.2 the question of muon counting, one is still faced with a more difficult question: how good a discrimination does muon counting provide between iron and proton primaries? The answer to this question relies fully on the validity of the shower development model used in the simulation, in particular on the adequacy of its treatment of nucleus-nucleus interactions.

Iron and proton primaries of a same energy are found in Section 3.3 to induce showers having significantly different particle densities on ground. In the energy domain of relevance here, iron showers give a larger ground density than proton showers. If the primary energy were known, one would therefore have several discriminators available to identify the primary. In particular, not only the total jump J but also the total charge Q and the number N_J of jumps would be perfectly reliable discriminators.

However, the energy of the primary is unknown, all what is known is precisely the particle density on ground which is used (in the form of a lateral distribution function) to obtain an estimate of the primary energy under the assumption that it is a proton. Two showers having different particle densities on ground may therefore be, for example, two proton showers of different energies, or a proton and an iron showers of a same energy. To first order, there is no way to tell them apart from the SD information alone. Section 3.4 addresses this problem and discusses the circularity of the arguments being used to identify primaries by muon counting.

This being clarified, Section 3.5 presents an energy-independent analysis of the PAO data which attempts at being free of the above difficulties. Energy independent discriminators, such as the ratio between the total jump and the total charge, J/Q, are made use of at distances from the shower core depending on ground density. As a particular application, Section 3.6 presents a study of UHECR showers correlated with Cen A.

Section 3.7 summarizes the study in the context of recent results of the Pierre Auger Collaboration which give evidence for an apparent inconsistency between the interpretation of FD and SD data, precluding a reliable evaluation of the mass composition from the SD data alone. In a nutshell, using the FD energy scale, the amplitude of the muon component estimated from SD data is about twice that predicted for protons, while that predicted for iron is only 4/3 of that predicted for protons. A possible interpretation, explored in References 51 and 52, is that the FD underestimates energies by some 30%. The energy-independent analysis presented in Section 3.5 shows that such an interpretation may only account for a minor part of the inconsistency.

As a final comment to close this introduction, it must be noted that no method of primary identification can allow for a shower-by-shower assignment: shower-to-shower fluctuations are much too important. Large statistical samples need to be used.

3.2 Muon counting

3.2.1 Separate contributions to J

The simulated data [53] used in the present section are divided into 18 families (three energies, two zenith angles and three distance intervals to the shower core). Energies and zenith angles are values used as input to the simulation; distances to the shower core are evaluated from the simulated data. The three energies (E) are $10^{18.5}$ eV, 10^{19} eV and $10^{19.5}$ eV. The two zenith angles (θ) are 0^{o} and 45^{o}. The three distance intervals (D) are defined differently for each energy in order to have three event samples of similar sizes in each case:
$D<D_1$, $D_1<D<D_2$ and $D>D_2$ with $[D_1, D_2]$ = [880 m , 1260 m], [1140 m , 1600 m] and [1440 m , 1950 m] for $log_{10}E$ = 18.5, 19.0 and 19.5 respectively.

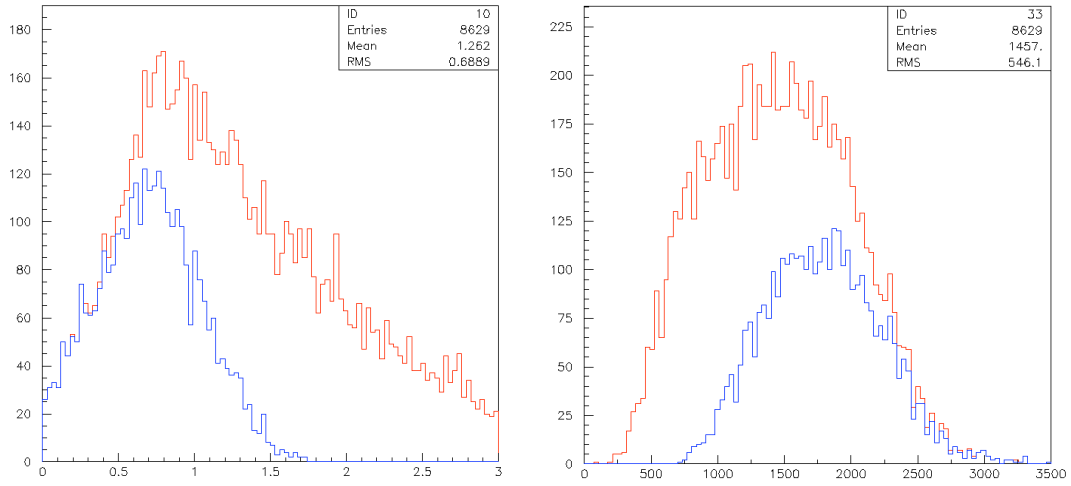

Figure 3.1: Left: Distributions of the decimal logarithm of the total charge *Q [VEM]* for all photon traces (red) and those having no jump in excess of 0.5 VEM (blue). Right: Distribution of the tank distance to the shower core [m] for all showers (red) and for showers having a photon trace with no jump in excess of 0.5 VEM (blue).

More generally, the central D interval, $[D_1, D_2]$, is defined as:

$$D_1(m)=560log_{10}E(eV)-9490, \qquad D_2(m)=700log_{10}E(eV)-11700 \qquad (2)$$

For each FADC trace we know from the simulation the number of muons N_μ and the separate contributions of electrons/photons and muons.

The "muonless" data are simply obtained by retaining only the electron/photon traces of the above "standard" data. The "double-muon" data are obtained by adding to each standard trace (muons + electrons/photons) the muon contribution of the preceding event in the same family (same energy, same zenith angle and same D interval).

While the FADC trace is the sum of the photon and muon contributions, the value of J does not obey the same additive law: the value of J obtained on the sum of the two traces is not the sum of the values of J obtained on each of the two traces separately! Yet, it is instructive to study the results of a jump analysis applied to the photon and muon traces separately. This was done in some detail in Reference 54.

Some selected results (obtained on the whole sample of simulated data used above) are presented below.

The fraction of electron/photon traces having no jump in excess of 0.5 VEM (i.e. J and N_J being both zero) is found to be 43%. These correspond to low Q and large D values as illustrated in Figure 3.1. The mean and *rms* values of Q for such traces are 7.4 and 5.7 VEM compared to 67.4 and 142.5 VEM for the whole sample. One notes that up to $Q \sim 3$ VEM, the two distributions are nearly identical. The number of muons associated with such traces has a mean value of 4.9 compared with 18.9 for all traces.

The distribution of J for electron/photon traces having $J>0$ is shown in Figure 3.2. J is found, on average, to be proportional to Q. Figure 3.3 shows examples of electron/photon traces having significant J values.

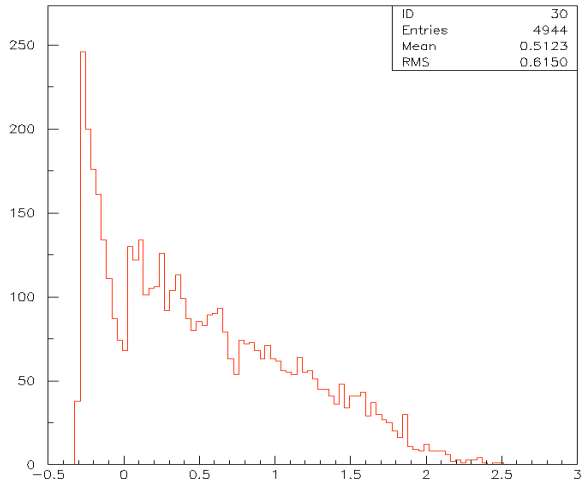

Figure 3.2: Distribution of the decimal logarithm of J for all electron/photon traces having at least one jump in excess of 0.5 VEM.

Looking now at muon traces, N_μ is found to depend linearly on J. On average, it is equal to $J' = 3.45J - 2.55$. The distribution of the quantity $N_\mu - J'$ is displayed in Figure 3.4 for different intervals of N_μ.

These results show that on pure muon traces J accounts on average for typically 1/3 of the total number of generated muons. The spread of the distributions shown in Figure 3.4 is equal to 3 muons for $N_\mu = 1$ and keeps increasing as 20% of the generated number of muons.

Inspection of individual traces shows that in several instances no method whatsoever, whether jump or else, has a chance to make a sensible and useful statement concerning the number of muons contributing to the trace, there is no way to tell a strong and narrow electron/photon signal from overlapping muons. Adding the photon trace only makes the situation worse. It is important, when trying to measure the muon to electron ratio, to limit one's ambitions to regions of the parameter space where one has a chance to say something sensible. Examples are shown in Figure 3.5.

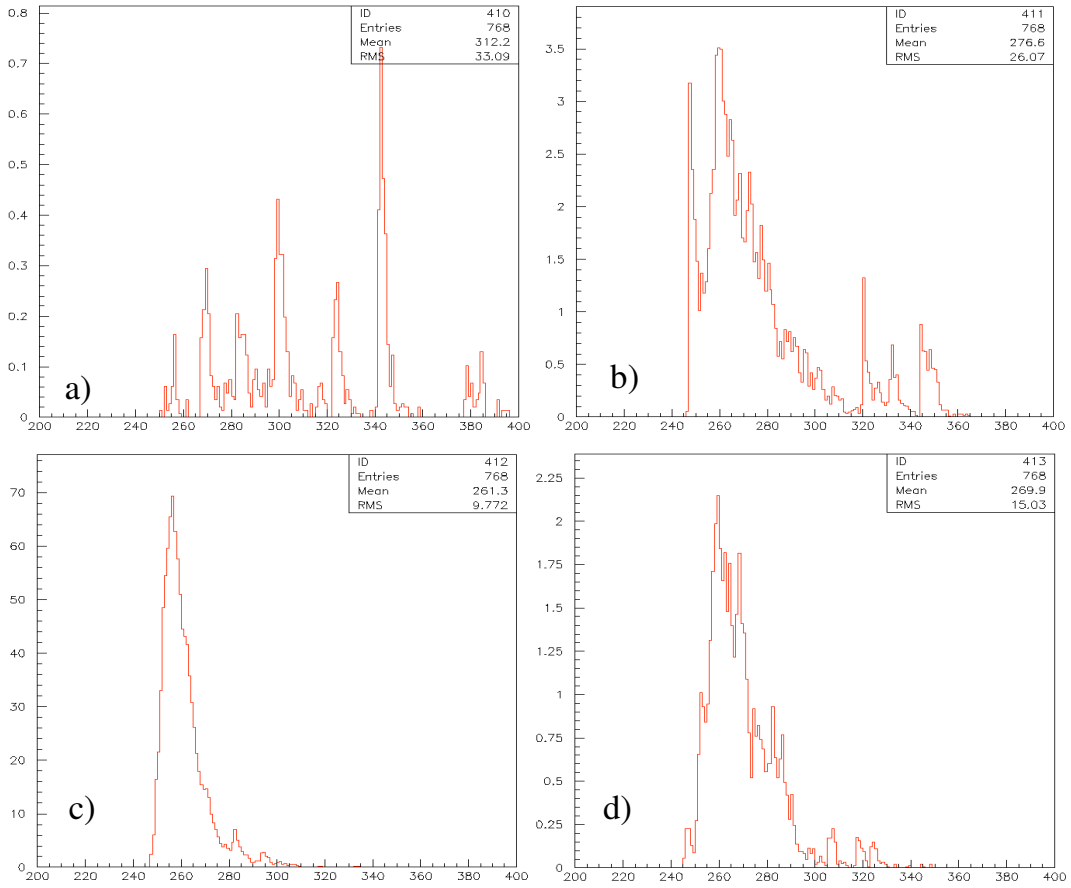

Figure 3.3: Four examples of electron/photon traces. Events a to c are for *Q~10, 100* and *1000 VEM* respectively with *J = 0.0, 7.3* and *74.7 VEM* respectively. Event d) has *J = 0* although *Q* is relatively high: *46.2 VEM*.

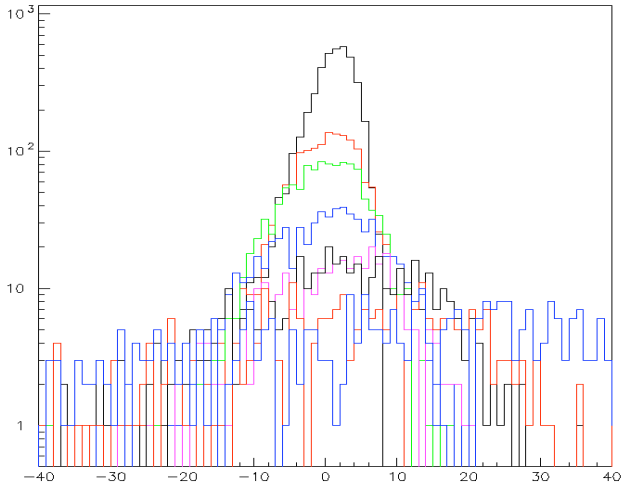

Figure 3.4: Distribution of $N_\mu - J'$ for different N_μ intervals in muon traces. The distributions get wider when N_μ increases. The intervals are 0-5, 5-10, 10-20, 20-30, 30-40, 40-60, 60-80 and >80.

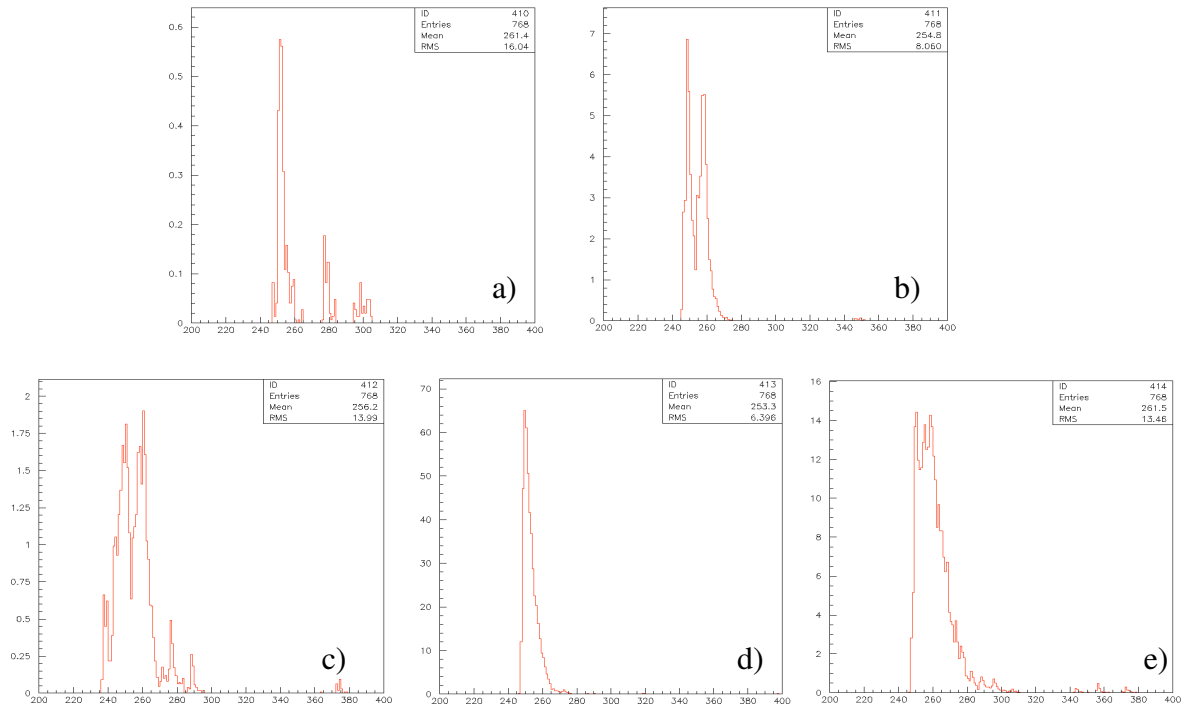

Figure 3.5: Five examples of muon traces. The respective values of Q, N_μ, J and J' are: a) 3, 4, 0, -3; b) 60, 19, 11, 34; c) 35, 19, 1, 2; d) 459, 166, 65, 221; e) 271, 119, 21, 168 where Q, J and J' are in VEM units.

3.2.2 Parameterization of J as a function of Q and N_μ

Relation (3.1) is now used in order to evaluate the values of coefficients A and B. However, the quantity Q is used instead of J_{low} but the two quantities are closely related.

A and B are fit to the relation $J = AQ+BN_\mu$ in the central D interval for all families together with the result

$A = (43.9 \pm 0.5)10^{-3}$

$B = (200 \pm 2)10^{-3}$

where the errors are statistical only. The uncertainty used in the χ^2 minimization is $\Delta J = J/\sqrt{N_J}$.

Figure 3.6 illustrates the quality of the fit. It shows the distribution of $(J_{Cal}-J)/\Delta J$ where $J_{Cal} = AQ+BN_\mu$. Muonless, standard and double-muon data are shown separately. Figure 3.7 shows the error ellipse in the (A, B) plane. Relative uncertainties on both A and B are at the percent level; there is a correlation between the two parameters, but not very strong.

One should note, however, that the three samples are not completely statistically independent. The fit is seen to work equally well for the muonless, standard and double-muon samples. This is an obvious improvement with respect to using a proportionality relation (3.1"), which, in particular, cannot cope with muonless events. It relies less on the simulation, it is independent from E, θ and D and requires only two parameters for the whole data set, but it still relies on the

simulation to predict the time distributions of the separate muon and electron/photon contributions to the FADC trace.

It is interesting to note that in the central *D* bin $\langle J\rangle/\langle Q\rangle$ = 0.050 for pure electron/photon traces and $\langle J\rangle/\langle N_\mu\rangle = 0.37$ for pure muon traces; these values are commensurate with the values of *A* and *B*, 0.044 and 0.20 respectively.

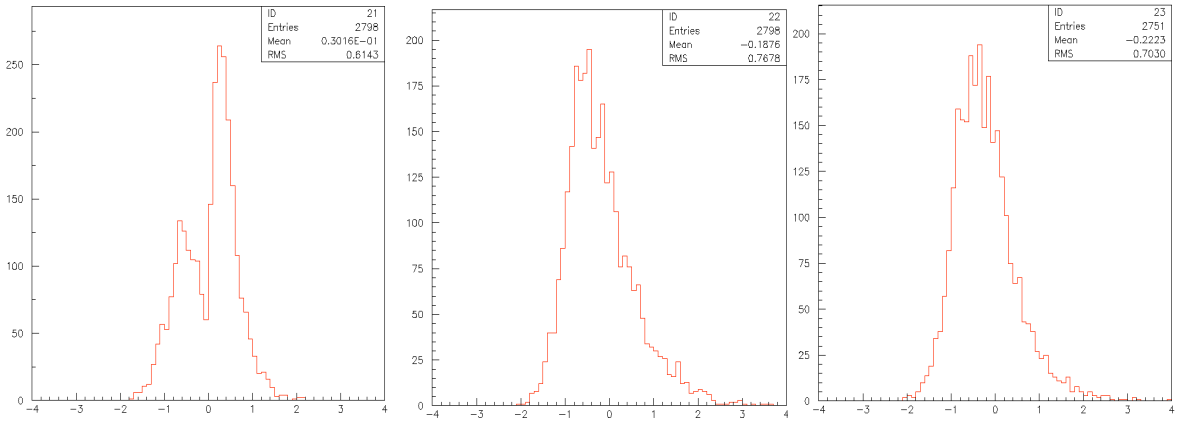

Figure 3.6: Distribution of $(J_{Cal}-J)/\Delta J$ for all families together in the central *D* interval (left: muonless; central: standard; right: double muons).

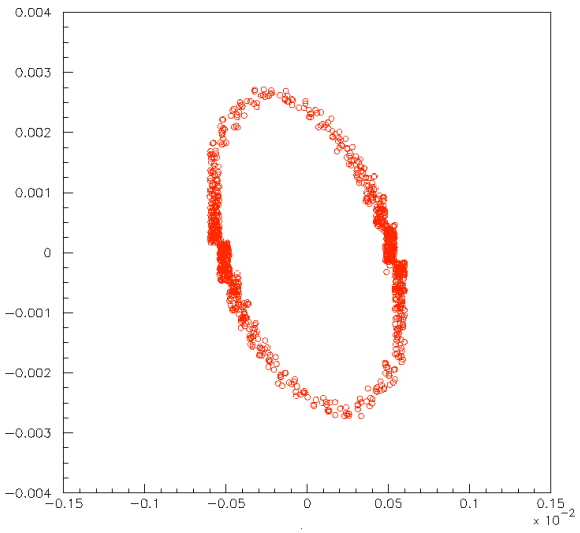

Figure 3.7: Error ellipse in the *(A, B)* plane. *A* is in abscissa and *B* in ordinate.

3.3 Iron-proton discrimination

Essential information is the knowledge of the separation between the simulated proton and iron data when using different discriminators. For a given discriminator, *J*, N_J, N_μ or *Q*, we calculate the mean values, M_p and M_{Fe} , and *rms* values, σ_p and σ_{Fe} of its distribution for each of the 18 families and define the proton-iron separation as

$$S=(M_{Fe}-M_p)/\sqrt{(\sigma_p^2+\sigma_{Fe}^2)} \qquad (3)$$

The usefulness of this concept is apparent from the following example: assume that one has a distribution of N showers and that one wishes to identify their primaries. To an excellent approximation, $\sigma_p=\sigma_{Fe}=\sigma$. The uncertainty ΔM on M is $\sigma/\sqrt{N}$. If one wishes to make a statement having a significance corresponding to k standard deviations, one needs ΔM to be smaller than $(M_{Fe}-M_p)/k=\sqrt{2}S\sigma/k$, namely one needs $N>½(k/S)^2$.

The results [57] can be summarized as follows. The global S values, all families together, are very small: 1.9, 0.1, 4.2 and 1.2 % for each of J, N_J, N_μ and Q respectively. The uncertainties are of the order of 1.5%. In order to obtain sensible separations, one needs to restrict the analysis to the central D interval, which we shall be doing from now on. In this central interval, the global values of S become 26, 27, 37 and 28% with uncertainties of the order of 3%. According to what was just said, a 3 standard deviation statement requires a statistics of 50 tanks with $S\sim30\%$. A shower-by-shower discrimination is therefore impossible.

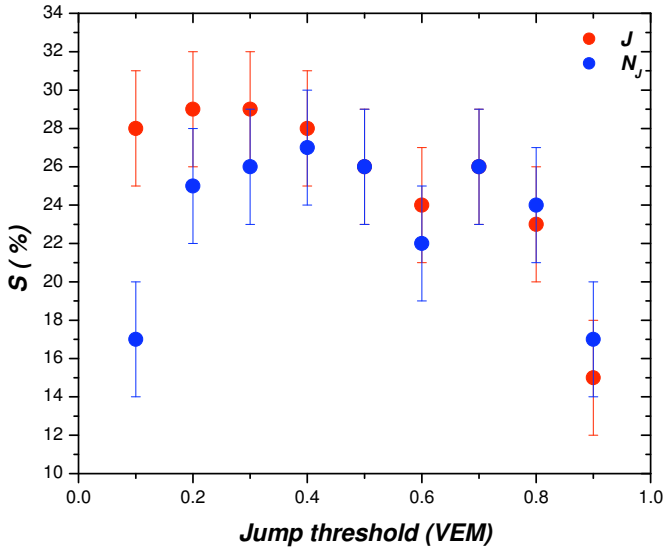

Figure 3.8: Dependence on jump threshold of the separation between protons and iron. Red dots are for J and blue dots for N_J.

The separations in J and N_J depend on the threshold used in defining jumps, namely 0.5 VEM. Changing this threshold changes the separations in J and N_J as shown in Figure 3.8. One might have expected J to reach a maximum for a threshold of 0.5 VEM, but such is not really the case. Indeed, J_{low} appears to be as good discriminators as J. So does Q, which is strongly correlated with J_{low} as illustrated in Figure 3.9. It would seem that, for most purposes, one may use indifferently one or the other.

Both J and N_J are similarly efficient discriminators and the question naturally arises of a possible correlation between them. Namely is it possible to achieve a better separation by using both J and N_J than by using just one of them? The answer is essentially negative as the two quantities are strongly correlated, as illustrated in Figure 3.10 which displays the correlation in the plane $J-\langle J\rangle$ *vs* $N_J-\langle N_J\rangle$ (the mean values are calculated for each family independently). The strong correlation

implies that there is not much to gain by using both J and N_J information. Indeed, Figure 3.11 shows the distributions of $J+N_J$ (J, expressed in VEM, and N_J being roughly equal on average) for protons and iron separately. The separation is now 29% compared with 26% and 27% when these discriminators are used separately.

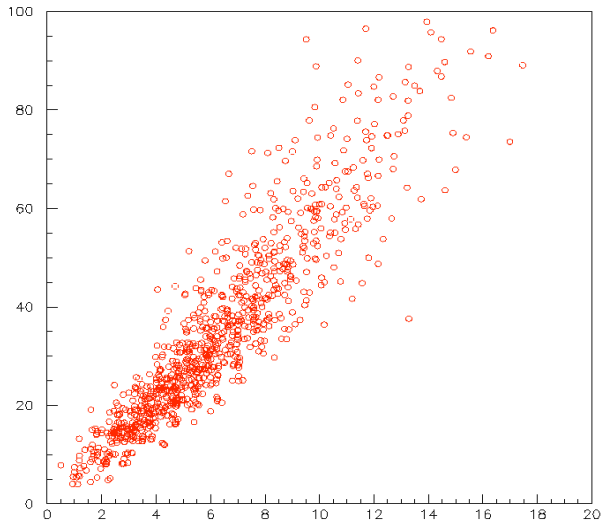

Figure 3.9: Correlation between J_{low} (in abscissa) and Q (in ordinate) in the central D interval for all families together.

We may note that N_μ is the best separator, which is comforting. Of course, it cannot be used in practice, as it is obviously unknown when dealing with real data. It has to be estimated. The jump method does it using Relations (3.1 to 3.1").

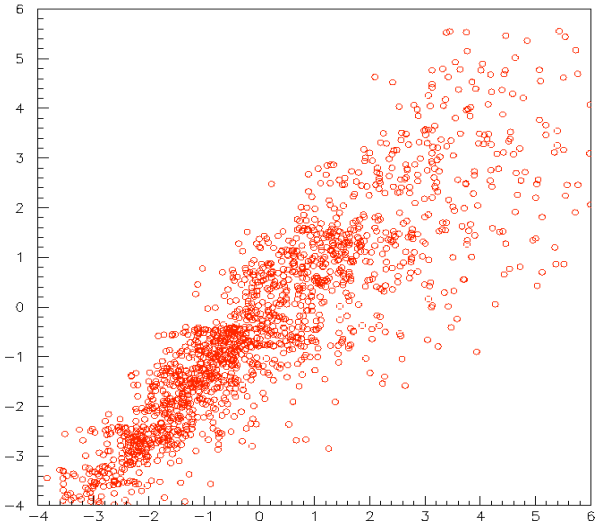

Figure 3.10: Two dimensional plot of $J-\langle J\rangle$ (ordinate) *vs* $N_J-\langle N_J\rangle$ (abscissa) in the central D interval (all families together).

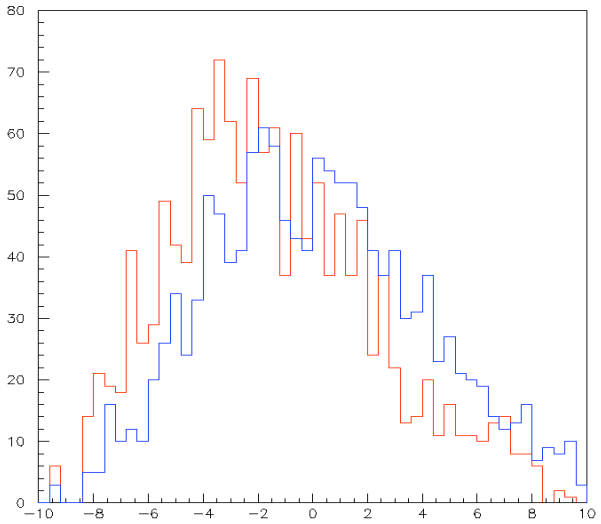

Figure 3.11: Distribution of the global discriminator $J+N_J$ in the central D interval for protons (red) and iron (blue) respectively.

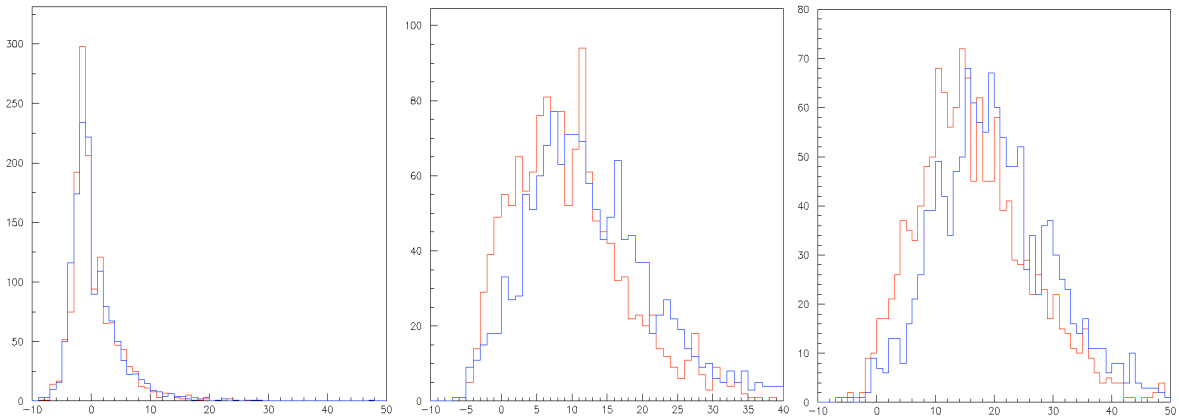

Figure 3.12: Distribution of N_{Cal} calculated in the central D bin (left: muonless; central: standard; right: double muons) for protons (red) and iron (blue) respectively.

Figure 3.12 displays the distribution of $N_{Cal} = B^{-1} J + (A/B) Q$ calculated in the central D interval for protons and iron separately using the fit values for A and B. The data are shown separately for each of the three samples (muonless, standard and double-muons). The separation obtained is 2%, 23% and 24% respectively.

Given the crudeness of the exercise the result seems encouraging as the best separation achieved so far was 27%. The low separation obtained for muonless data shows that the electron/photon components of protons and iron data have similar J values. In the double muon data both the mean value and the *rms* value of N_μ increase when going from protons to iron in such a way that the separation remains nearly constant.

In conclusion, a parameterization of the number of muons as a function of both the J value and the total charge Q of the trace seems to be more adequate than a simple proportionality to the former. Its form is meant to explicitly separate, as much as possible, the individual contributions to J of the electron/photon and muon

components. Moreover, it has been shown that a very simple parameterization using only two parameters independent of zenith angle, energy and distance to the core gives good results as long as the analysis is restricted to a central D interval, defined as (energy E in eV, and distance D in metres)

$[D_1, D_2] = [560\log_{10}E - 9490,\ 700\log_{10}E - 11700]$.

Such a parameterization gives good results not only on the simulated normal data but also on muonless and double muon data, implying a lesser reliance on the validity of the simulation. Separations of the order of 25% are obtained.

The above arguments have been made in general terms but no attempt has been made to fine tune the results. Refinements such as making a better optimization of the limits of the central D interval, of the discriminator (possibly using J, N_J and Q together) and of the parameterization could be considered but they would not be expected to bring much improvement.

3.4 Energy dependence and correlations

3.4.1 A major difficulty

To the three sets of simulated data used in the preceding section, muonless, standard and double-muons, we add a set of "half-muon" traces obtained from the standard family by halving the number of muons as described in detail in [57]. Moreover we add new zenith angles, in total seven angles between 0^o and 60^o.

The distribution of the total charge Q of each FADC trace is shown in Figure 3.13 for each of the four sets separately. As the jump method is not expected to work close to the shower core where Q is very large, we shall sometime restrict the analysis to tanks having $Q < 40$ VEM. In other instances we shall restrict it to tanks at a distance D from the shower axis contained in an energy dependent interval $[D_1, D_2]$ with $D_1\,(m) = 393 + 650\log_{10}E(EeV)$, $D_2\,(m) = 753 + 770\log_{10}E(EeV)$.

As discussed earlier, this latter selection accounts both for the need to reject very large Q tanks, close to the shower core, and tanks biased by the trigger as explained in Figure 2 of Reference 47.

For each trace, having a known number N_μ of muons, one evaluates, in addition to the total charge Q, the number of jumps N_J and the total jump J. Figure 3.14 shows the distributions of the latter quantities for each of the four data sets.

It was argued in the preceding section that a form *(F')*, $J = AQ + BN_\mu$, should be preferred to a simple form *(F)*, $J = BN_\mu$, to evaluate N_μ. The argument was that both the electromagnetic and muonic components of Q contribute to J. To illustrate this, the sum of all four simulated data sets having $Q < 40$ VEM are separated in bins of N_μ and in each bin the best fit values of B (using form F) and of the pair A,B (using form F') are calculated. Also calculated is the value of B using form F' when A is fixed to the value $A_0 = 43.3\ 10^{-3}$ which it takes for pure electromagnetic traces (i.e. in the muonless set with $N_\mu = 0$). The χ^2 uses an uncertainty $\Delta J = J/\sqrt{N_J}$ on J.

The point here is that for inverting reliably F' into a form $N_\mu = \alpha J + \beta Q$, one would like A and B not to depend on N_μ. They should be constants. To check on this, we may evaluate A and B for each value of N_μ separately. When fixing N_μ one

selects a sample of *(Q,J)* pairs and fits a linear relation between them: $J=AQ+C$. The constant term, C, divided by N_μ is B. Figure 3.15 summarizes the results.

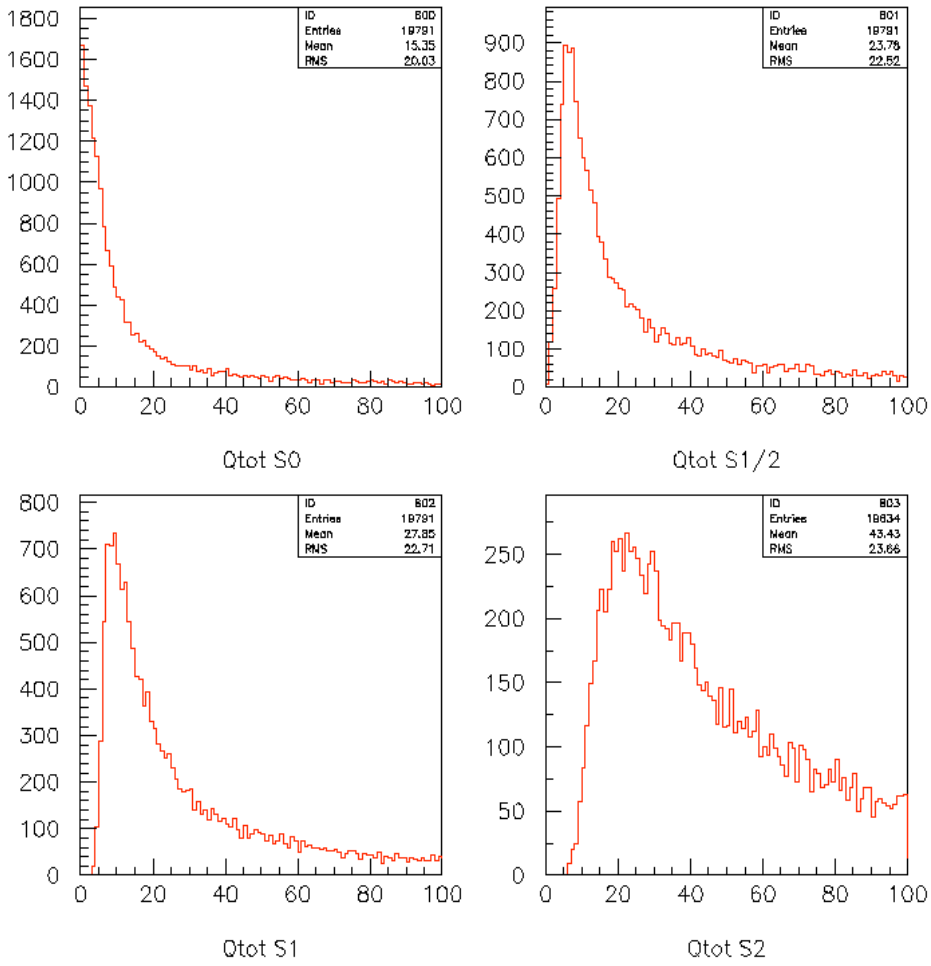

Figure 3.13: Total charge distributions (VEM) for each of the four sets of simulated data.

When using form *F'*, apart from low values of N_μ, there seems to be only a weak correlation between N_μ and J (low values of B) which seems to depend mostly on Q (large values of A). For large enough values of N_μ, C practically cancels, Q and J are approximately proportional. We note indeed that if Q and N_μ were strictly proportional, i.e. $Q=kN_\mu$, A and B would be fully correlated as $Ak+B= cte$. This is not far from being the case as illustrated in Figure 3.16. A measure of the correlation, defined as the difference divided by the sum of the principal axes of the correlation ellipse, is shown in Figure 3.17 as a function of N_μ. This high correlation explains why some points seem to behave abnormally in Figure 3.15: the error bars shown ignore the correlation and when A is high, B is low and conversely. The modest correlation found in Figure 3.7 was the result of fitting A and B on the whole range rather than on individual values of N_μ as is now done.

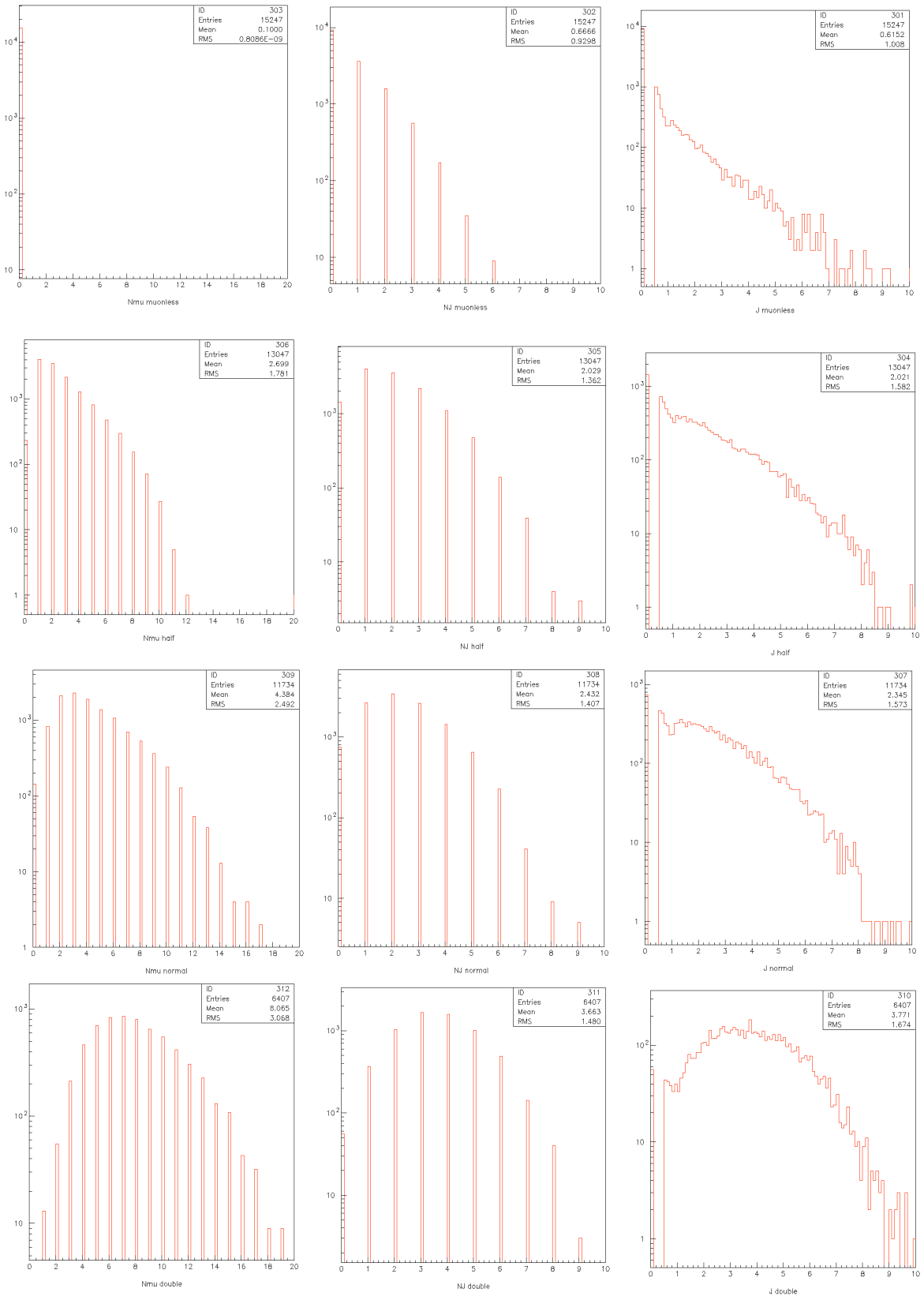

Figure 3.14: Distributions of N_μ , N_J and J (from left to right) in the muonless, half-muon, standard and double-muon sets (from top to bottom) for traces having $Q < 40$ VEM.

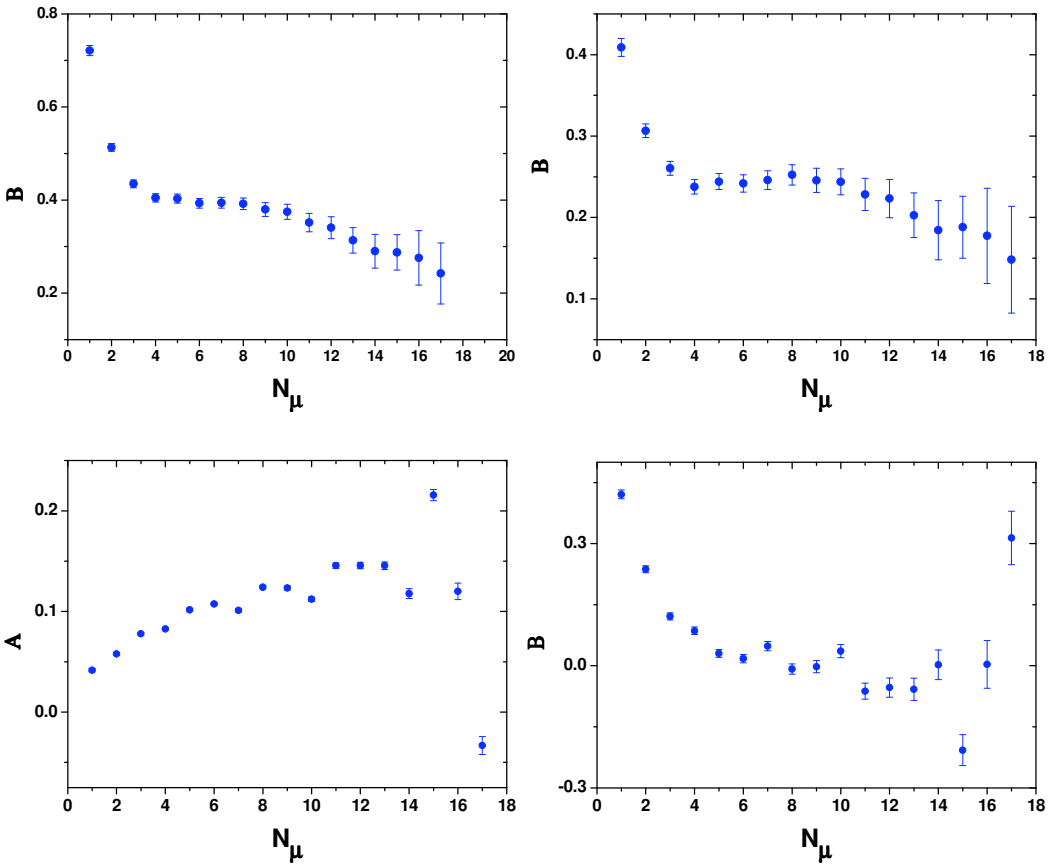

Figure 3.15: The best fit values of *A* and *B* are shown as a function of N_μ. Top left: *B* as obtained from *F*; Top right: *B* as obtained from *F'* with *A* fixed to the value A_0 which it takes in the muonless set. Bottom: *A* (left) and *B* (right) as obtained from *F'*.

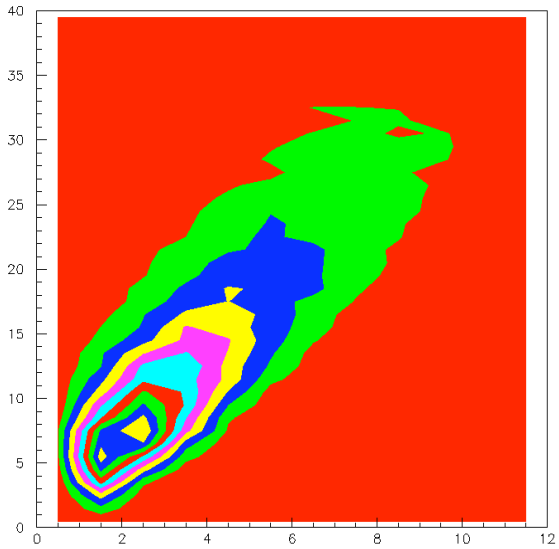

Figure 3.16: Two dimensional distribution of simulated events having $Q < 40$ VEM for all sets together. Abscissa is *Q* and ordinate is N_μ.

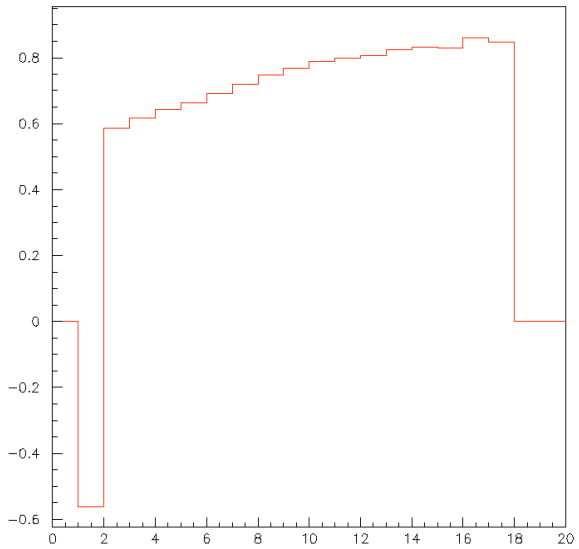

Figure 3.17: Dependence on N_μ of the correlation coefficient of the best fit values of *A* and *B* using *F'* (0 corresponds to no correlation and 1 to full correlation).

Figure 3.18 shows the dependence on N_μ of the mean values of J, Q and N_J (the values of J and N_J have been multiplied by 10 for easing the comparison). It displays a remarkable similarity between the three quantities. Another way to illustrate the problem is to display the dependence on N_μ of the *rms* values of the distributions of $\Delta J = J - \beta N_\mu$ (form F) and of $\Delta J = J - \alpha Q - \beta N_\mu$ (form F'), which is done in Figure 3.19: replacing F by F' brings only a minor improvement. In both Figures 3.18 and 3.19 Q was required not to exceed *40 VEM*.

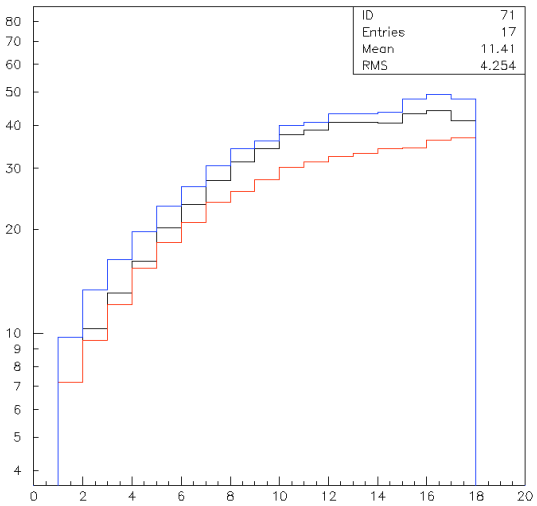

Figure 3.18: Distributions of the mean values of *J/10* (black), Q (red) and $N_J/10$ (blue) as a function of N_μ for all sets together.

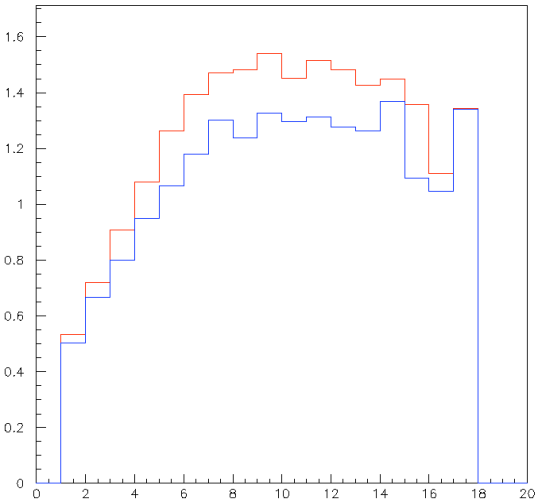

Figure 3.19: *Rms* of ΔJ for F (red) and F' (blue) as a function of N_μ for all sets together.

In summary, when applying the recipe elaborated in the preceding section, advocating the use of a form *(F')* in preference to a form *(F)*, one faces an unexpected problem: J, Q and N_J all increase in similar ways when N_μ increases. The fact that the four data sets are produced from a same standard set introduces a bias, making the effect slightly more dramatic. This makes the use of form *(F')* unpractical. Moreover, it is now clear that it is nearly impossible to tell apart the muon from the electron/photon contributions to the FADC trace without relying heavily on the simulation. This is a serious problem because one does not know the shower energy other than from the lateral distribution function, which is again nearly scaling with Q. How can this result be reconciled with the very different shapes of the jump $(q_{i+1} - q_i)$ distributions shown in Reference 46 for electromagnetic and muonic traces respectively? It was on that difference that the method was based. Figures 3.20 and 3.21 display these distributions for different Q intervals rather than mixing different Q values. In Figure 3.20, one considers pure electromagnetic traces and pure muonic traces (from each of the half-muon, standard and double-muon sets). The distributions are normalised to the number of traces considered (in the chosen Q interval for that set). One finds indeed that while the muonless distributions differ from the others, the half-muon, standard and double-muon distributions are very similar. In particular, for a threshold of *0.4*

VEM, very close to the threshold of *0.5 VEM* used in the definition of J, the number of jumps per trace in a given Q interval are independent of the nature of the trace.

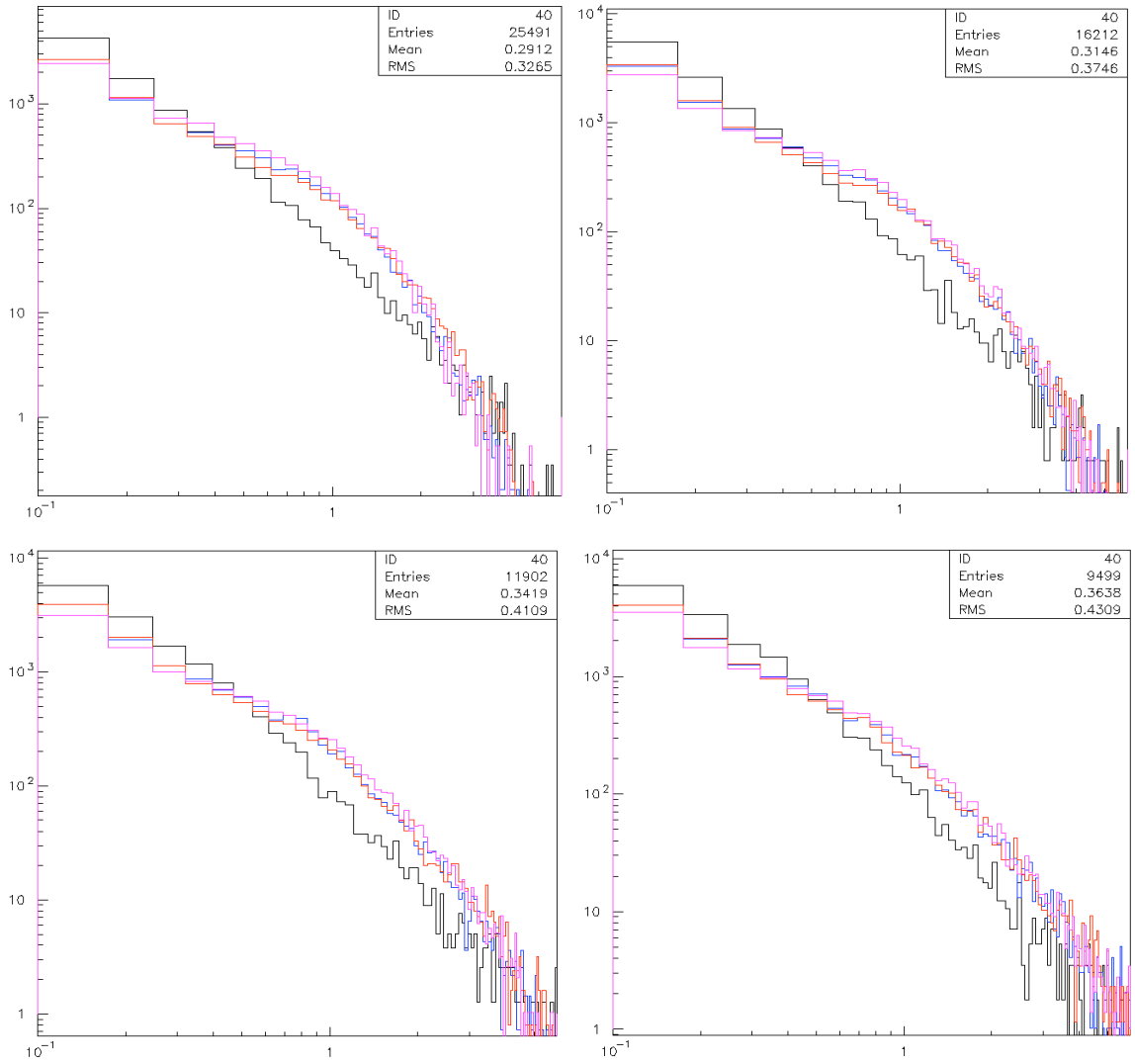

Figure 3.20: Distributions of $q_{i+1}-q_i$ for different Q *(VEM)* intervals (from left to right, top to bottom: [10, 20], [20, 30], [30, 40], [40, 50]) and for pure electromagnetic (black) traces and pure muonic traces from the standard (blue), half-muon (red) and double-muon (purple) sets. The data are normalised to 1000 traces.

In order to make sure that this result applies to the standard set alone (one might fear that the bias resulting from the use of the half-muon and double-muon sets be responsible for it), one considers in Figure 3.21 total traces (electromagnetic + muonic) for the standard set alone. In each Q interval one looks separately at three cases depending on the value taken by N_μ (0 to 5, 5 to 10 or 10 to 15). Here again, the number of jumps per trace is essentially fixed independently from N_μ once Q is restricted to a narrow interval.

In summary, when looking at data in a narrow Q interval, the values of J and N_μ are already strongly constrained and the knowledge of J does not help much to further constrain the value of N_μ. This result kind of discourages any attempt at improving the evaluation of N_μ using the method advocated in Section 3.2.

However, the present study brings up a new question: in real data, contrary to simulated data, the energy is unknown and a large Q value might result from a higher energy or from a higher N_μ; how can one tell between the two? The energy is estimated from *S(1000)* which is itself obtained by the values taken by Q in each of the tanks of a given event. The relation between energy and *S(1000)* is not the same for iron as for proton, but, of course, one does not know the nature of the primary. If N_μ and Q were strictly proportional and if the larger value of N_μ observed in iron data compared to proton data of the same energy were associated with an equally larger value of Q there would be no way to tell one from the other: the larger values of N_μ and Q could be interpreted as the result of a higher energy as well as of a more massive primary.

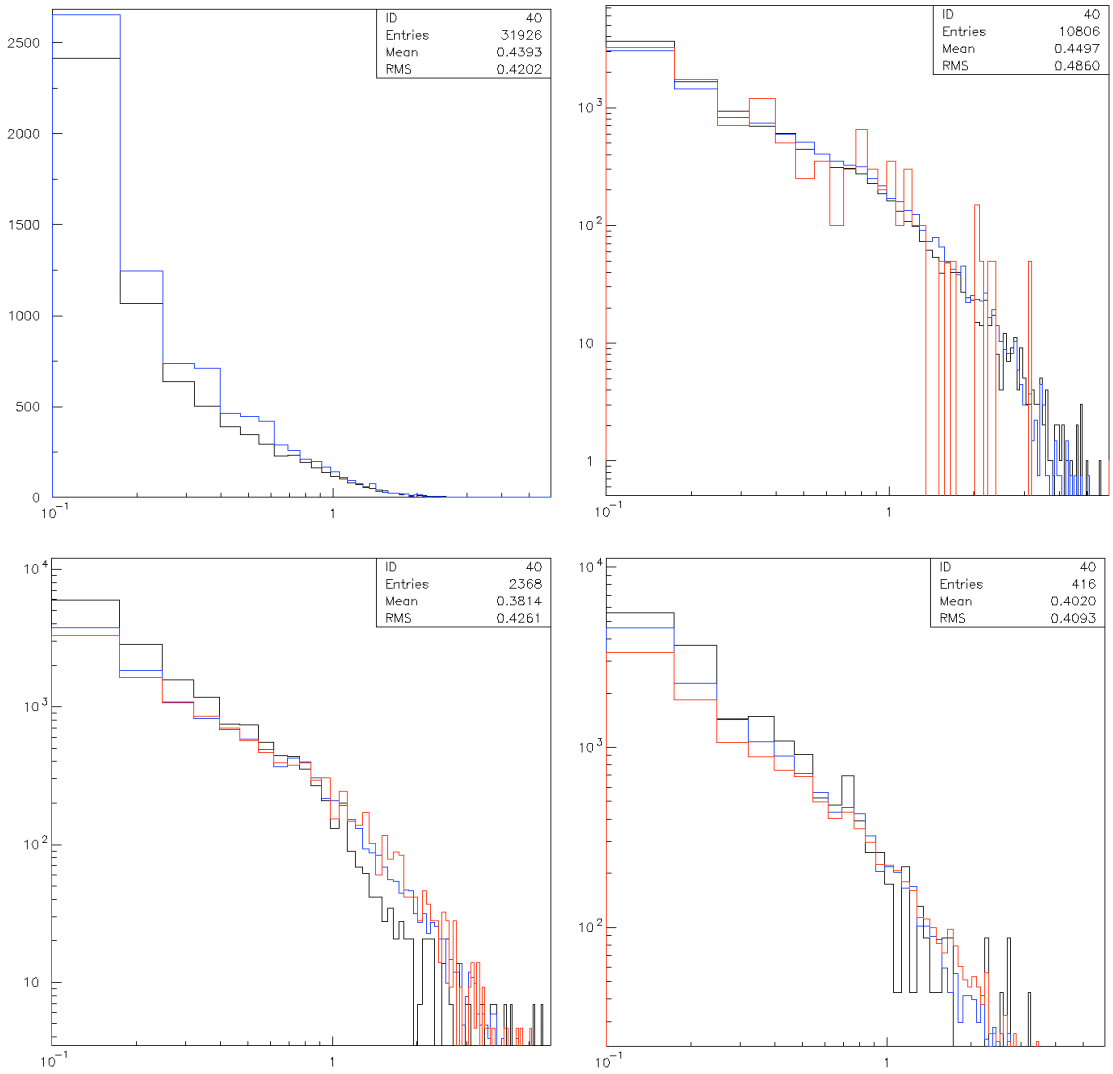

Figure 3.21: Distributions of $q_{i+1}-q_i$ for different Q *(VEM)* intervals (from left to right, top to bottom : [10, 20], [20, 30], [30, 40], [40, 50]) for traces of the standard set (em + μ) having different values of N_μ (0 to 5, black; 5 to 10, blue; 10 to 15, red). For Q between 10 and 20 VEM, there is no trace having N_μ >10. The data are normalised to 1000 traces.

The approximate proportionality between Q, J and N_μ should not come as a surprise. Apart from overlap corrections, J and Q must indeed be proportional for a same charge distribution of signals, whether electromagnetic or muonic.

The lesson to retain from this analysis is no longer to use form F' rather than from F but rather to look for a discriminator using the jump variable and having as little energy dependence as possible. This question is now addressed.

3.4.2 Looking for an energy independent iron proton discriminator

Two tools have been considered to reach approximate energy independence: the use of a $[D_1, D_2]$ cut and the use of normalised variables.

A preliminary study has shown that good discrimination was obtained using a cut $D_2\ (m) = 600 + 800\ log_{10}E(EeV)$ and $D_1=D_2/2$. There is not much to gain by increasing D_2 which anyhow has to stay below the trigger bias limit (Figure 2 of Reference 47). The discrimination is not very sensitive to the value of D_1: lowering D_1 brings more statistics but less discrimination. In what follows the above cut is applied throughout. In addition, tanks having a total charge Q in excess of 300 VEMs and showers having a zenith angle in excess of 53^o ($cos\theta < 0.6$) are discarded.

Table 3.1

$E(eV)$	θ	$<J>$ (VEM)		$<Q>$ (VEM)		$<J/Q>$ (%)	
		P	Fe	p	Fe	p	Fe
$10^{18.5}$	0^o	7.3 ± 0.4	9.6 ± 0.5	95 ± 5	124 ± 6	7.7 ± 0.2	7.9 ± 0.1
$10^{18.5}$	45^o	7.4 ± 0.4	8.9 ± 0.4	80 ± 4	83 ± 4	9.5 ± 0.2	11.1 ± 0.2
$10^{19.0}$	0^o	6.8 ± 0.3	8.6 ± 0.4	89 ± 4	110 ± 5	8.0 ± 0.2	8.1 ± 0.2
$10^{19.0}$	45^o	7.1 ± 0.3	9.3 ± 0.3	80 ± 3	96 ± 4	9.7 ± 0.2	10.6 ± 0.2
$10^{19.5}$	0^o	8.1 ± 0.4	9.0 ± 0.3	98 ± 4	108 ± 4	8.5 ± 0.2	8.7 ± 0.1
$10^{19.5}$	45^o	7.9 ± 0.2	9.7 ± 0.3	84 ± 3	97 ± 3	10.6 ± 0.2	10.9 ± 0.2

Two normalised jump–related variables have been considered: J/Q and $J/J_{1/4}$ where $J_{1/4}$ is defined as J by changing the threshold from 0.5 to 0.25 VEM. A comparison between these two discriminators did not give evidence for the latter to bring additional discrimination once the former has been used.

The dependence of the mean values of J, Q and J/Q on energy for each of the pertinent standard subsets is summarized in Table 3.1 above.

As a function of energy the average values of J are 8.3, 8.0 and 8.7 ± 0.2; of Q 96, 94 and 97 ± 3 and of J/Q 9.1, 9.1 and 9.7 ± 0.1 %. Within the limited statistical accuracy of the simulated data the three variables are indeed reasonably energy independent.

The strategy will therefore be as follows:

1. Select data in separate intervals of energy (meaning of $S(1000)$ within some small zenith angle dependent corrections). Apply $[D_1, D_2]$ and $cos\theta$ cuts.
2. In each interval fit J, Q and J/Q to forms $F = F_0+A(D-D_1)/(D_2-D_1)+B\ cos\theta$.
3. Calculate for each tank the quantities $\delta_J = J-F_J$, $\delta_Q = Q-F_Q$ and $\delta_{J/Q} = J/Q-F_{J/Q}$ and, for each shower, their weighted averages Δ_J, Δ_Q, $\Delta_{J/Q}$.

4. Compare in each interval the result obtained to that predicted by shower models using the same procedure.

Table 3.2

	F_0	A	B
J	17.2 ± 0.1	-17.2 ± 0.1	1.33 ± 0.08
Q	157.1 ± 0.6	-222.2 ± 0.9	78.3 ± 0.7
J/Q (%)	14.2 ± 0.1	3.3 ± 0.1	-7.9 ± 0.6

Table 3.3

$E(eV)$	θ	$<\Delta_J>$		$Rms(\Delta_J)$		S (%)
		p	Fe	p	Fe	
$10^{18.5}$	0^o	1.6 ± 0.3	3.9 ± 0.2	2.0	1.6	90 ± 14
$10^{18.5}$	45^o	0.4 ± 0.2	2.1 ± 0.2	2.2	1.9	58 ± 10
$10^{19.0}$	0^o	1.1 ± 0.2	2.7 ± 0.2	1.7	1.6	69 ± 12
$10^{19.0}$	45^o	0.2 ± 0.1	2.2 ± 0.2	1.4	1.5	97 ± 11
$10^{19.5}$	0^o	2.2 ± 0.2	3.8 ± 0.2	2.0	1.7	61 ± 11
$10^{19.5}$	45^o	2.7 ± 0.2	3.5 ± 0.1	1.6	1.2	40 ± 11

$E(eV)$	θ	$<\Delta_Q>$		$Rms(\Delta_Q)$		S (%)
		p	Fe	p	Fe	
$10^{18.5}$	0^o	-7.6 ± 2.6	20.0 ± 2.3	20	17	105 ± 13
$10^{18.5}$	45^o	-11.3 ± 2.5	-12.0 ± 2.0	25	19	-22 ± 101
$10^{19.0}$	0^o	-14.3 ± 2.0	5.6 ± 2.0	20	19	72 ± 10
$10^{19.0}$	45^o	-12.7 ± 1.5	0.5 ± 2.0	15	19	55 ± 10
$10^{19.5}$	0^o	-10.6 ± 1.9	10.3 ± 1.6	18	16	87 ± 10
$10^{19.5}$	45^o	1.5 ± 1.3	15.6 ± 1.3	13	13	77 ± 11

$E(eV)$	θ	$<\Delta_{J/Q}>$		$Rms(\Delta_{J/Q})$		S (%)
		p	Fe	p	Fe	
$10^{18.5}$	0^o	-0.76 ± 0.17	-0.37 ± 0.15	1.3	1.1	23 ± 13
$10^{18.5}$	45^o	-1.20 ± 0.23	1.06 ± 0.17	2.2	1.6	83 ± 10
$10^{19.0}$	0^o	-0.44 ± 0.19	-0.07 ± 0.15	1.9	1.5	15 ± 9
$10^{19.0}$	45^o	-0.57 ± 0.17	0.26 ± 0.15	1.7	1.5	37 ± 10
$10^{19.5}$	0^o	0.32 ± 0.19	0.39 ± 0.14	1.8	1.4	3 ± 9
$10^{19.5}$	45^o	-0.03 ± 0.14	0.25 ± 0.14	1.4	1.3	15 ± 11

The aim is not to get a better discrimination than obtained, for example, in Reference 47 but rather to cross check its results with a different approach and possibly different biases.

In the remaining of this section we illustrate the above strategy on the six families of the Monte Carlo standard set considered previously. For simplicity the same values of F_0, A and B are used for the three energies. They are given in Table 3.2.

To measure the quality of the discrimination between proton and iron we use a discriminator defined as $(<\delta_{Fe}>-<\delta_p>)/\sqrt{[rms^2(\delta_{Fe})+rms^2(\delta_p)]}$. It takes values of 42%, 34% and 12% for *J*, *Q* and *J/Q* respectively.

In a next step we extend the procedure to individual showers rather than individual tanks. Table 3.3 lists the mean and *rms* values of Δ for each of the six subsets previously considered in Table 3.1. Figure 3.22 shows the global distributions of Δ for the proton and iron subsets and for each of the three variables separately. The global discriminators take now values of 73%, 56% and 27% respectively.

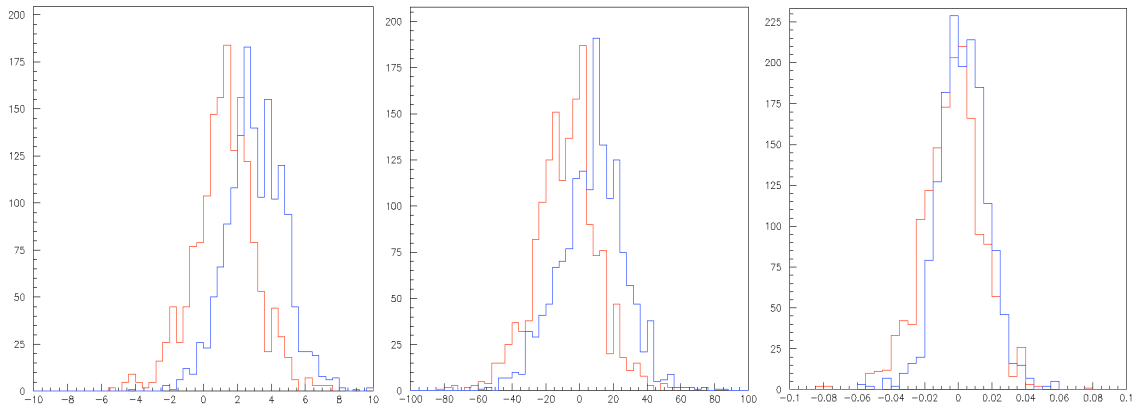

Figure 3.22: Distributions of Δ_J (left), Δ_Q (middle) and $\Delta_{J/Q}$ (right) for protons (red) and iron (blue).

3.5 An energy-independent analysis of Auger data

3.5.1 Introduction

The preceding section has underlined the importance of performing energy independent analyses when using the jump method. Another reason to do so is provided by recent results of the Pierre Auger Collaboration that suggest the possibility of an inconsistency between the interpretation of FD and SD data, precluding a reliable evaluation of the mass composition from the SD data alone. This was already commented upon in Section 4 and needs only to be briefly recalled here. In a nutshell, popular hadronic models using the primary energy as measured by the FD in a nearly model independent way [55] predict too small an SD signal. Moreover, there exist serious indications that the deficit is mostly affecting the muon component [51]. The situation is summarized in Figure 6 of the Lódz presentation of A. Castellina [52], which is, for convenience, reproduced in Figure 3.23 below. Using the FD energy scale, the amplitude of the muon component estimated from SD data is about twice that predicted for protons, while that predicted for iron is only 4/3 of that predicted for protons. A possible interpretation, explored in References 50 and 51, is that the FD underestimates energy by some 30%. Even so, the data still fall outside the proton-iron window. The present analysis contributes a new argument to this topic.

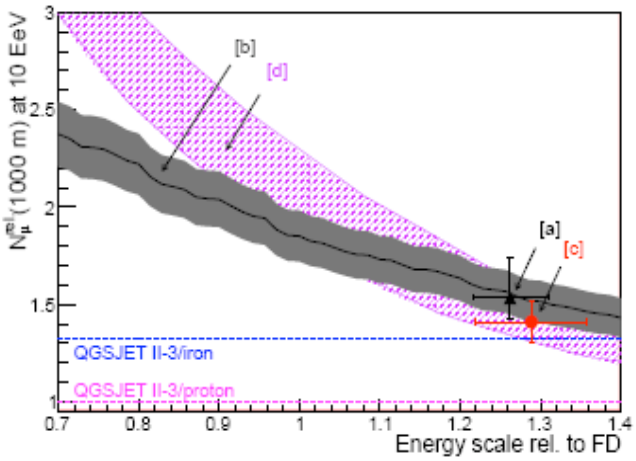

Figure 3.23: Number of muons at 1000 m relative to QGSJETII/proton vs. energy scale (relative to FD calibration) from [a] the universality method (triangle); [b] the jump method (filled area); [c] the smoothing method (circle); [d] the golden hybrid analysis (dashed area). The events have been selected for $log_{10}(E/eV) = 19.0 \pm 0.02$ and $\theta \leq 50^{\circ}$. According to the tested model, iron primaries give a number of muons 1.32 times bigger than that from protons (horizontal lines in the figure).

The main idea of the present analysis is to compare SD data with model predictions in an energy independent way. The comparison is made on variables that are sensitive to the muon fraction and, as such, are meant to be good discriminators between proton and iron primaries. In case of a disagreement, it could not be blamed on the FD energy scale but would provide evidence for a pure SD problem, either at the level of simulation (of the shower development and/or of the detector) or of data analysis proper. The variables under scrutiny here are:

– the total jump [4, 13, 14] in the FADC trace, *J*, here defined as usual with a threshold of 0.5 VEM.

– the total charge of the FADC trace, *Q*, with which, as has been seen in the preceding sections, *J* is found to be strongly correlated;

– their ratio *J/Q*, which was observed to be a very reliable – but not independent – discriminator;

The main phases of the analysis are described below:

– In a first phase, in each tank, the values of *J, Q* and *J/Q* are evaluated using the mean FADC trace, averaged over the three PMTs of the tank. Data retained for the present analysis are T4 triggers, 2008 PAO data. Showers having a zenith angle θ in excess of 53^{o} ($\cos\theta < 0.6$) are not considered and tanks having a total charge *Q* in excess of 300 VEMs are discarded from the analysis.

– A value of the energy, *E*, is evaluated from *S(1000)* using the standard algorithm [58] and only showers having *E* in excess of 3 EeV are retained. It must be clear that using the word "energy" here is nothing more than a semantic convenience, it does not imply any other knowledge than that of *S(1000)* and does not need any energy scale to be referred to. In particular, in the case of Monte Carlo events, the energy used to generate showers is ignored, *E* being again calculated from *S(1000)* in the same way as in real data. The *S(1000)* and *E* distributions are shown in Figure 3.24.

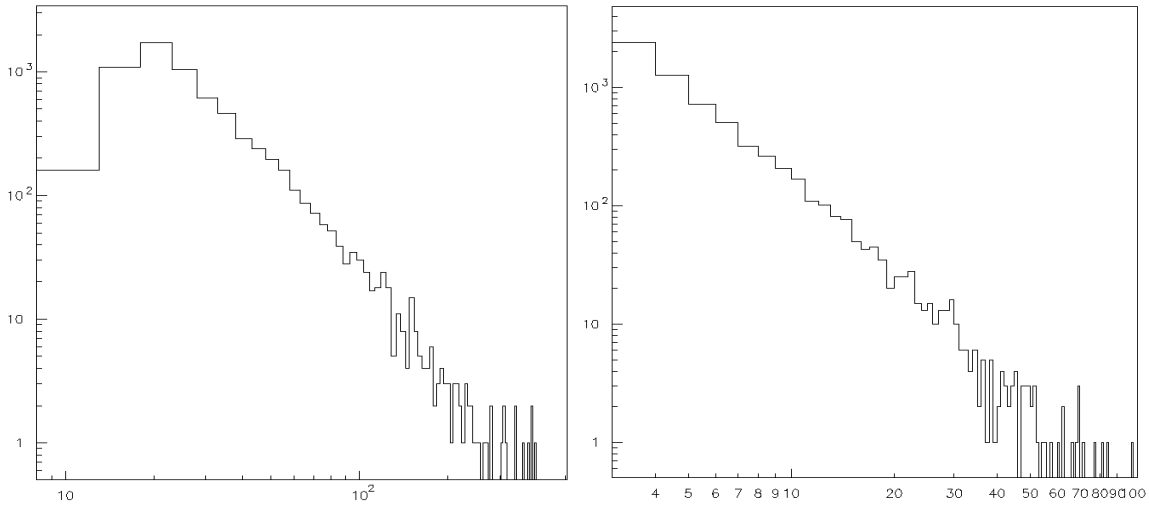

Figure 3.24: Measured distributions of *S(1000)* and *E* (respectively left and right) for the selected showers. Units are VEM and EeV.

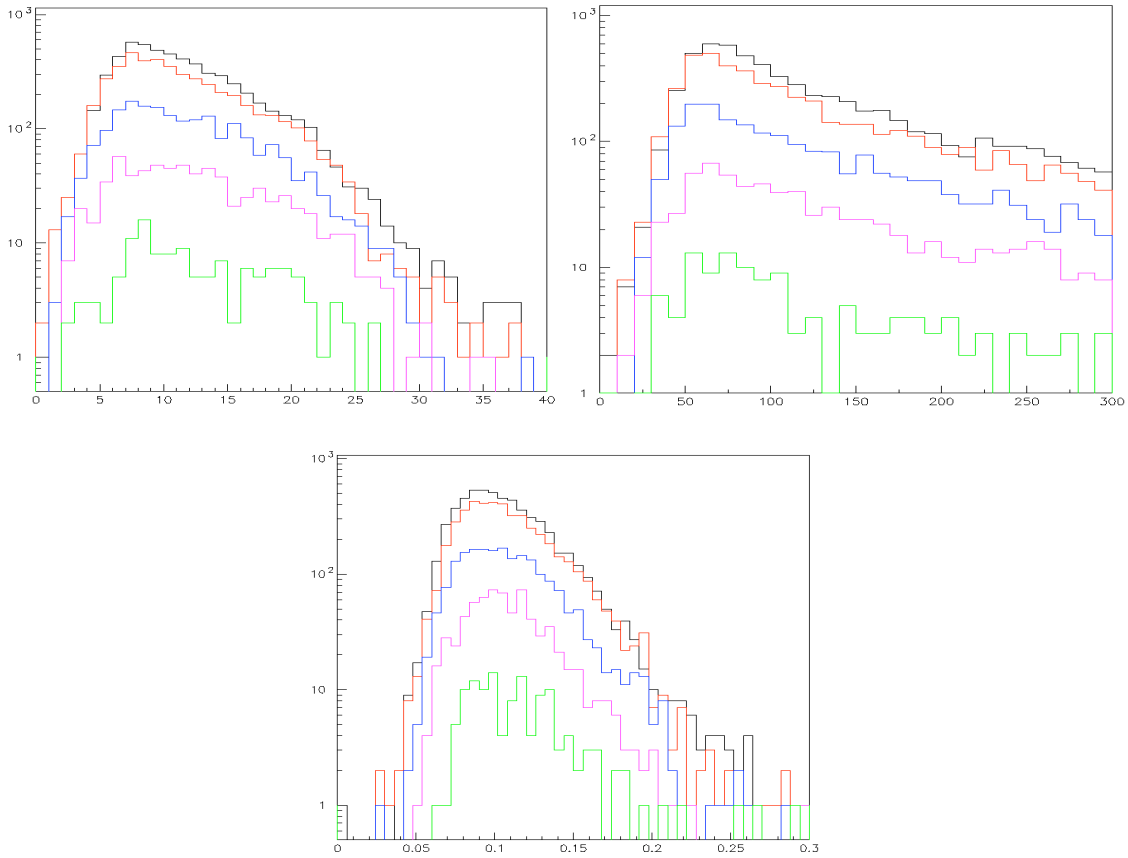

Figure 3.25: Distributions of the variables *J, Q and J/Q* (respectively upper left, upper right and lower panels) for selected tanks of selected showers. The distributions in each of the five energy intervals (see text) are displayed separately, the lower the energy, the higher the population. Units are VEM and bin of 25 ns The energy intervals are 3 to 4.64, 4.64 to 10, 10 to 21.5, 21.5 to 46.4 and > 46.4 EeV.

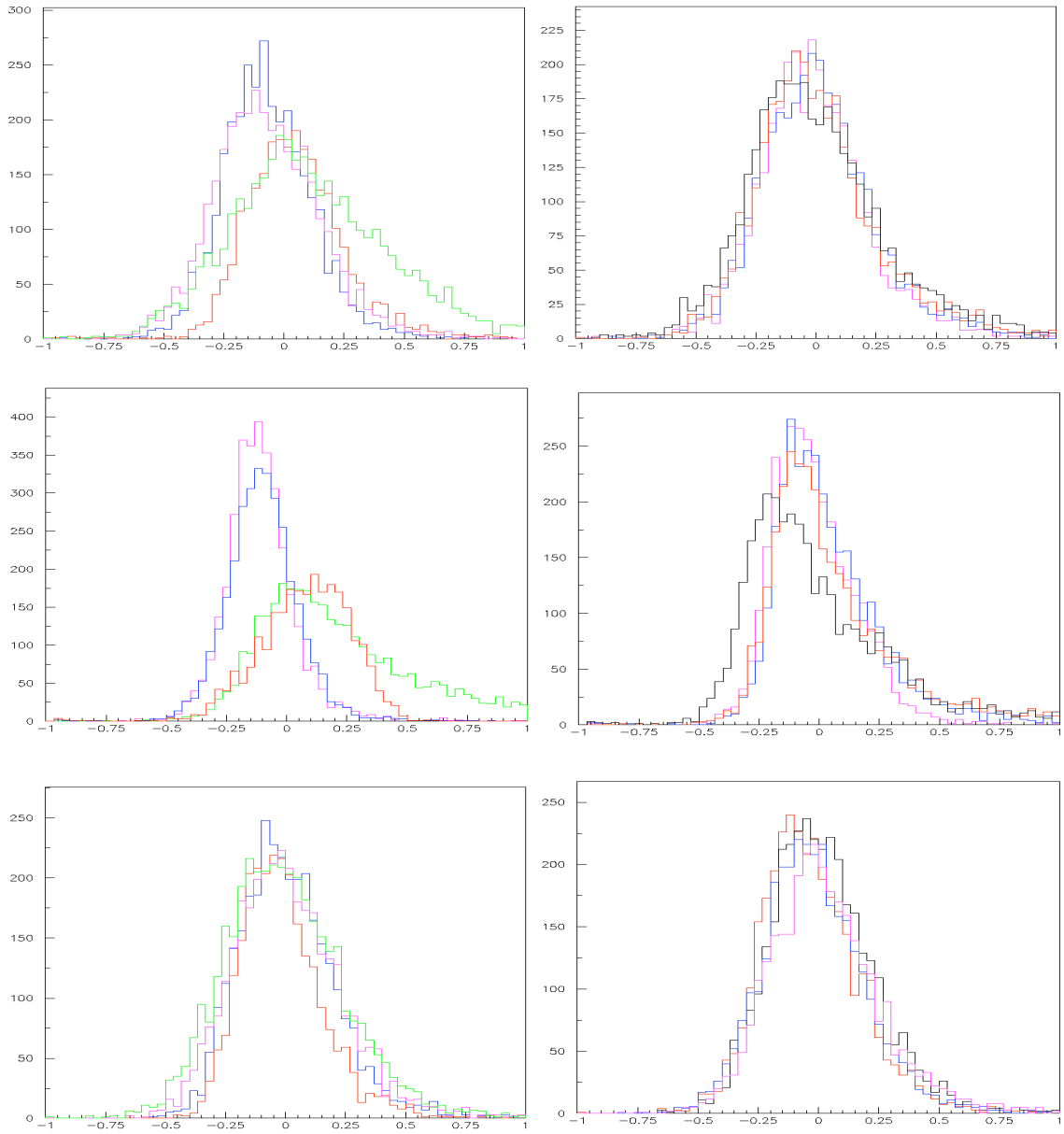

Figure 3.26: Deviations from unity of the normalized values of *J*, *Q* and *J/Q* (top to bottom) over the whole energy range as functions of *x* (left) and *cosθ* (right). The *x* intervals are 0 to 0.4, 0.4 to 0.6, 0.6 to 0.8 and 0.8 to 1. The *cosθ* intervals are 0.6 to 0.7, 0.7 to 0.8, 0.8 to 0.9 and 0.9 to 1.

– An interval $[D_1, D_2]$ is defined, in which to confine the distance D to the shower axis of the Cherenkov tanks considered in the analysis. The upper limit is such as to avoid trigger biases and the lower limit to provide good discrimination between proton and iron showers. Moreover, the interval is made to evolve as a function of $S(1000)$ for the mean values of J and Q to remain approximately constant [57]. More precisely:

$$D_2\,(m) = 600 + 800\,\log_{10}E(EeV) \qquad (1)$$

$$D_1 = 0.5\,D_2.$$

In fact, the cut on the total charge (Q<300 VEM) depopulates a low D band of the $[D_1, D_2]$ interval nearly equivalent to having $D_1 = 0.6D_2$.

For convenience, E intervals are defined in geometric progression with three bins per decade. The distributions of each of the variables under study in each of the E intervals are displayed in Figure 3.25. As expected, J, Q and J/Q are found to be energy independent.

– Functions of D and of zenith angle θ of the form $F = F_0+Ax+B\ cos\theta$, where $x=(D-D_1)/(D_2-D_1)$ and where F stands for J, Q and J/Q are fitted to the real data and used as a reference. Each of the variables J, Q and J/Q is from now on measured in units of these functions. The same reference is used for the Monte Carlo events. The quality of the fits is good as illustrated in Figure 3.26 showing the deviations from unity of the normalized values of J, Q and J/Q over the whole energy range as functions of x and $cos\theta$ separately. It must be noted, however, that a bad quality fit would not introduce any bias but simply smear the data and therefore deteriorate the discriminating power of the variable.

3.5.2 Results

The mean values of the deviations from unity of the normalized variables J, Q and J/Q have been evaluated for both real data and Monte Carlo simulated showers. Monte Carlo events have been processed in the very same way as the data. For both data and Monte Carlo the values measured in the different selected tanks of a same shower have been averaged. The Monte Carlo events used here [59], proton and iron primaries separately, were generated by QGSJET in Corsika, converted by the official Auger Offline software into FADC traces and selected according to exactly the same criteria as for real data: same cuts on Q, D and θ, same way to calculate E from $S(1000)$. They were generated at several zenith angles and energies. While no use is made in the present analysis of the values of the generated energies, it is important to notice that the $S(1000)$ algorithm grossly underestimates the energy of Monte Carlo events, by nearly a factor 2.

A common feature is that J and J/Q data fall outside the window predicted by the model for a mass range spanning from proton to iron. This result is obtained in each energy interval separately. It is also obtained when one (wrongly) uses the generated energy in the Monte Carlo simulation to calculate D_1 and D_2, giving confidence that the conclusions of the present analysis are robust and bias free.

Table 3.4

	$<J>-1$	$<Q>-1$	$<J/Q>-1$
Data	0.015 ± 0.004	0.046 ± 0.005	0.001 ± 0.004
Proton MC	-0.198 ± 0.007	-0.005 ± 0.009	-0.165 ± 0.007
Iron MC	-0.134 ± 0.007	0.011 ± 0.009	-0.112 ± 0.006

In Reference 57, the values of D_1 and D_2 had been calculated using the generated energy and Q had been found to discriminate between iron and protons. Here, on the contrary, where D_1 and D_2 are calculated from E, namely from $S(1000)$, Q takes nearly the same values in both proton and iron Monte Carlo events.

Table 3.4 summarizes the results for the second energy interval and Monte Carlo events generated at 10 EeV and populating the corresponding *S(1000)* range. Including other energy ranges, be it in real or in Monte Carlo data, does not change significantly the results.

For each variable V, it is convenient to define a quantity $\lambda=(V_{exp}-V_p)/(V_{Fe}-V_p)$, where the meaning of the subscripts is obvious and which provides a measure of the disagreement between data and predictions: one would expect λ to be somewhere between 0 and 1, 0 for pure proton primaries and 1 for pure iron primaries.

It is sufficient at this stage to retain the *J/Q* value which is known to be particularly bias free and robust against changes in the details of the analysis. This value is $\lambda=3.13\pm0.40$. The uncertainty $\Delta\lambda$ has been calculated as $\Delta\lambda=\{\Delta V_{exp}^2+(\lambda\Delta V_{Fe})^2+([1-\lambda]\Delta V_p)^2\}^{1/2}/|V_{Fe}-V_p|$. This result, representative of those obtained in other energy intervals and for *J*, is similar to those [52] of Figure 3.23 when the energy scale is adjusted to match the FD calibration. However, in the present analysis, an interpretation in terms of an underestimated energy scale can no longer be retained.

As the disagreement between data and model predictions cannot be disposed of by claiming an underestimated FD energy scale, it must be blamed on the SD alone: possibly on errors in the present analysis, or on imperfections of the SD simulation or in inadequacies of the hadronic model. In the latter case, it is interesting to remark that analyses measuring directly the longitudinal profile [51, 52, 55], such as the FD measurement of X_{max} or the SD measurement of the azimuthal asymmetry of the rise time (sensitive to the position of the end tail of the longitudinal profile) do not seem to suffer from the present disease and find values of λ between 0 and 1 (getting nearer to 1 as energy increases). This might suggest that the problem lies with the hadronic models predicting too steep a lateral distribution function of muons. It might also reveal errors in the detector simulation and/or in the present analysis.

If one blames the large measured value of λ on the simulation under-evaluating the value of *J/Q*, one may obtain an estimate of the corresponding factor by assuming some mixture of iron and protons in the real data, say 60%/40% as suggested by the longitudinal profile analyses. Then the normalized $\langle J/Q\rangle$ value predicted by the simulation becomes 0.867±0.007 compared to 1 in the data. This would therefore suggest that the simulation underestimates $\langle J/Q\rangle$ by ~15%. Indeed, the *rms/mean* values predicted by the simulations, ~16% for iron and ~18% for protons, are in perfect agreement with the value of 17% measured in real data, giving support to such an interpretation.

3.5.3 Conclusion

Obviously, checking the results of the present study (as well as those mentioned in Reference 52 which have been using the same Monte Carlo simulation) with independently generated Monte Carlo events is highly desirable. Particular attention should be given to accurate comparisons of the lateral distribution functions predicted for proton and iron primaries with that

experimentally measured. It should also be understood why the reconstructed energy is nearly twice as small as that generated.

In summary, the present analysis has contributed an additional argument to the well established fact [51, 52, 55] that commonly used hadron interaction models, combined with a simulation of the surface detector, fail to reproduce the data, in particular those that are sensitive to the amplitude of the muon component. An important feature of the present analysis is to be explicitly independent from any energy scale, excluding that the observed disagreement could be blamed exclusively on the FD underestimating energies by ~30%. This is at variance with former analyses, such as the constant-intensity-cut method [51], which can be interpreted as providing an energy calibration of the SD independently from the FD energy scale. Here, the disagreement between measurements and predictions can only be blamed on possible errors in the present analysis or on inadequacies of the simulations (detector and/or hadronic model). In particular, a possible interpretation would be that the simulation underestimates the value of J/Q by some 15%.

3.6 Cen A correlated showers

3.6.1 Introduction

Motivated by the remark [60] that a significant fraction of UHECRs detected by the surface detector (SD) originate from the neighbourhood of Centaurus A (Cen A, RA=204.1^o, DEC=−43.0^o, the closest AGN from Earth) and that it is much easier for a proton than for an iron nucleus to be seen as pointing to its source (because of magnetic bending in the disk of the Milky Way) the present study looks for a possible difference in muon content between the showers pointing to Cen A and those of the whole sky. It aims at providing additional information of relevance to a recent X_{max} analysis [61] using Auger hybrid data, which suggests that the average atomic mass of the highest energy UHECRs pointing to Cen A within 18^o be higher than that of the whole sky (X_{max} is the depth in the atmosphere at which the development of an extensive air shower is maximal). This result is puzzling because one would expect light primaries to be associated with an accurate pointing and massive primaries to be angularly deviated from their source by the magnetic field in the disk of the Milky Way.

Using Auger SD data, the muon contents of the Cen A and whole sky data samples are now compared.

3.6.2 Data set

Data retained in this study are the T5 trigger Auger SD data having energy $E > 4$ EeV, zenith angle $\theta < 60^o$, recorded from January 1, 2004 to April 26, 2010. Shower events are reconstructed by the Auger Observer programme v2r6p2. There are 29703 such showers. Figure 3.27 shows their energy and zenith angle distributions.

Showers pointing to Cen A within 18^o are called Cen A events. Several studies [60, 62, 63] have shown that there is an excess of events within 18^o from the

centre of Cen A at energies exceeding 52.5 EeV. For convenience, and to ease comparison with the earlier X_{max} analysis [61], this definition of Cen A events uses an energy independent angular region around Cen A ; however, at energies lower than 52.5 EeV, the magnetic field in the disk of the Milky Way makes the correlation with Cen A less reliable.

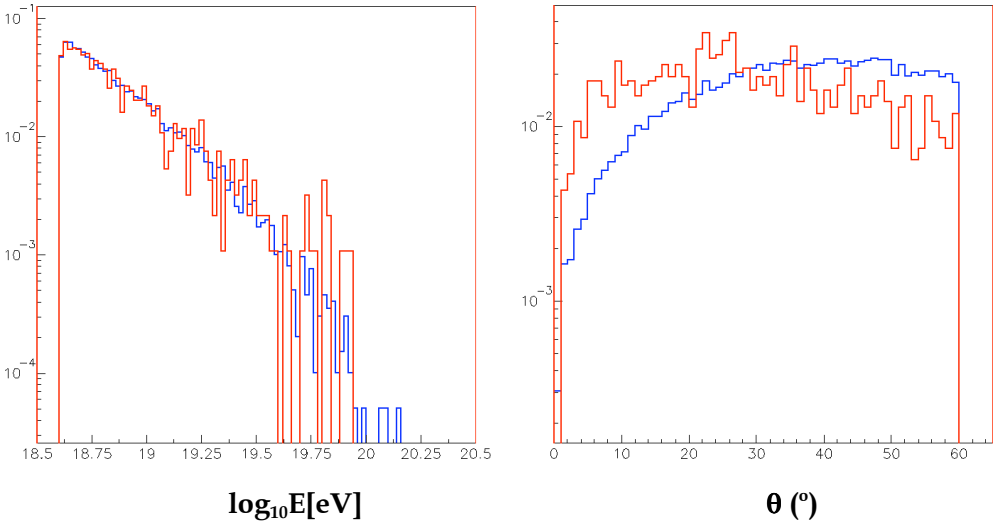

Figure 3.27: Normalized energy (left) and theta (right) distributions of the whole sky (blue) and Cen A (red) samples.

3.6.3 Muon densities at 1000 meters from shower axis: Cen A and whole sky data samples

We first apply the standard jump analysis using as proton/iron discriminator muon densities at 1000 meters from shower axis, $\rho_\mu(1000)$, as described in Reference 56, the Cen A and whole sky data samples being considered separately in the same spirit as was done by the Prague group with X_{max} using Auger hybrid data in an elongation rate analysis [61].

For each shower, the value of $\rho_\mu(1000)$ is calculated as follows:

– In a first step, the number of muons, N_i, measured by each water Cherenkov tank hit by the shower is evaluated using the jump method [47, 57].

– In a second step, the numbers of muons of all the tanks hit by the shower are fit to a common form, $N_i=N_{1000}(r_i/1000)^\beta$. Here, N_{1000} (the number of muons at 1000 m) and β (the power index, required to be negative) are two adjustable parameters; r_i is the distance from tank i to the shower axis. A number of requirements have been applied in order to evaluate N_{1000} reliably: there must be at least four tanks hit by the shower (excluding saturated signals) and the r_i span covered by the retained tanks must exceed 750 m. Moreover, the rejected events (both Cen A and whole sky) of the highest energy bin have been individually inspected and eventually rescued when it was clear that the evaluation of N_{1000} was reliable.

– In a final step, the muon density at 1000 m, $\rho_\mu(1000)$, is calculated by dividing the interpolated number of muons at 1000 m, N_{1000}, by the water

Cherenkov tank's cross section as seen in the direction of the shower axis, $S=\pi R^2_{tank}cos\theta+2R_{tank}h_{tank}sin\theta$ where $R_{tank}= 1.8\ m$ is the radius of the SD tank and $h_{tank}= 1.2\ m$ is its height.

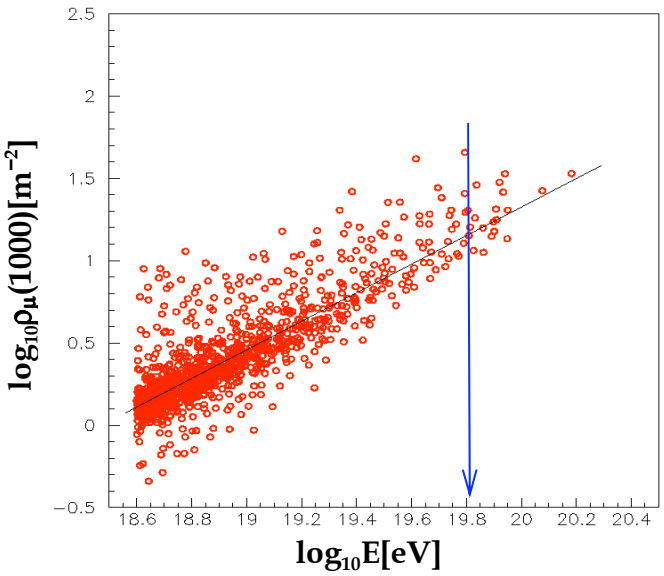

Figure 3.28: Energy dependence of the muon density at 1000 m. The blue arrow shows the energy threshold E_{thresh} = 52.5 EeV.

The value of $\rho_\mu(1000)$ increases with energy because of the larger particle density on ground. Figure 3.28 displays the energy dependence of $\rho_\mu(1000)$ in log-log scale. The fit, of the form $A+Blog_{10}(E[eV])$, gives A = −16.034 and B = 0.864 or $\rho_\mu(1000) = 0.389E^{0.864}$. The best fit is shown as a black line.

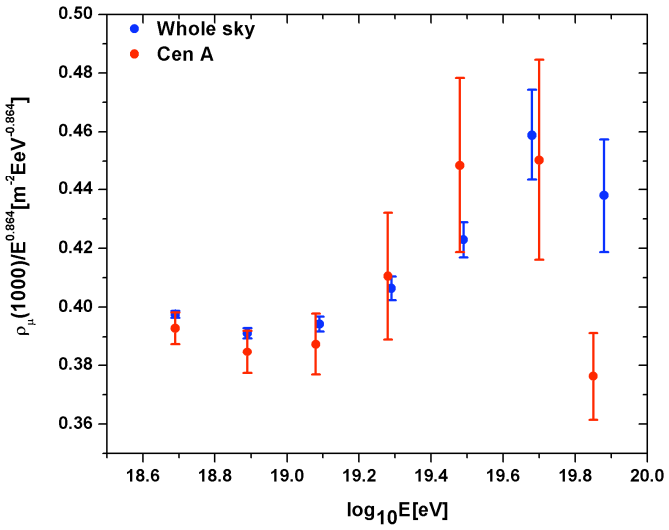

Figure 3.29: Energy dependence of muon density at 1000 m divided by $E^{0.864}$. The blue dots are of the whole sky sample and the red ones are for Cen A.

Figure 3.29 shows the dependence of $\rho_{eff}=\rho_\mu(1000)E^{-0.864}$ on $log_{10}E[eV]$ for both data samples, Cen A and the whole sky, separately. The data are distributed in bins of $log_{10}E[eV]$ having a width of 0.2. It is interesting that ρ_{eff} reaches a

minimum around $E_0=10^{19.0}$ eV, suggesting a possible change in mass composition to heavier masses around E_0. It is obvious from the figure that there is no significant difference in the ρ_{eff} values of the two samples, except in the last energy bin where, however, the Cen A statistics is very low (9 events having $log_{10}E[eV]>19.8$ collected together). Averaging ρ_{eff} above 52.5 EeV gives 0.414±0.027 for CenA events and 0.442±0.018 for the whole sky which differ by only 0.83 standard deviations. One should note that while this difference is not statistically significant, its sign is opposite to that which one would expect from the analysis of Reference 61.

At lower energies, and at variance with the results of Reference 61, the muon density analysis does not show a significant difference in ρ_{eff} between Cen A and whole sky. It must be noted that SD data, having much higher statistics than hybrid data, extend to much higher energies (by nearly one order of magnitude): the energy spectrum of the Cen A events used in Reference 61 stops around $log_{10}E[eV] = 19.1$ while that of the SD data stops around $log_{10}E[eV] = 19.9$. However, the significance of the SD result depends on the sensitivity of ρ_{eff} to the muon content and of the muon content to the mass composition.

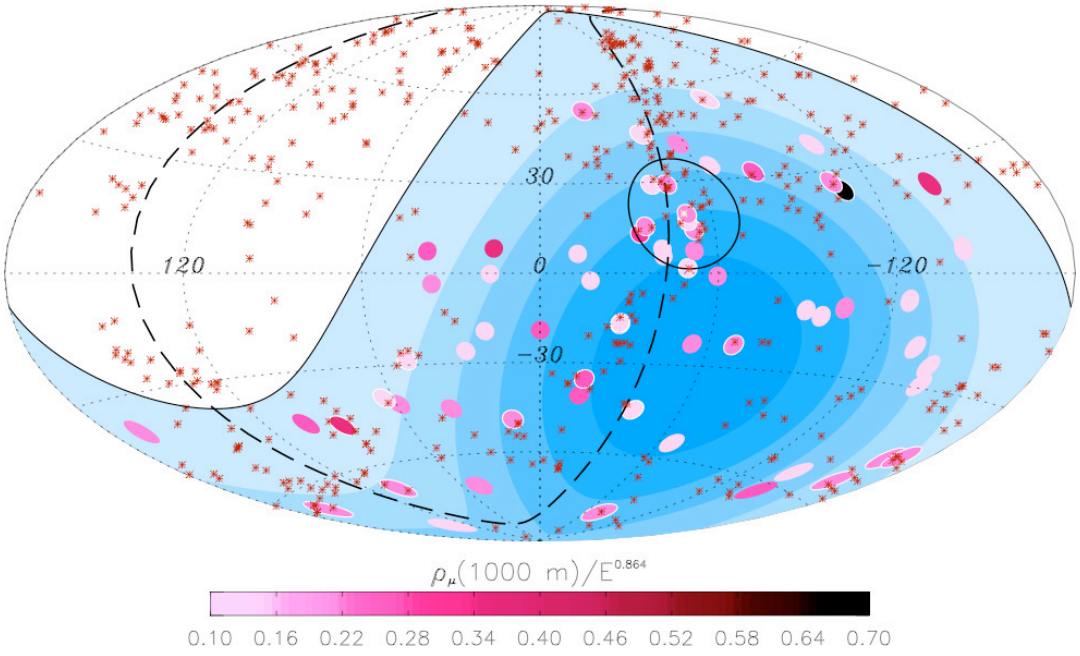

Figure 3.30: Sky map of the 65 highest energy Auger events (full disks), with energies exceeding 55 EeV. AGNs from the VC-V catalog having a redshift $z\leq0.018$ are shown as red crosses. The black circle shows the region within 18° of Cen A. The colour of the disks is a measure of ρ_{eff} (pale meaning muon poor and dark meaning muon rich, see colour scale).

Having evaluated the muon densities of the highest energy events makes it possible to look at their distribution in the sky. Does one see clusters of muon rich (or poor) events? Figure 3.30 shows the sky map of the SD events having $E > 55$ EeV, the presently calibrated energy at which correlation between UHECRs and AGN was established by the Auger Collaboration [44] in 2007 (it was 57 EeV at the

time). The sky map shows no evidence for clusters of muon rich events but one must remember that no mass assignment can be reliably made on a shower-by-shower basis. It is interesting to note the presence of events not correlated with AGNs but coming from voids, quite far from the closest AGN; several such events are relatively muon poor (therefore on the proton side, having in principle a reliable arrival direction). Which are the sources of such events?

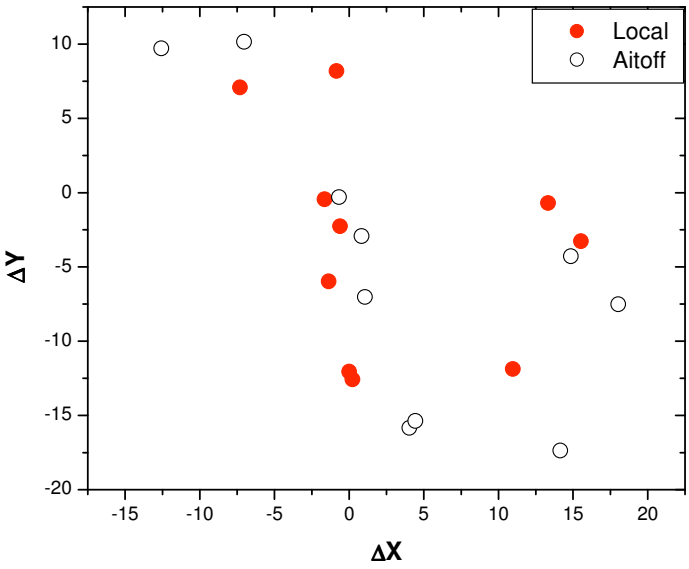

Figure 3.31: Sky map of the Cen A sample (see text).

Figure 3.31 shows the sky map of the Cen A events. Coordinates are in degrees. The red points are measured in equatorial coordinates with respect to Cen A, and taking the North in the Δx direction. The open circles are the Aitoff projection in galactic coordinates, again centred on Cen A. As expected, they are slightly distorted with respect to the former. More statistics will be needed to see whether the apparent alignment of the seven showers on the left is confirmed.

3.6.4 Separation between the Cen A and whole sky sample as compared to that expected between iron and proton primaries

In the previous section, the number of muons was evaluated in each tank as $N_\mu = CJ$ where J is the sum of the jumps in the mean FADC trace exceeding 0.5 VEM-peak and C is a scale factor obtained from Monte Carlo simulation of the shower development [56]. In the present section, an effort is made to quantify the significance of the observed similarity between the Cen A and whole sky jump distributions. The analysis is restricted to tanks located at moderate distance D to the shower core, where the discrimination between iron and proton primaries has been shown to be optimal [57]. Precisely, D is required to be in a window $D[m] \in [D_1, D_2]$ where $D_1[m] = 393 + 650 \log_{10} E[EeV]$ and $D_2[m] = 753 + 770 \log_{10} E[EeV]$ respectively. This choice of a D window was made to optimize the separation between Monte Carlo proton and iron jump distributions; the values of the separation achieved, as evaluated from simulated showers, are 38±7%, 29±5% and

31±4% at 3.2, 10 and 32 EeV respectively. Moreover, the comparison between the Cen A and whole sky samples is made directly on J, without evaluating N_μ. In the energy range of interest here, $S_{Fe,p}$ ~31% implying that one needs a sample of at least 17 events to tell iron from proton to within 3 standard deviations.

The data are distributed in three energy bins (40 to 57 EeV, 57 to 78 EeV and > 78 EeV) and the mean jump value is found to be nearly energy independent, a linear fit giving $\langle J\rangle = 8.6\,(1 + 2.33\,10^{-3}\,E)$ with E measured in EeV.

Figure 3.32 shows the jump distributions for Cen A and whole sky events separately and for showers having energy in excess of 55 EeV. Each tank located in the proper D window is an entry in the distribution. The jumps have been corrected for the slight energy dependence of $\langle J\rangle$. An analysis using J/Q rather than J as a discriminator has also been performed and has given essentially the same result. There are 105 (resp. 463) tanks in the Cen A (resp. whole sky) sample, with an average of about 11 tanks per shower.

Both samples have similar jump distributions, the mean jump values being *8.29±0.48* for the Cen A sample and *9.19±0.22* for the whole sky, giving $\{\langle J\rangle_{CenA} - \langle J\rangle_{Wholesky}\}(\sigma^2_{CenA} + \sigma^2_{Wholesky})^{-1/2} = -18\pm6\%$ compared with *31±4%* for the iron-proton separation. Even if, in this energy domain, the whole sky sample where purely iron, the present result gives an average mass composition slightly closer to protons than to iron (1.9 compared to 2.6 standard deviations). If the mass composition of the whole sky is equivalent to ~40% proton ~60% iron, as suggested by the most recent elongation rate analyses [55], protons would be clearly favoured by the Cen A sample: 0 standard deviations compared with 5 standard deviations for a pure iron hypothesis. The Cen A sample favours therefore protons over iron within the limited statistics available, at variance with what would be expected from the analysis of Reference 62. A limitation of the present analysis is the relatively scarce sample of simulated showers on which it is based. Using a larger sample, possibly generated with different hadronic models, would help in giving confidence in the reliability of the present result.

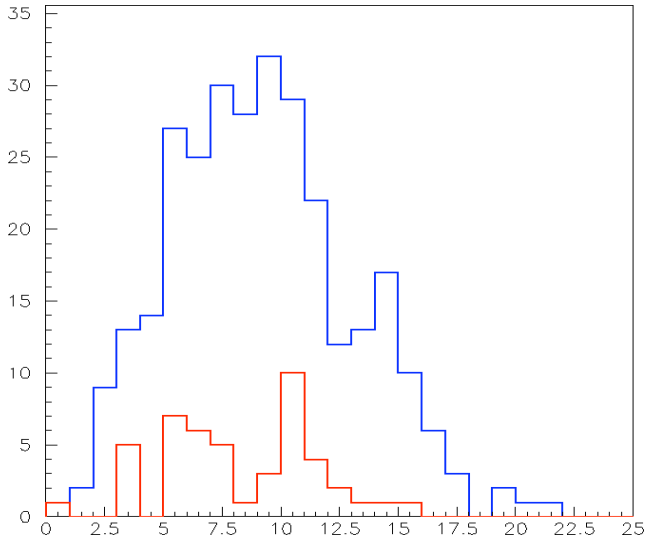

Figure 3.32: Jump distribution (measured in VEM, jump threshold set at 0.5 VEM) for the Cen A (red) and complementary (blue) samples (E> 57 EeV).

3.6.5 Conclusions

We have studied the muon content of UHECR showers using the Auger surface detector, separating out Cen A correlated showers with the aim of learning about a possible difference in mass composition. Two different applications of the jump method, with quite different sources of systematic errors, have been used. No significant difference between the Cen A and whole sky samples has been found at variance with the result of an X_{max} analysis using hybrid data [61]. While the SD data sample has much lager statistics than the hybrid sample, the sensitivity of the jump method to the primary mass composition is moderate and, with the present statistics, the limit that can be placed on a possible Cen A vs whole sky difference is only 58% of the difference expected between iron and proton primaries. Yet, with such limited sensitivity, a proton hypothesis is always preferred to an iron hypothesis. Assuming a 60% iron, 40% proton average composition for the whole sky in the energy range of relevance, the Cen A data would disfavour an iron hypothesis by five standard deviations while being perfectly compatible with a proton hypothesis. This result is clearly at variance with that presented in Reference 61.

However, this result rests on the assumption that it makes sense to compare the measured separation between the whole sky and Cen A with the simulated separation between iron and proton primaries. As seen in section 3.5, the failure of the simulation to properly describe the data sheds serious doubts on the validity of this assumption.

Ignoring the predictions of the simulation but taking as granted that iron primaries are associated with a larger muon density on ground than proton primaries (in the D range considered here), all that can be said is that the Cen A sample is more proton-rich than the whole sky sample and that the difference is a three standard deviations effect. Nothing more can be said without making additional assumptions.

One might assume that the whole sky sample is, say, 60% iron and 40% proton on the basis of the longitudinal profile analysis. But this is not sufficient to make a quantitative evaluation of the Cen A mass composition. What is needed is the scale that relates separation to mass composition and knowing the mass composition of the whole sky sample does not tell us what this scale is.

While having given evidence for a three standard deviation effect in the comparison Cen A vs whole sky, the analysis has not really clarified a situation that remains confused. Yet, the fact that showers pointing back to their source are very likely to be proton showers, otherwise the magnetic field in the disk of the Milky Way would prevent a good match, remains a serious argument to be taken in due consideration. Assuming that the Cen A sample is indeed pure protons and assuming that the whole sky sample is a proton-iron mixture (as suggested by longitudinal profile analyses), one can calculate the iron proton separation, which one finds in good agreement with the prediction of the simulation. As in the general case studied in Section 3.5 in the case of J/Q, this may suggest that the simulation underestimates the jump value by a constant factor, giving therefore a correct estimate of the separation.

3.7 Conclusions

It is now time to summarize what has been learned in the present section.

After a brief introduction in Section 3.1, Section 3.2 was used to get some familiarity with the relation between the total jump J and the properties of the FADC trace. In particular, it was realized that in order to have a chance to learn something sensible about the number N_μ of muons contributing to an FADC trace, it was necessary to restrict the observation to tanks not too close to the shower axis. From a separate study of muon and electron/photon traces, J was found to be approximately proportional to N_μ and respectively Q (the total charge), which did not come as a surprise. Combining electron/photon and muon FADC traces has shown that J could be fit to a form $J=\{(43.9\pm0.5)10^{-3}Q+(200\pm2)N_\mu\}10^{-3}$.

Section 3.3 has studied the separation which could be expected from a measurement of J between a sample of tanks detecting proton induced showers and a sample of tanks detecting iron induced showers. It was remarked that even when knowing N_μ exactly (which of course is not possible) the iron-proton separation never exceeds 30%. This gives a measure of the correlation between the nature of the primary and the density of muons on ground. It implies that to make a statement on the identity of the primaries to three standard deviations requires a sample of at least 50 tanks. It was also remarked that if the energy of the primary were known, not only J but also Q and N_J (the number of jumps in the trace) would be good proton-iron discriminators.

However, the energy of the primary is unknown and Section 3.4 has revealed that the inversion of the relation $J=AQ+BN_\mu$ into $N_\mu=\alpha J+\beta Q$ – with the aim to obtain N_μ from Q and J – is not straightforward. The problem is the existence of such a strong correlation between Q and J that there is essentially nothing to gain by using the above binomial form. An important corollary of this strong correlation is the difficulty to tell the difference between, say, two proton showers of different energies and proton and iron showers of the same energy. In order to overcome this difficulty, the use of an energy-independent discriminator is mandatory. Two tools have been used to this aim: using J/Q as a discriminator, and restricting the analysis to tanks located within a range of distances to the shower axis depending on $S(1000)$. It was shown on simulated events that both were individually successful.

Section 3.5 applied this energy independent analysis to real PAO data and confirmed the misfit with the predictions of shower model simulations. Moreover, it established an important new result: this mismatch can not be resolved by a simple rescaling of the relation between $S(1000)$ and energy. It was also remarked that the mismatch could simply be described as the simulation underestimating the value of J/Q by only ~15%.

Finally, Section 3.6 presented a jump analysis making use of the above knowledge and applied to ultra high energy showers originating within 18^O from Cen A. At variance with a recent elongation rate analysis using hybrid data, it favours a proton origin for Cen A associated showers when compared with the whole sky.

The present study has illustrated the difficulty to identify the nature of the primary using SD data. The lack of consistency between data and simulation is a

real concern and more work will be required to sort it out. One cannot be satisfied with blaming the models used in the simulation unless the physics mechanism of relevance is clearly understood. The sophisticated codes traditionally used to simulate shower development lack transparency and make it very difficult to identify with confidence the phenomena of relevance. The remaining part of the present work is a step toward the development of a very crude, but transparent shower development simulation, in the hope that it could shed new light on the problem.

Chapter 4

SIMULATION OF ELECTROMAGNETIC SHOWERS

4.1 Introduction

The preceding section has shown the need for a better understanding of the development of ultra high energy air showers. Precisely, the mismatch between the measured muon density on ground and the prediction of popular shower development models calls for a clear understanding of the parameters of relevance to muon production. The available shower models [19] combine experimental knowledge, acquired at high energy colliders, and theoretical knowledge, inferred from QCD, in different mixes. They all have reached a high degree of sophistication and include detailed descriptions of the underlying physics. While being very precious tools for the analysis of cosmic ray data, they are also kind of black boxes, the use of which is somewhat heavy. The aim, in the present and following sections, is to develop a shower model where identifying and tuning the parameters of relevance is easy and transparent. As the emphasis is on the evaluation of the primary mass, what we shall be after is essentially a comparison between light, say protons, and heavy, say iron, primaries. A toy model approach should then be sufficient to the extent that the effects of the gross approximations that it implies cancel in the comparison.

Extensive air showers are made of several components. A major component is a set of electromagnetic showers induced by the decay photons of neutral pions. Whenever a neutral pion is produced, it promptly decays into two photons, which, in the excellent approximation where photoproduction can be neglected, generate electromagnetic showers. These are made of electrons, positrons and photons and are in some sense neutral to the subsequent development of the shower where new mesons, among which neutral pions, are produced. The present section addresses the question of the longitudinal development of such electromagnetic showers, providing a parameterized description of the mean longitudinal shower profile and of its shower-to-shower fluctuations. In its present version, the transverse shower profile is not considered; its description should be the subject of further work.

The next section addresses the much more complex question of hadronic shower development. At variance with electromagnetic showers, where the underlying physics is the well understood QED, hadronic showers are made of a cascade of strong hadronic interactions. There, the underlying physics, QCD, is well understood in its principles but precise calculations are only feasible in the perturbative approximation of the theory, implying essentially large transverse momenta. Most mesons produced in a shower being low transverse momenta, perturbative QCD does not apply: one needs to rely on approximations inspired from the qualitative knowledge one has of its main features. In addition to this basic difficulty, weak meson decays compete with strong interactions in an altitude-dependent way, interaction lengths depending on the air density and decay lengths depending on energy, making a parameterization somewhat awkward.

Applications of the present treatment of electromagnetic showers to the LPM and Perkins effects are presented at the end of the section.

4.2. Longitudinal shower development

4.2.1 The method

We use a simple model of the longitudinal development of electron and photon showers, retaining only pair creation and bremsstrahlung as relevant elementary processes. At very high energies, showers contain so many particles that it is impracticable to follow each of them in a simulation. Most existing codes deal with this problem by using statistical approximations (sampling, averaging, thinning, etc.). The approach used here is different: as soon as a shower particle, electron or photon, has energy lower than some threshold, it is replaced by a parameterized subshower profile, considerably reducing the complexity of the problem. All what needs to be done is then to devise a proper parameterization of the shower profile and to calculate the dependence on energy of the parameters. In practice, the mean and *rms* values of the parameters are calculated once for all as a function of energy and the subshowers are generated accordingly with random Gaussian fluctuations of the parameters having the proper means and variances. A detailed account of this work is available in Reference 64.

4.2.2 Elementary processes

Showers may be initiated by an electron (or positron, here electron is to be understood as electron or positron) or a photon and any other particle that may be created in the cascade (such as $\mu^+\mu^-$ pairs from photon conversion) is ignored. Moreover the only processes considered are pair creation in the case of photons and bremsstrahlung in the case of electrons, implying that Compton scattering, photoelectric effect, and other processes that are important at lower energies are not taken into account.

To a very good approximation, the probability d^2P for a photon of energy E to convert in a medium of radiation length X_0 over a thickness $dx=X_0\,dt$ (t has no dimension, dx and X_0 are measured in g/cm^2), into a pair having an electron of energy in the interval $[\eta,\ \eta+d\eta]$ (the positron energy being in the interval $[E-\eta,\ E-\eta-d\eta]$) is

$$d^2P=\{1-4/3\ \eta/E\ (1-\eta/E)\}d\eta/E\ dt \qquad (4.1)$$

The radiation length in air is $36\ g/cm^2$.

The dependence of $Ed^2P/d\eta/dt$ on η/E is displayed in Figure 4.1 (left). It has a parabolic shape with a minimum of $2/3$ corresponding to the symmetric case (electron and positron having equal energies). It is symmetric in the exchange of the electron and positron (η/E becoming $1-\eta/E$). Integration over η/E gives $dP/dt=7/9$: the photon distribution over the thickness traversed, $x=tX_0$, is an exponential of the form $exp(-7/9t)$.

In the case of an incident electron of energy E, the probability d^2P to radiate, over a distance $dx=X_0dt$, a photon having an energy in the interval $[\eta, \eta+d\eta]$ is, to a good approximation,

$$d^2P= \{4/3- 4/3\ \eta/E + (\eta/E)^2\}\ d\eta/\eta\ dt \qquad (4.2)$$

It is illustrated in Figure 4.1 (right) where $d^2P/(dt\ d\eta/\eta)$ is shown against η/E. It reaches a minimum at $8/9$ for $\eta/E = 2/3$ while being unity when $\eta=E$ and being 4/3 when $\eta=0$. The total energy bremsstrahled per interval dt is

$$\int \eta\ d^2P = \{4/3\ E- 4/3\ E/2 + E/3\}\ dt = E\ dt. \qquad (4.3)$$

The remaining energy has therefore an exponential dependence over the thickness $x=tX_0$ traversed of the form e^{-t}. However, the number of photons bremsstrahled is infinite, an infinite number of zero energy photons being radiated. Introducing a cut-off ε, the number of radiated photons having energy in excess of ε is obtained by integration over η between ε and E:

$$dN=\{4/3 \ln E/\varepsilon - 5/6 + 4/3\ \varepsilon/E - 1/2\ (\varepsilon/E)^2\}dt \qquad (4.4)$$

The multiplication of particles in the cascade is counteracted by the energy losses which they suffer. The critical energy, E_c, is defined as the energy where an electron loses as much energy by ionization as it does by radiation. It is equal to 80 MeV in air. The strategy adopted here is to consider bremsstrahlung explicitly only for photons having an energy in excess of E_c, namely setting $\varepsilon=E_c$ in Relation 4.4. At $E=10^{21}$ eV with $\varepsilon=E_c=80$ MeV and $dx=0.01X_0$, Relation 4.4 gives $dN\sim\{20\ln10-\ln80-5/6\}0.01\sim 0.4$. Multiple photon radiation can therefore be safely neglected when using such small steps of 0.01 radiation lengths.

The energy radiated in the form of photons of energy lower than E_c is, in such a step:

$$dE=0.01\{4(E_c/E)/3-2(E_c/E)^2/3+(E_c/E)^3/3)\}E \qquad (4.5)$$

The electron energy loss is calculated in each slice $dx=0.01X_0$ as the sum of the latter and of the ionization loss:

$$dE/dx=0.01E_c(1+0.15\log_{10}[E/E_c])dt \qquad (4.6)$$

In addition any particle, electron or photon, having energy lower than 1.5 MeV is made to stop and to deposit its energy in the shower. Both this energy and the energy loss calculated using Relation 4.6 are deposited over two radiation lengths with a profile having a maximum at one radiation length.

The model has been checked against the result of a detailed simulation [64] for 30 GeV electrons in iron ($E_c= 20$ MeV). The result is displayed in Figure 4.2 and shows quite good agreement given the high energy approximation used here.

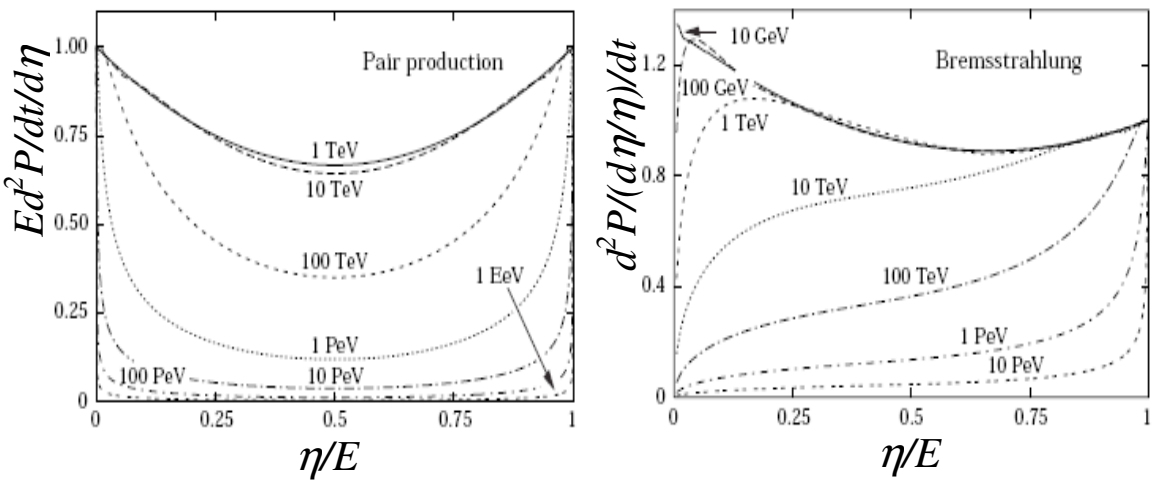

Figure 4.1: Left: Differential pair creation probability per unit of radiation length as a function of the fractional energy taken by the electron.
Right: Differential bremsstrahlung probability per unit of radiation length and per $d\eta/\eta$ as a function of the fractional energy taken away by the photon.
Full lines are without and dashed lines with LPM reduction (from 100 GeV to 10 PeV for bremsstrahlung and from 10 TeV to 1 EeV for pair creation in steps of a factor 10).

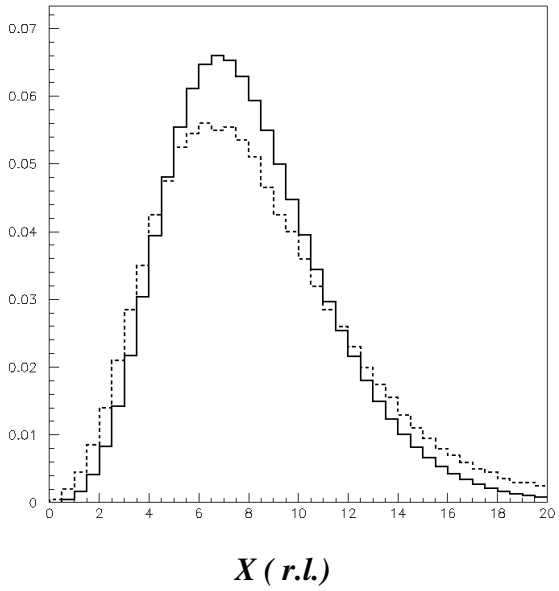

Figure 4.2: Average longitudinal profile (radiation length) of a shower induced by a 30 GeV electron in iron: full line, result of the present simulation; dotted line: EGS4 result [64].

4.2.3 Parameterization of the profile

The form used here to parameterize the longitudinal shower profile is the standard Gaisser-Hillas function [66]

$$lnS=lnS_{max}+\{[X_{max}-X^*]/w\}\{1+ln([X-X^*]/[X_{max}-X^*])\} \qquad (4.7)$$

where S is the longitudinal density of charged particles at depth X (measured in g/cm^2) in the medium. In practice, SdX may be the sum of the charged particle track lengths in the transverse shower slice between X and $X+dX$, or the energy ionization loss in that same slice, or even the amount of Cherenkov or fluorescence light produced in that same slice. At high energies, all four distributions are expected to have very similar shapes. The depth variable X is measured in g/cm^2 with dX being the product of the local density by the thickness of the slice. In atmospheric air the dependence of density on altitude distorts X with respect to actual distances.

The quantity X^* defines where the shower, understood as its charged particle components, starts developing. In the case of a photon, it starts at the location of the first pair creation while in the case of an electron it starts at $X^*=0$. Obviously, once started, the shower develops independently from X^* and S depends explicitly on $X–X^*$. It is therefore sufficient to consider showers induced by electrons, *i.e.* having $X^*=0$.

Taking S_{max} and X_{max} as units, one defines reduced variables $\eta=S/S_{max}$ and $\xi=X/X_{max}$. The reduced profile then reads $\eta=\{\xi exp(1–\xi)\}^{\delta}$ and depends on a single parameter $\delta=X_{max}/w$. Equivalently, $ln\eta=\delta(ln\xi+1–\xi)$.

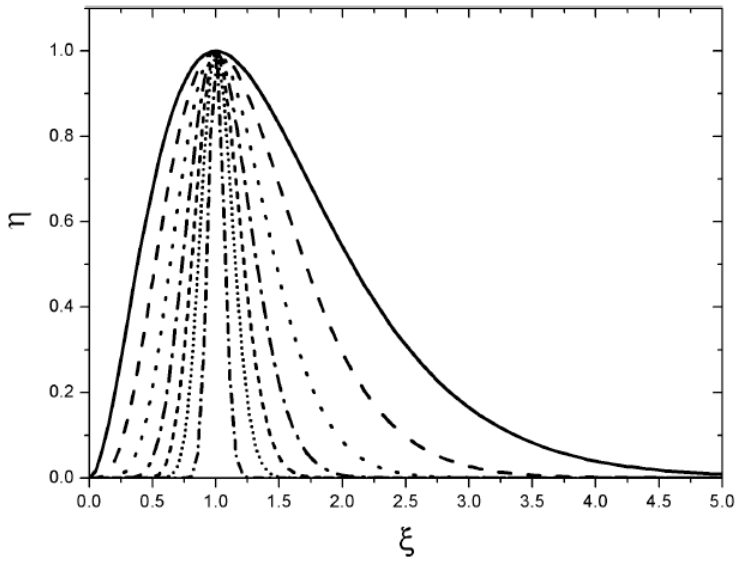

Figure 4.3: Reduced profiles for different values of δ (2, 4, 8, 16, 32, 64 and 256).

The reduced profile starts at 0 at origin as ξ^{δ} and approaches 0 again when $\xi\rightarrow\infty$. Differentiating gives $d\eta/d\xi=\eta\delta(1/\xi–1)$ which cancels for $\xi=1$ where η reaches its maximum value, 1, independently from δ. Therefore, the real profile reaches its maximum value S_{max} at $X=X_{max}$ which justifies their names. The second derivative, $d^2\eta/d\xi^2=\eta\delta^2(1/\xi–1)^2–\eta\delta/\xi^2$ cancels for $\delta(1/\xi–1)^2=1/\xi^2$ or $\xi=1\pm1/\sqrt{\delta}$. While the turning points are equidistant from $\xi=1$ the profile is not at all symmetric around this value. As illustrated in Figure 4.3 it is significantly skewed, the more the larger δ. As $\delta>1$, the profile starts tangent to the ξ axis. Analytic expressions of the mean, *rms* and integral values are given in Table 4.1 below, both for the reduced profile and the real one.

Table 4.1. Gaisser-Hillas parameters for an electron ($X^*=0$).

Parameter	Reduced profile	Real profile
Mean value	$1+1/\delta$	$X_0+X_{max}(1+w/X_{max})$
Rms value	$(\sqrt{(1+\delta)})/\delta$	$\sqrt{((w+X_{max})w)}$
Integral	$J(\delta) = e^{\delta}\Gamma(\delta+1)/\delta^{\delta+1}$	$S_{max}X_{max}J(X_{max}/W)$

The knowledge of $\langle X\rangle$ and of $Rms(X)$ fixes w and X_{max}. The knowledge of $\Sigma = \int SdX$ then fixes S_{max}. Explicitly,

$$\delta = \{\langle X\rangle / Rms(X)\}^2 - 1 \quad X_{max} = \langle X\rangle \delta/(\delta+1)$$
$$S_{max} = \Sigma\, \delta^{\delta+1} exp(-\delta)/\Gamma(\delta+1)/X_{max} \qquad w = X_{max}/\delta \tag{4.8}$$

It has been checked that $\langle X\rangle$ and $\rho=Rms(X)/\langle X\rangle$ are not significantly correlated, thereby making it legitimate to apply independent Gaussian fluctuations to each.

The dependence on energy of the mean and *rms* values of $\langle X\rangle$ and ρ evaluated by the present simulation is illustrated in Figure 4.4. The parameters were calculated with full shower development up to an initial energy of 100 GeV. Above this energy, any shower particle having an energy smaller than 40% of the initial energy was replaced by a Gaisser-Hillas profile evaluated for the proper values of the relevant parameters (after application of Gaussian fluctuations). The start of the profile was defined as $X^*=0$ for electrons and was chosen at random with an $exp(-[7/9]X^*/X_0)$ distribution for photons. As $E_c=80$ MeV is the only scale of the problem, the development of the profile scales in proportion with the logarithm of the energy as soon as E_c is negligible with respect to initial energy.

Because of shower-to-shower fluctuations, the parameters that describe the average profile (obtained as superposition of a large number of different showers) are not exactly the same as the mean values of the parameters that describe individual profiles (as displayed in Figure 4.4). More precisely, the mean value of the former profile, $\langle X'\rangle$, and that of the mean values of the latter profiles, $\langle\langle X\rangle\rangle$, are equal and can be parameterized as $3.22+2.34\log_{10}E$. But the ρ parameter of the former profile, ρ', and the mean value of the ρ parameters of the latter profile, $\langle\rho\rangle$, differ. They can be parameterized as

$\rho'=0.102+1.91/(\log_{10}E+4.246)$ and $\langle\rho\rangle=0.020+4.106/(\log_{10}E+9.449)$ respectively. In these parameterizations, units are radiation lengths and GeV. The difference between ρ' and ρ is further illustrated in Figure 4.5 which compares the corresponding values of $b=1/w=\rho^2/\langle X\rangle$. The asymptotic value of ~ 70 inverse radiation lengths is reached by b' significantly earlier than by b.

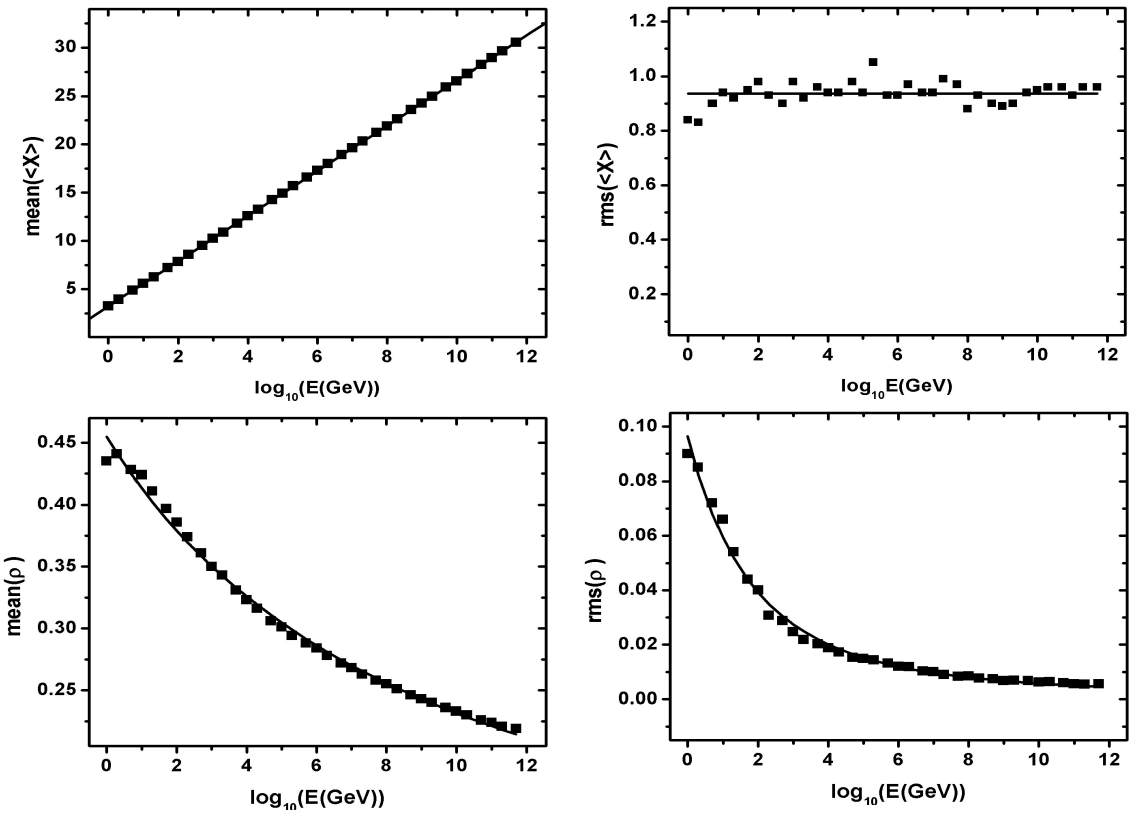

Figure 4.4: Dependence on energy of the parameters defining the longitudinal shower profile. Upper panels: Mean value of <*X*> (left) and *rms* value of <*X*> (right); units are radiation lengths. Lower panels: Mean value of *ρ* (left) and *rms* value of *ρ* (right). The lines are the result of the fits described in the text.

In the case of the latter profiles, the *rms* values of the quantities <*X*> and *ρ* define the size of the shower-to-shower fluctuations. To a very good approximation, *Rms(<X>)* is constant and equal to 0.94±0.01 radiation lengths. On the contrary, *Rms(ρ)* is found to decrease with energy as $Rms(\rho)=0.001+16.20/(\log_{10}E+5.6)^3$.

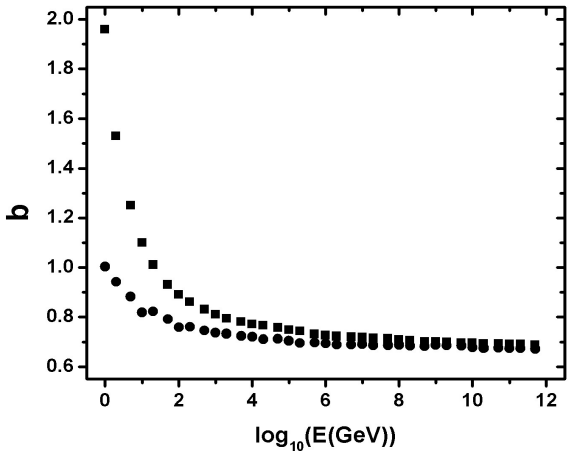

Figure 4.5: Dependence of $b=1/w=\rho^2/<X>$ on energy for the mean profile (full dots) and for individual profiles (full squares).

4.2.4 Neutral pion showers

Ultra high energy extensive air showers are essentially made of electromagnetic sub showers generated from the decay photons of π^0 secondaries. As these are scalar mesons, the decay photons are emitted isotropically in the π^0 rest frame. Namely the distribution of the cosine u of the angle of the centre-of-mass photon momentum with the laboratory π^0 momentum is uniform. Applying the proper Lorentz transformation and neglecting the π^0 mass in comparison with its energy, a π^0 of energy E produces two photons of energies $E^{\pm}=½E(1 \pm u)$. The energy dependence of the resulting showers is illustrated in Figure 4.6. Here X^*, being the smaller number of two numbers having an exponential distribution of scale $9X_0/7$ is observed to have an exponential distribution of scale $9X_0/14$ as expected (Figure 4.6).

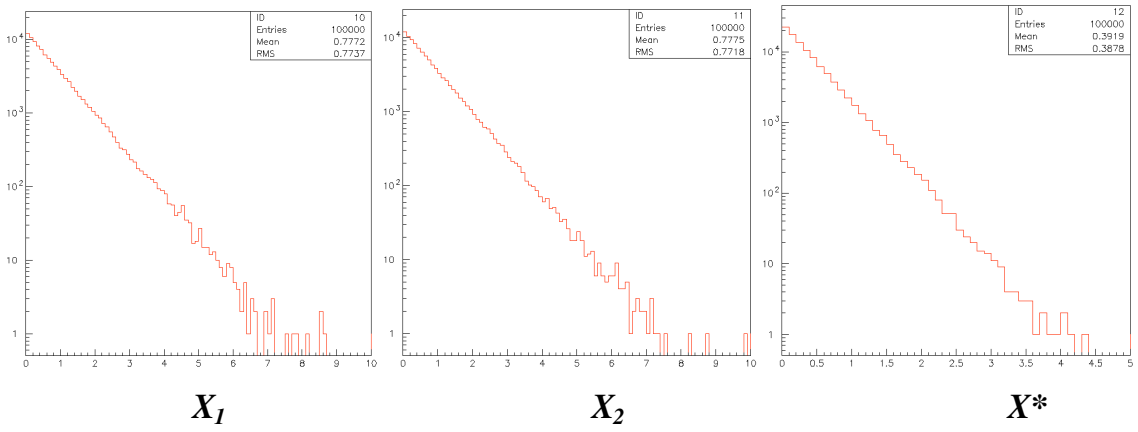

Figure 4.6: Distribution of X^* in the case of π^0 decays. The left panels (X_1 and X_2) are for the decay photons. The right panel (expanded scale) is for the smaller of X_1 and X_2.

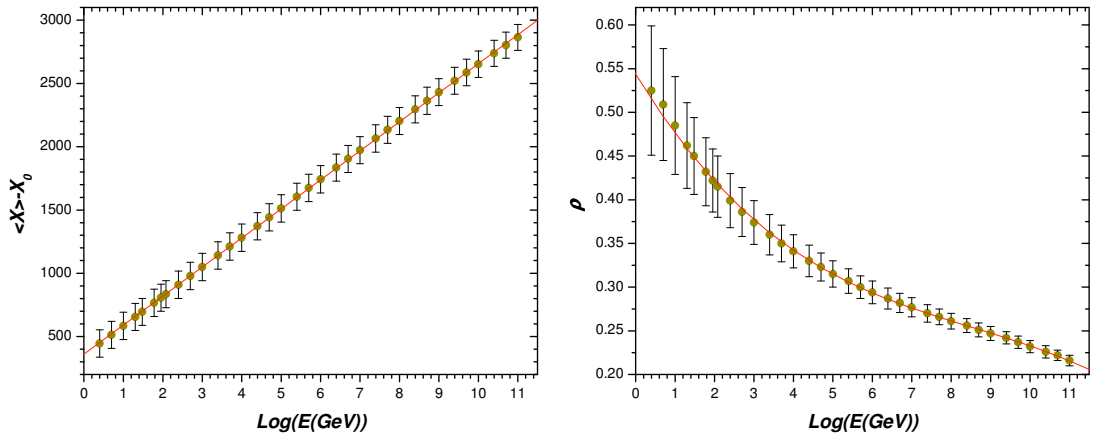

Figure 4.7: Dependence on the decimal logarithm of the energy of the mean values of $\langle X\rangle - X_0$ (left panel) and ρ (right panel) for neutral pions. The vertical bars are not error bars but correspond to ± the *rms* values of the distributions. Thicknesses are measured in percent of a radiation length.

Table 4.2. Parameterization of the simulated shower profiles at energies between 2.5 GeV and 10^{11} GeV.

		A	B	C	D
Electrons	*Mean* $<X>-X_0$	3.91	2.30	-	-
	Mean ρ *(%)*	51.5	–6.7	0.6	$-2.4\ 10^{-2}$
	Rms $<X>-X_0$	0.94	-	-	-
	Rms ρ *(%)*	6.77	–2.20	0.28	–0.01
Photons	*Mean* $<X>-X_0$	3.45	2.30	-	-
	Mean ρ *(%)*	55.2	–7.7	0.7	$-2.9\ 10^{-2}$
	Rms $<X>-X_0$	0.81	-	-	-
	Rms ρ *(%)*	6.90	–2.37	0.31	–0.01
π^0	*Mean* $<X>-X_0$	3.60	2.30	-	-
	Mean ρ *(%)*	54.4	–7.4	0.7	$-2.78\ 10^{-2}$
	Rms $<X>-X_0$	1.07	-	-	-
	Rms ρ *(%)*	7.92	–2.68	0.35	$-1.5\ 10^{-2}$

Fits of the energy dependence of the mean and *rms* values of the distribution of $<X>-X_0$ and ρ have again been performed over the whole energy range (2.5 GeV to 10^{11} GeV). They are illustrated in Figure 4.7 and their parameters are listed in Table 4.2. Below 2.5 GeV, it is no longer justified to neglect the transverse momenta of the decay photons, Whether or not the fits can be used at these low energies depends on what one is after. In a high energy hadronic shower simulation, the detailed treatment of these low energy pions is not important as long as energy is conserved, which is the case in the approximation made above, $E^{\pm}=\frac{1}{2}E(1 \pm u)$.

4.3 The LPM effect

4.3.1 Description of the effect

As an application of the results obtained above, we now considered the effect of LPM suppression on extensive air showers [67]. The unusual kinematics conditions of bremsstrahlung and pair creation are at the source of the Landau Pomeranchuk Migdal (LPM) effect [68]. In the case of bremsstrahlung by a relativistic electron, the momentum transfer, and particularly its longitudinal component, is very small. Letting E be the incident electron energy and m the electron mass, the longitudinal momentum transfer is (to first order in $\varepsilon=m/E<<1$ and neglecting transverse momenta)

$$
\begin{aligned}
q_L = p_e - p'_e - k &= \sqrt{(E^2 - m^2)} - \sqrt{\{(E-k)^2 - m^2\}} - k \\
&= E(1 - \tfrac{1}{2}\varepsilon^2) - (E-k)[1 - \tfrac{1}{2}\varepsilon^2 E^2/(E-k)^2] - k \\
&= \tfrac{1}{2}\varepsilon^2[-E + E^2/(E-k)] \\
&= \tfrac{1}{2}\varepsilon^2 Ek/(E-k) \\
&= m^2 k/[2E(E-k)]
\end{aligned}
\qquad (4.9)
$$

where p_e and p'_e are the electron longitudinal momenta before and after radiation took place and k is the longitudinal momentum of the radiated photon.

The Heisenberg uncertainty principle implies that the formation of the final state occurs over a distance $l_{f0} = \hbar/q_L = 2\hbar E(E-k)/(m^2 k)$, called the formation length, that may be very large. As an example, a 10^{18} eV electron radiating a 10^{15} eV photon gives $q_L = 10^{-10}$ eV and $l_{f0} = 2$ *km*. Over the formation length, the system cannot be significantly disturbed for the final state to materialize. Any significant perturbation will strongly reduce the bremsstrahlung cross-section. In particular, multiple Coulomb scattering will produce such a perturbation as soon as the multiple scattering angle [64], integrated over the formation length, exceeds the characteristic bremsstrahlung emission angle ε. This occurs over a distance l_{ms} that is easily calculated. To a good approximation, the reduction factor S is simply

$S = l_f / l_{f0} = \sqrt{\{kE_{LPM}/[E(E-k)]\}}$ where

$E_{LPM} = m^4 X_0 / (2\hbar E^2) \approx 3.85$ TeV/cm X_0 (*2.2* TeV for lead and 1.17 10^{17} eV for air at sea level). To this approximation, S is a universal function of the scaling variables k/E_{LPM} and E/E_{LPM} .

While the standard bremsstrahlung cross-section is of the form $dN/dk \sim 1/k$ the LPM reduced cross-section is instead $\sim 1/\sqrt{k}$.

A similar effect takes place in the case of pair creation.

4.3.2 Migdal evaluation and experimental evidence

Migdal [68] has performed a more serious evaluation of the suppression factors and his results are displayed in Figure 4.1 in the case of lead. When the electron energy reaches 100 GeV or so, bremsstrahlung starts to be significantly reduced, in particular the radiation of lower energy photons. The same happens in the case of pair creation when the photon energy reaches 1 TeV or so, symmetric pairs being preferentially suppressed. Integrating the curves displayed in Figure 4.1 gives the global reduction factor. Its dependence on energy is shown in Figure 4.8 for both electrons (bremsstrahlung) and photons (pair creation).

The LPM effect has been studied at SLAC using electrons of 8 to 25 GeV incident on thin targets (0.001 to 0.06 X_0) made of various materials (from carbon to gold) [69]. The beam was pulsed, with, on average, one electron per pulse, and bent in a magnetic dipole by 39 mrad after having crossed the target. Both the radiated photon and the outgoing electron were detected in high resolution arrays (BGO for the photon, with a 4% energy resolution, and lead glass for the electron). Beam lines were evacuated. High quality data were collected and the 25 GeV gold data (0.06 and 0.07 X_0) show a strong LPM reduction (up to a factor 3 for photon energies of 5 MeV) well described by the Migdal model. Well understood edge effects cause

differences between thin and thick target data. These data give confidence in the Migdal calculation and justify the approximations made.

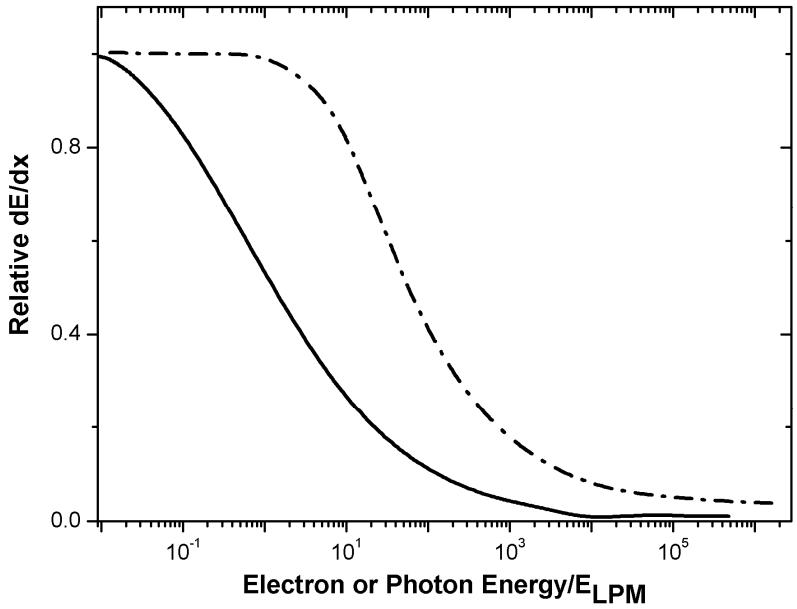

Figure 4.8: Energy dependence of the LPM reduction factors in Pb for bremsstrahlung (full line) and pair creation (dashed line).

4.3.3 Evaluation of the effect on extensive air showers

In the case of extensive air showers, the situation is not as simple as in the case of solid targets: the density of atmosphere, and therefore the value of E_{LPM} depend on altitude. In the present context it is sufficient to model the atmospheric pressure in the form of an exponential decreasing over a characteristic length of 8.7 km. The value [70] taken by E_{LPM} is 1.17 10^{17} eV (A_0/A), where A is the thickness of air above the altitude under consideration and A_0 its value at sea level, 1030 g/cm^2. E_{LPM} is therefore 3.4 EeV for 36 g/cm^2 (1 X_0), and 1.3 EeV for ~90 g/cm^2 (one hadronic interaction length). Temperature effects may slightly affect these values but are ignored here. The first hadronic interaction produces several hundred pions with neutral pions decaying exponentially into a photon pair over a decay length of ~200 m/EeV. The highest energy neutral pions can reach 20 or so EeV but they represent a small fraction, a few percent at most, of the secondary pions. This dilution of the incident energy among many pions considerably reduces the impact of the LPM effect.

The changes induced by the LPM effect on the integrated (Figure 4.8) and differential (Figure 4.1) bremsstrahlung and pair creation cross-sections have been implemented in the simulation code. Calling F_e and F_γ the reduction factors displayed in Figure 4.8, calculated for lead with E_{LPM}=*2.2* TeV, their values for air at altitude z *(km)* are

$F\{E \times E_{LPM}(lead)/E_{LPM}(air)\}$. As

$E_{LPM}(air)=1.17\ 10^{17}$ eV (A_0/A) and $A=A_0 exp(-z/8.7)$,

$E_{LPM}(air)=1.17.10^{17}$ eV $exp(z/8.7)$: the reduction factors are

$F\{E\times(2.2/1.17)\times10^{-5}\times exp(-z/8.7)\}$. At the nth 0.01 X_0 step, using $A_0=1030$ g/cm^2 and $X_0=36$ g/cm^2, one reaches an altitude z such that

$1030\ exp(-z/8.7)= n\ cos\theta\ 36/100$ where θ is the shower zenith angle. Then

$F\{E\times(2.2/1.17)\times10^{-5}\times exp(-z/8.7)\}=F\{6.6Encos\theta\ 10^{-9}\}$.

The LPM reduction in the upper atmosphere is therefore of the same order of magnitude as in lead at an energy a million times lower. The reduction occurs on bremsstrahlung at lower energy − typically one order of magnitude lower − than in pair creation. Results are presented in Figure 4.9 as a function of energy for incident electrons and for three angles of incidence: vertical, 30^o and 60^o.

The main effect on the differential bremsstrahlung cross-section is to suppress preferentially the radiation of low energy photons, namely to favour bremsstrahlung of high energy photons. This increases the efficiency of the cascade mechanism in the development of the shower, which tends to make it shorter and counteracts somewhat the effect of the reduction of the total cross-section which tends to make it longer. Indeed, $<<X>>$ is even found to decrease slightly with respect to the no LPM case before taking off significantly around 10^{21} eV but this small decrease is not significant within the accuracy of the model calculation. The increase in $<\rho>$, larger than that in $<<X>>$, starts being significant above 10^{20} eV. Large zenith angle showers develop longer in the low density upper atmosphere and are therefore less affected by the LPM suppression.

The average effect on extensive air showers is therefore negligible in practical cases. However, shower-to-shower fluctuations are found to be strongly influenced by the LPM effect. They are amplified by large factors reaching, at 5.10^{20} eV, 6.4, 5.0 and 2.7 for vertical, 30^o and 60^o showers respectively. The LPM effect may therefore need to be taken into account when shower-to-shower fluctuations are of particular relevance.

In practical cases, results will depend upon the altitude of the observatory as showers ending into ground are only partially measured. In the present simulation, this effect has been ignored: the altitude of the observatory was supposed to be low enough to allow the shower to fully develop in atmosphere.

The results displayed in Figure 4.9 apply to showers induced by electrons or photons. They would be of direct relevance to γ-ray astronomy if energies in excess of ~10 EeV could be reached. The Pierre Auger Observatory has been searching for such showers and has been able to place strong limits [71] on their occurrence that essentially reject most top-down models of UHECR production.

Extensive air showers can reach such energies but the impact of the LPM effect on their development is considerably reduced by two factors. One, mentioned earlier, is the high multiplicity of the first hadronic interaction, which dilutes considerably the available energy among the secondary mesons produced. The second results from the fluctuations associated with the large decay length of neutral pions. The distribution of their decay vertices being exponential, the resulting shower-to-shower fluctuations have an *rms* value equal to the characteristic decay length, much larger than that induced by the LPM effect. In the

typical case of a vertical shower produced by a first hadronic interaction at an altitude of 20 km, one hadronic interaction length, 90 gcm^{-2}, corresponds to 1.1 km, which in turn is the characteristic decay length of a neutral pion of ~6 EeV. At such energy, the LPM effect starts barely to take off while the fluctuations associated with the neutral pion decay are already at a scale commensurate with the difference expected between showers induced by protons and respectively iron nuclei.

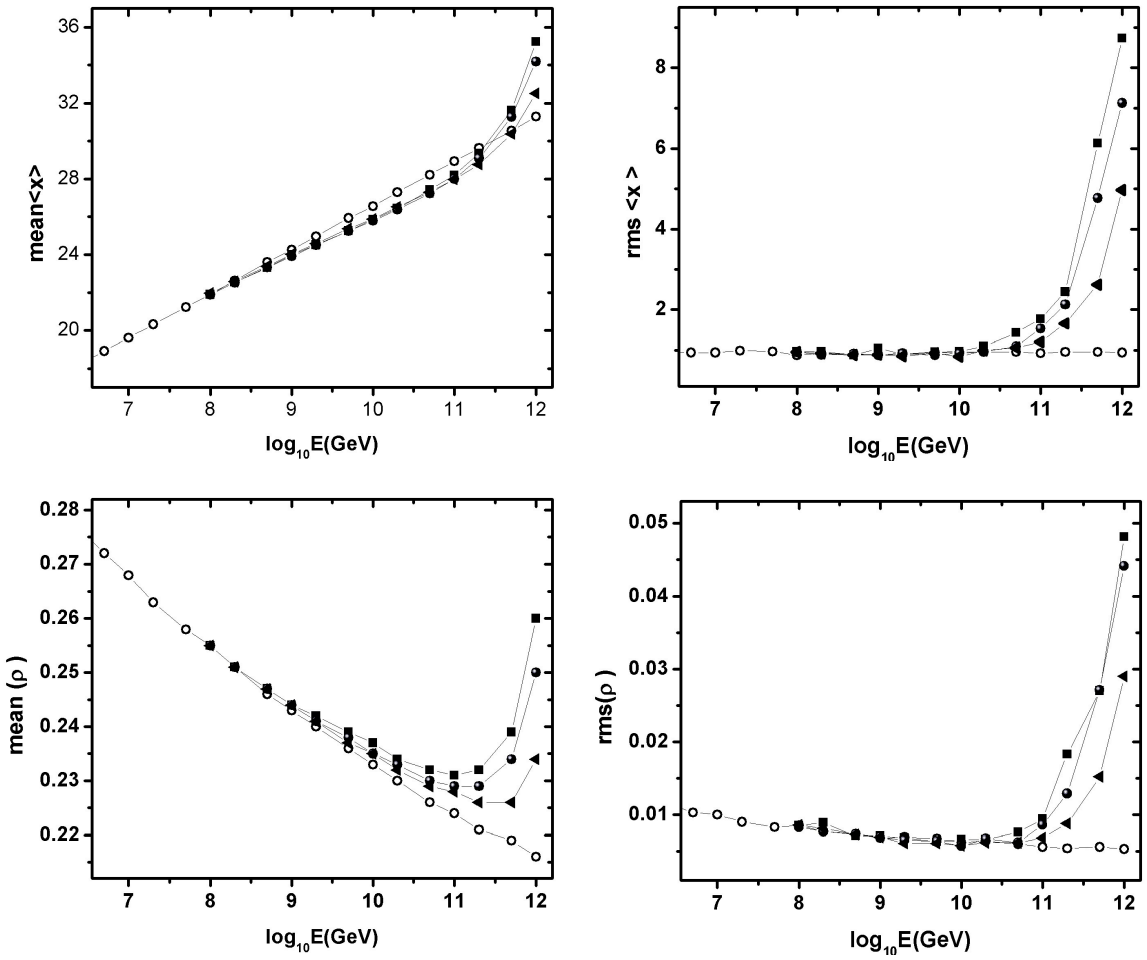

Figure 4.9: Dependence on energy of the shower parameters calculated (LPM effect included) for incident electrons and for three angles of incidence: vertical (full circles), *30*^{o} (full squares) and *60*^{o} (full triangles). Mean values are shown in the left panels and *rms* values in the right panels; <<*X*>> is shown in the upper panels and *ρ* in the lower panels. The results obtained when ignoring the LPM effect are shown as open circles.

In conclusion, the incidence of the LPM effect on the physics of extensive air showers is very small and can be neglected in most practical cases. The parameterization of the longitudinal profile of electromagnetic showers presented here should prove useful when dealing with problems such as the LPM effect presented here as an illustration.

4.4 The Perkins effect

4.4.1 Introduction

As a second application of our treatment of electromagnetic showers, we now consider [72] the Perkins effect. Physicists working with photographic emulsions have noted [73] and studied [74] the reduced ionization occurring in the event of a conversion of a high energy photon. The effect is well described as resulting from the mutual cancellation of the electric fields carried by the electron and positron of the newly formed pair. In practice reduction occurs whenever the transverse separation between electron and positron does not exceed 10 nm and is stronger for smaller separations. Recently, M. Urban [75] suggested studying the consequences of the effect on the early development of UHECR showers. The present section addresses this question.

4.4.2 Reduced ionization

A photon of energy E converts into an electron of energy $E_1=uE$ and a positron of energy $E_2=(1–u)E$ where u has a well known distribution. Their initial angular separation is negligible ($\sim m_e/E$) and their acquired separation is essentially the result of multiple Coulomb scattering in the medium where the photon has converted. After x radiation lengths their space angles with respect to the photon momentum are $\alpha_i=21\sqrt{x}/E_i$ where E_i is measured in MeV. After n steps of a percent of a radiation length, which is the step size used in the Monte Carlo code, the angle between electron and positron is therefore

$\omega=\sqrt{(\alpha_1^2+\alpha_2^2)}=21\sqrt{\{x(1/E_1^2+1/E_2^2)\}}=2.1\sqrt{\{n(1/u^2+1/(1–u)^2)\}}/E$

$= s\sqrt{n}$ where $s=2.1\sqrt{\{(1/u^2+1/(1–u)^2)\}}/E>2.1\sqrt{8}/E=5.9/E$.

The transverse separation[1] between electron and positron after a path length L is of the order of $L\omega$. Taking the atmospheric pressure ρ at altitude z of the form

$\rho=1030\exp(–z/8.7)$ with ρ in g cm^{-2} and z in km,

$L=\Delta z/\cos\theta=8.7\ln(\rho_{down}/\rho_{up})/\cos\theta=8.7\ln(1+\Delta n/n_{up})/\cos\theta$

where Δz is the drop in altitude, Δn the number of steps crossed since the photon converted and θ the zenith angle associated with the path L.

For the effect to be significant, it must extend over at least one step, namely $L\omega=8.7s\ln(1+1/n_{up})/\cos\theta$ must not exceed 10 nm, therefore $52\ln(1+1/n_{up})/E/\cos\theta$ must not exceed 10^{-11} km. Namely E must exceed $E_{low}=5.2\ \ln(1+1/n_{up})/\cos\theta$ EeV. If it does the effect will be active over Δn_{max} steps such that $10^{-11}\cos\theta=8.7s\sqrt{\Delta n_{max}}\ln(1+\Delta n_{max}/n_{up})$. This equation is easily solved by iteration. For $n_{up}>>1$, it reads

$10^{-11}\cos\theta=8.7s\Delta n_{max}^{3/2}/n_{up}$, hence $\Delta n_{max}=\{10^{-11}\cos\theta n_{up}/(0.87s)\}^{2/3}$.

As a function of the number Δn of steps following the photon conversion, the separation increases from zero to 10 nm when Δn increases from zero to Δn_{max} in

[1] Note that the longitudinal separation, $L(1/\beta_1-1/\beta_2)$, is much smaller than the transverse separation unless one of the energies is very small, of order of MeV. Its effect can safely be neglected. Moreover, the transverse separation is in fact $L\omega/\sqrt{3}$: the calculation performed in the remaining of this section is therefore overestimating the size of the effect.

approximate proportion to $\Delta n^{3/2}$. Hence the corresponding ionization is $(\Delta n/\Delta n_{max})^{3/2} I_0$, I_0 being the ionization in the absence of reduction. In order to account for possible deviations from the simple model described above a form $(\Delta n/\Delta n_{max})^{\alpha} I_0$ is retained where α will be varied between 1 and 2.

The Monte Carlo code has been modified accordingly. It starts with a photon of energy E converting after n_{up} steps and flying downward with zenith angle θ. The threshold used to stop the development of the cascade is evaluated for each secondary particle as the associated value of E_{low} and, above threshold, the value of Δn_{max} is calculated for each photon conversion. Ionization is then simply reduced by the factor $(\Delta n/\Delta n_{max})^{\alpha}$.

4.4.3 Results

Figure 4.10 displays the early development of vertical showers induced by photons having energies of 1, 10 and 100 EeV respectively. The photon is made to convert after having traversed 1 radiation length and α is equal to 1. The effect takes off above 1 EeV and then grows with energy. The profiles displayed in Figure 4.10 have not been normalized to a fixed area: their amplitude increases with energy, nearly linearly as the longitudinal extension increases only logarithmically with energy. This causes the effect on the early shower development to increase much less fast than might have been expected: at higher energies, bremsstrahlung is soon catching up. The delay does not exceed 0.2 radiation length.

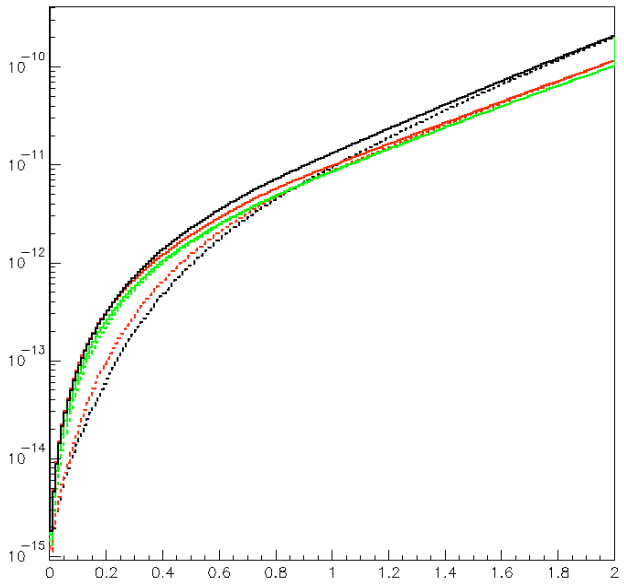

Figure 4.10: Early development of shower profiles (arbitrary units) induced by a vertical photon converting at a depth of one radiation length taken as origin of abscissa (scale in units of one radiation length). The solid (dotted) curves are without (with) reduced ionization. Energies are 1 EeV (green), 10 EeV (red) and 100 EeV (black).

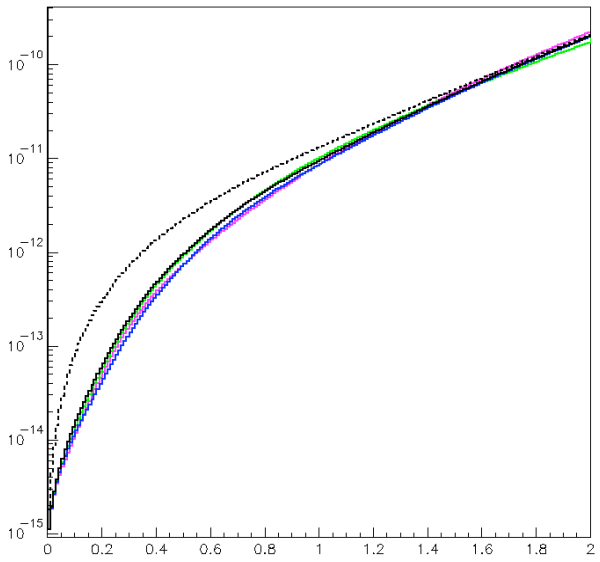

Figure 4.11: Effect on the early development of a 100 EeV photon shower profile (arbitrary units, black) such as shown in Figure 4.10 of: converting at a depth of 5 radiation lengths (violet), using *α=2* (blue), increasing the zenith angle to 60^o (green). The dotted curve ignores the effect.

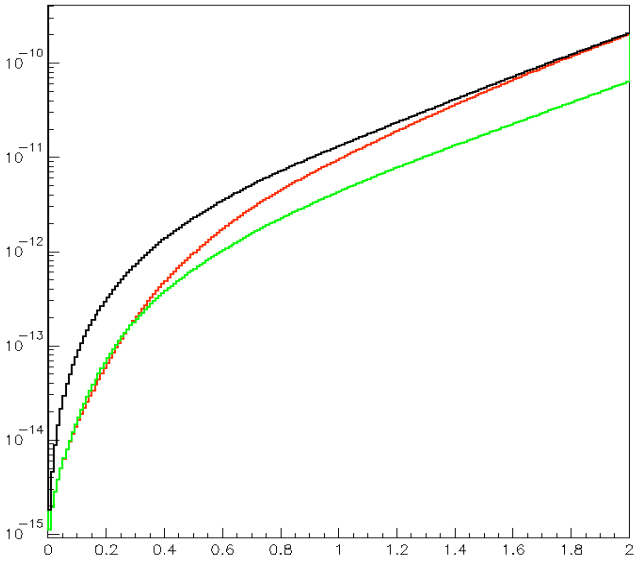

Figure 4.12: Effect on the early development of a 100 EeV photon shower profile (arbitrary units, red) such as shown in Figure 10 of reducing bremsstrahlung in proportion with the reduced ionization (green). The black curve ignores both effects (ionization and bremsstrahlung).

Figure 4.11 displays the effect of increasing the depth at which the photon converts from 1 to 5 radiation lengths, the effect of increasing the zenith angle from 0 to 60^o and the effect of increasing α from 1 to 2. None of these is significant.

Finally, Figure 4.12 illustrates the contribution of bremsstrahlung over the distance where the ionization is reduced. There is no reason to expect a strong suppression in this case but some screening of the nuclear Coulomb field by the

partner electron or positron may occur. What is assumed in the figure is that bremsstrahlung is suppressed to the same level as ionization is, it being understood that this should be an overestimate. Then, the delay accumulated by the reduced ionization is not caught up and remains as a global shift of the shower profile to higher depths.

In summary, the delay induced by reduced ionization on the development of a photon induced air showers does not exceed 0.2 radiation length. In the practical case of hadron induced air showers, where photons are decay products of neutral pions, themselve being products of the first hadronic interaction, the effect is so diluted that it will become insignificant. It has been made visible here by comparing photons that all convert at the same place but in real life the conversion point fluctuates at the scale of a radiation length, not to mention the fluctuation of the π^o decay point which fluctuates at the scale of 200 m/EeV. Yet, the delay is systematic, at least on average. Shower by shower, it depends on the value taken by u, being maximal when $u=1/2$ and cancelling when u approaches 0 or 1.

4.5 Summary

The scaling property of the development of electromagnetic showers has made it possible to describe it in remarkably simple terms. The price to pay, ignoring particles other than electrons, positrons and photons and ignoring interactions other than bremstrahlung and pair creation, is modest: the model gives a very good approximation of reality and is considerably simpler than the much more sophisticated codes in common use in standard shower Monte Carlo packages.

The model developed in the present chapter has been applied to two simple processes, the LPM effect and the Perkins effect, illustrating its descriptive power. Both effects have been found nearly negligible in the energy domain accessible to the PAO.

The use of a Gaisser Hillas profile to describe the longitudinal shower development has been found to be a convenient tool when both the mean and *rms* values of the parameters are taken in due considerations. Individual shower profiles occurring naturally may substantially differ from Gaisser Hillas profiles but, on average, their properties are well described as long as the Gaisser Hillas parameters are properly fluctuated. Indeed, in the analysis of FD data, the use of Gaisser Hillas profiles to describe individual showers is known to be efficient and reliable. The parameterization of π^0 induced showers that was obtained in the present chapter will prove extremely useful in the next chapter when dealing with the electromagnetic component of hadronic showers. Unfortunately, the hadronic component does not obey a simple scaling law: two scales, interaction and decay, are competing. As a result, the case of hadronic showers, which is the subject of the next chapter, is much more difficult to handle.

Chapter 5

SIMULATION OF HADRONIC SHOWERS

Recent Auger results [52] have shown that existing Monte Carlo codes do not properly describe the muon component of UHECR showers. Such codes are very detailed and essentially include all of our knowledge in matter of hadronic interactions at ultra high energies. However, the price to pay is a lack of transparency that makes it difficult to use these in order to get some feeling of the influence of such or such a physics parameter of relevance. The present code has been written to overcome this weakness. Moreover, it focuses on muons that reach ground at a distance from the shower axis exceeding some predefined threshold, as done in practice in the analysis of actual Auger SD data. Indeed, the longitudinal shower profile, that is accessible to FD data exclusively, is studied without paying attention to its transverse extension.

The present chapter describes the main steps of the simulation.

A phenomenological approach, similar to the HDPM code [76] available in Corsika [19], is used with, however, a different strategy. The main problem in extrapolating accelerator data to UHECR showers is not so much energy than rapidity. Indeed 20 EeV in the lab correspond to 200 TeV in the cms, only two orders of magnitude above Tevatron energies and only one above LHC energies. The slow *logs* evolution of hadronic physics makes it unlikely that an extrapolation of lower energy collider data to the UHECR range be very wrong. But in terms of rapidity, UHECR showers are dominated by forward production, a region of rapidity that is inaccessible to collider data. In particular, no accurate measurement exists of the inelasticities and of the shape of the fall of the rapidity plateau, both of which are of utmost relevance to the development of UHECR showers. The HDPM approach is therefore to start from what is known, i.e. central production, and hope to get the forward production, which is essentially unknown, right. While being a very sensible approach, it does not allow for acting directly in a simple way on parameters such as the inelasticity. Here, instead, the inelasticity is taken as an adjustable parameter and the shape of the rapidity plateau is accessible in a transparent way.

Particular attention is devoted to features that allow for an identification of the primary, proton or heavier nucleus. This concerns essentially the first interaction: once the primary nucleus has interacted, shower development involves only nucleon-air and meson-air interactions. Any approximation made in the description of these interactions can be expected to affect similarly showers initiated by different primaries and not to significantly affect the comparison of, say, proton-initiated and iron-initiated showers. This remark allows for important simplifications in the treatment of the shower development following the first interaction.

5.1 Hadronic interactions

5.1.1 General strategy

The general picture is that which emerges from collider measurements such as that of the UA5 experiment [77]: two leading particles, each taking some 25% of the available cms energy, separated from a central rapidity plateau by two rapidity gaps. The rapidity plateau is characterized by a rather uniform density distribution and important short range rapidity correlations that are well described by clusters. These are seen in charge as well as in rapidity and transverse momentum. Transverse momentum distributions are steeply falling, first exponentially as expected from the Fourier transform of a disk, and later as a power law as expected from interacting point like constituents. The general algorithm used in the code is as follows:

1. Choose the fractions η_1 and η_2 of the cms energy $\sqrt{s}$ carried by the leading particles (which retain the identities of the projectile and target particle respectively). The cms energy available for central production is therefore $\sqrt{s}^*=(1-\eta_1-\eta_2)\sqrt{s}$. The leading particles do not carry any transverse momentum, and so do therefore the central secondaries taken together, the longitudinal cms momentum and energy of which are now defined.

2. Depending on $\sqrt{s}^*$, choose the number of central clusters and the numbers of pions in each cluster in such a way as to reproduce the desired multiplicity distribution. Once this is done choose the width of the rapidity plateau in such a way as to conserve energy. Clusters are then distributed evenly at equal intervals on the plateau. A final adjustment of the cluster momenta is made to fine tune energy momentum conservation.

A library of clusters containing between two and seven pions is created. Their transverse momentum distribution is chosen to reproduce that desired for the central pions and clusters are given no transverse momentum. While the width of the rapidity plateau and the cluster rapidity density increase linearly with $\log s^*$, implying that the cluster multiplicity increases quadratically with $\log s^*$, the number of pions per cluster and the transverse momentum distribution are nearly constant, increasing only slightly with $\log s^*$.

5.1.2 Central clusters

For a given number k of pions, central clusters are built by choosing the pion transverse momenta at random with a distribution of the form [19] $dN/dp_t \approx (p_t/p_0)(1/[1+p_t/p_0])^n$. The mean transverse momentum is $\langle p_t \rangle = 2p_0/(n-3)$. Typically, $p_0=1.3$ GeV and $n\sim10$. Therefore, we fix $n = 10$ and use p_0 to scale the transverse momentum distribution as desired. The default value uses $p_0\,(GeV)=3.5\langle p_t \rangle$ where

$$\langle p_t \rangle = \begin{cases} 0.3+0.00627\,\ln(4s^*) & \text{for } 2\sqrt{s}^* < 132 \text{ GeV} \\ \{0.442+0.0163\,\ln(4s^*)\}^2 & \text{for } 2\sqrt{s}^* \geq 132 \text{ GeV} \end{cases}$$

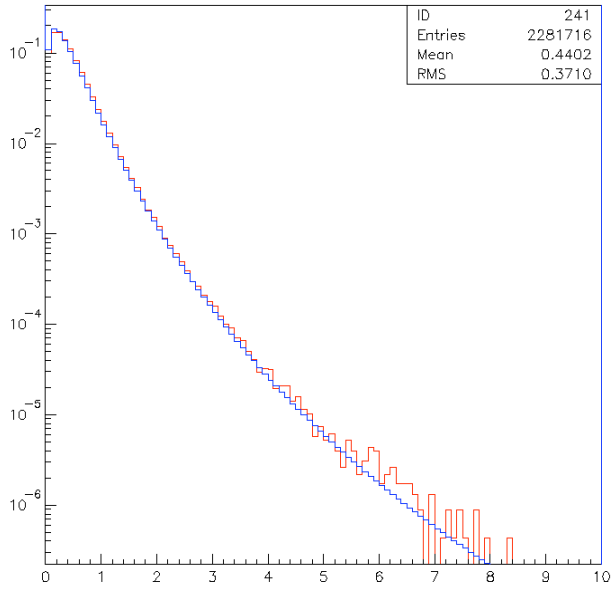

Figure 5.1: Transverse momentum distribution (GeV). The result of the code (red) is compared to the analytical form (blue) given in the text.

Figure 5.1 displays the transverse momentum distribution for $\langle p_t \rangle = 0.44$ GeV. The blue curve is of the form $dN/dp_t \approx (p_t/p_0)(1/[1+p_t/p_0])^{10}$ where $p_0 = 3.5 \langle p_t \rangle = 1.54$ GeV. The red histogram is the result of the algorithm used in the code.

The case of clusters containing only two pions is particularly simple: the momenta are chosen back to back with an isotropic distribution. The case of clusters containing at least three pions is dealt with as described below.

The azimuthal angles of the pion momenta are chosen at random between $-\pi$ and $+\pi$ and are adjusted in order for the total transverse vector momentum to cancel. The adjustment is made by changing each azimuth φ_i by a quantity $\Delta\varphi_i = (A\cos\varphi_i + B\sin\varphi_i)/p_{ti}$ where A and B are the result of a best fit. The operation is repeated 3 times. In some cases, it is not possible to cancel the total transverse momentum by simply changing the azimuthal angles. In such cases (defined as having a total transverse momentum in excess of 1 MeV) a new choice of transverse momenta is made.

Pion longitudinal momenta, p_l, are calculated in the rest frame of the cluster. Choosing θ, the angle of the pion momentum with the incident momentum, at random with a uniform $\cos\theta$ distribution one calculates $p_l = p_t/\tan\theta$ and boosts the whole cluster longitudinally in order to bring it to rest. The boost leaves the transverse momenta unchanged and does not too much disturb the isotropy of the cluster fragmentation as can be seen from Figure 5.2. It displays the final $\cos\theta$ distribution which is seen to be nearly uniform.

Figure 5.3 shows the cluster mass distributions for clusters containing $n = 3$ to 7 pions separately. The value of $\langle p_t \rangle$ was taken to be 0.4 GeV. To a very good approximation the mean values $\langle M \rangle$ depend linearly on multiplicity n: $\langle M \rangle = 0.58n - 0.25$.

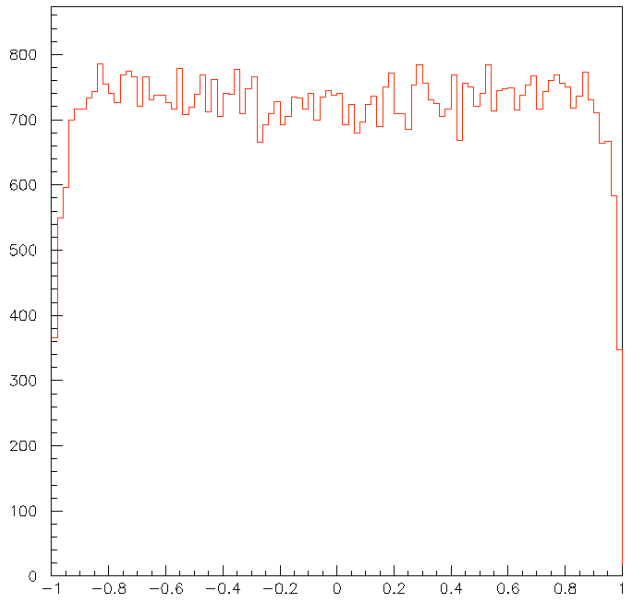

Figure 5.2: *Cosθ* distribution in the cluster rest frame for clusters containing at least three pions.

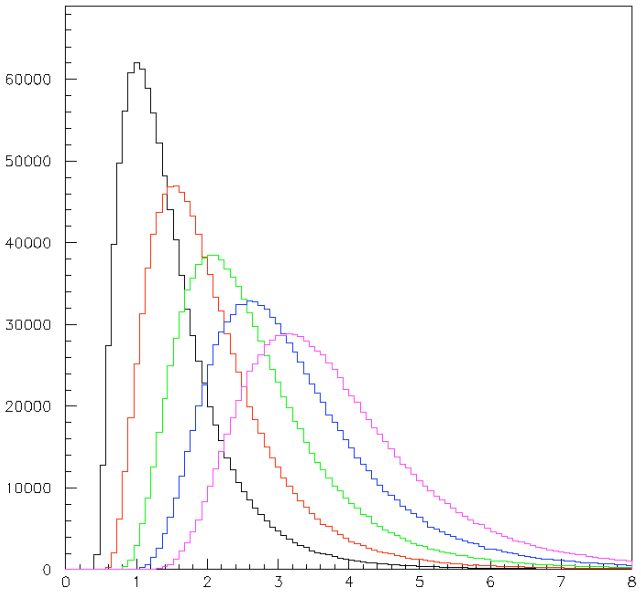

Figure 5.3: Cluster mass distributions for clusters containing 3, 4, 5, 6 and 7 pions (from black to purple).

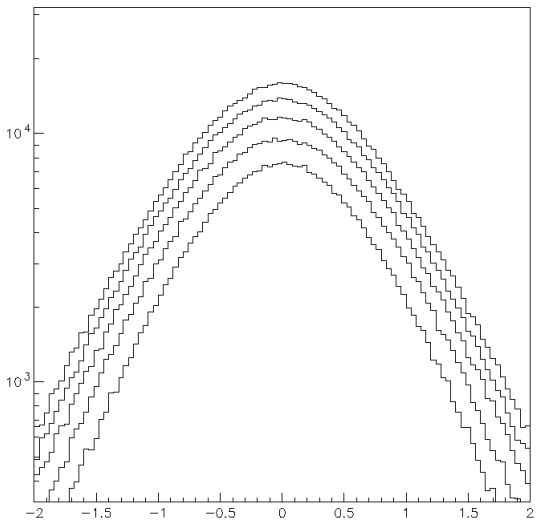

Figure 5.4: Distribution of pion rapidities in the cluster rest frame for clusters containing 3, 4, 5, 6 and 7 pions (moving upwards).

Figure 5.4 displays the distributions of pion rapidities for each multiplicity separately in the cluster centre of mass system. They are nearly Gaussians with an *rms* deviation of ~$1/\sqrt{2}$ units of rapidity, independently from multiplicity.

5.1.3 Nucleon-nucleon interactions

The calculations are made in the centre of mass system of the interacting nucleons having incident energies E_{inc1} and E_{inc2}. The energies carried away by the leading particles are written $\eta_1 E_{inc1}$ and $\eta_2 E_{inc2}$ where η_1 and η_2 are chosen at random with Gaussian distributions having a mean value of 0.6 and an *rms* value of 0.15. The Gaussians are truncated in order for the leading particle energies to exceed the particle rest mass but not to exceed the initial particle energy. The total energy available for central production is $\sqrt{s}^* = \sqrt{s} - \eta_1 E_{inc1} - \eta_2 E_{inc2}$. An effective energy $\sqrt{s_{eff}}$ is defined as $\sqrt{s_{eff}} = \sqrt{s}^*/(1 - \langle\eta_1\rangle/2 - \langle\eta_2\rangle/2)$. As already mentioned it makes more sense to use $\sqrt{s}^*$ rather than $\sqrt{s}$ to decide on the properties of central production; it is therefore necessary to define $\sqrt{s_{eff}}$ in order to use the formulae given in References 76 and 19 as a function of $\sqrt{s}$. The pion transverse momentum distribution is taken from Reference 76 as are the mean values of the total and charged multiplicity distributions. The number of pions per cluster is chosen at random between 2 and 7 with a Gaussian distribution having a mean value of $1.6 + 0.21\ ln s^*$ and an *rms* value of 1. The total number of clusters n_{cl} is chosen at random with an *ad hoc* distribution meant to properly reproduce the final multiplicity distribution. Its mean value, $\langle n_{cl}\rangle$, is taken to be the ratio of the mean values of the total multiplicities and of the number of pions per cluster. For convenience, a Gaussian distribution in $ln(n_{cl}/\langle n_{cl}\rangle + 1)$ is used rather than a binomial distribution. Its mean value is $\{16 + 0.75l - 0.31l^2\}/25$ and its *rms* value is $\{5.7 - 0.56l + 0.27l^2\}/25$ where $l = log_{10}(\sqrt{s_{eff}})$. Pions are defined to be charged or neutral at random in the ratio given in [76]. Figure 5.5 compares the charged multiplicity distributions obtained here with those of Reference 76.

The cluster rapidity distributions are chosen according to a linear combination between a rectangular plateau (weight 0.75) and a triangular plateau (weight 0.25). They are then boosted to where they belong to (in general, η_1 and η_2 are different and the central production rest frame is not at rest in the global centre of mass frame used here). A final tuning of the pion rapidities achieves exact energy momentum conservation.

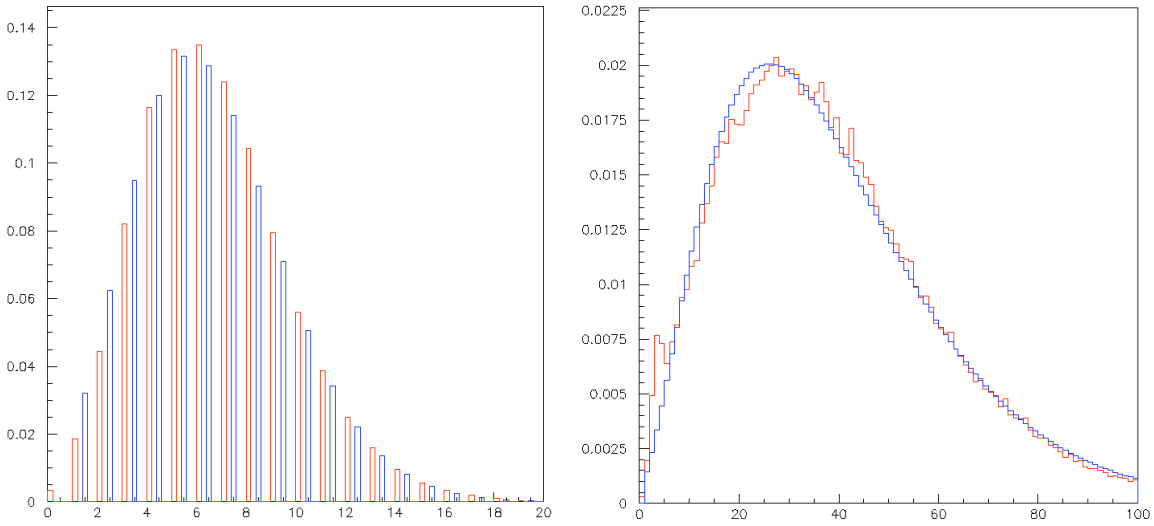

Figure 5.5: Comparison of the charged multiplicity distributions obtained here (red) with those of Reference 76 (blue). Incident proton energies are 10^2 (left) and 10^6 (right) GeV.

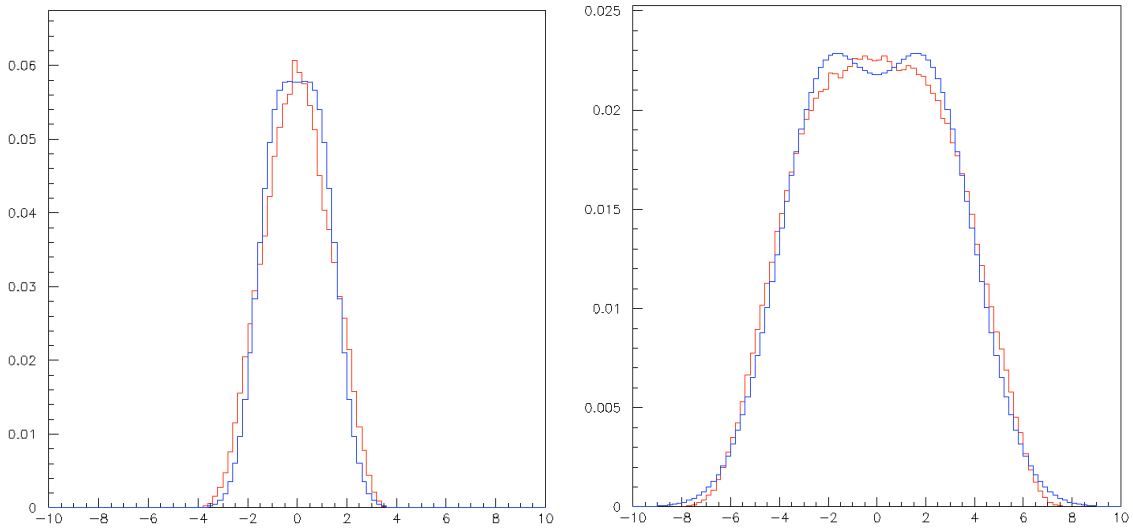

Figure 5.6: Comparison of the pion rapidity distributions obtained here (red) with those of Reference 76 (blue). Incident proton energy are 10^2 (left) and 10^6 (right) GeV.

For the time being, pion nucleon interactions are treated the same way as nucleon nucleon interactions apart from the values taken by the interaction cross section which are taken from Reference 19.

5.2 Nuclei

5.2.1 Nucleon air interactions

Nucleon-air interactions are taken to be nucleon nitrogen interactions exclusively. The volume density distribution of the nitrogen nucleus is taken of the Woods Saxon form: $\rho=1/\{1+exp[(r-r_N)/\Delta r]\}$ with $r_N = r_{0N}\ 14^{1/3}$ and Δr = 0.5 fm. The incident nucleon is taken to have a cross section $log_{10}\sigma[mb]= 1.340+0.0642log_{10}E_{inc}$ [GeV]. The radius r_{0N} is equal to 1.02 fm at an incident lab energy of $E_{inc}= 10^6$ GeV. In order to match the resulting nucleon nitrogen cross section with that quoted in Reference 19 a very small adjustment of the nitrogen radius has been made by having r_{0N} increase with E_{inc} [GeV] as $1.056-0.0292(log_{10}E_{inc})+0.0039(log_{10}E_{inc})^2$. An interaction is described by choosing an impact parameter b at random with a uniform b^2 distribution and by calculating the number $n_{wounded}$ of nitrogen nucleons contained in the cylinder of cross section σ having as axis the incident nucleon momentum. The incident nucleon is then made to interact successively with each of the $n_{wounded}$ nucleons. The pions produced in the interactions escape the nucleus without interacting further. On the contrary, the leading nucleon re-interacts $n_{wounded} - 1$ times, each time with a properly reduced energy. The nucleon nitrogen cross section is calculated as $\pi(b_{max})^2$ where b_{max} is the value of the impact parameter beyond which $n_{wounded}$ does not exceed 0.5 .

5.2.2 Iron-air interactions

An iron nucleus of incident energy E_{inc} is supposed to consist of 56 nucleons, each having an energy $E_{inc}/56$ and a momentum parallel to the incident momentum. This neglects the Fermi momentum which is of the order of the Planck constant divided by the iron radius, ~200/4=50 MeV. The distribution of the nucleons inside the iron nucleus is calculated to reproduce the Woods Saxon volume density with r_{Fe}=1.1 $56^{1/3}$ = 4.21 fm and Δr = 0.5 fm at incident lab energy of $E_{inc}= 10^6$ GeV. Correlations between nucleons are modelled with a hardcore interaction of radius 0.5 fm: namely, we make sure that the centres of two neighbour nucleons be never closer than d_0 = 1 fm from each other. In order to reproduce the energy dependence of the iron nitrogen cross section given in Reference 19, the dimensions of the iron nucleus, r_{Fe} , Δr and d_0, are made to increase with energy using a scaling law of the form: $1.031-0.0202(log_{10}E_{inc})+0.0025(log_{10}E_{inc})^2$. A library of 100 such nuclei has been produced. The match between the Woods Saxon density and that obtained here is shown in Figure 5.7. As in the case of nucleon nitrogen interactions, an impact parameter b between the centres of the two interacting nuclei is chosen at random. Each of the 56 iron nucleons is then considered in sequence. In cases where it interacts with the nitrogen nucleus, the interaction proceeds as defined in the preceding paragraph. Else, the nucleon escapes freely and will interact later on with another nitrogen nucleus independently from the other nucleons of the primary iron nucleus. The inelastic interaction cross section is again calculated as $\pi(b_{max})^2$ where b_{max} is the value of the impact parameter beyond which none of the iron nucleons interacts with the nitrogen nucleus.

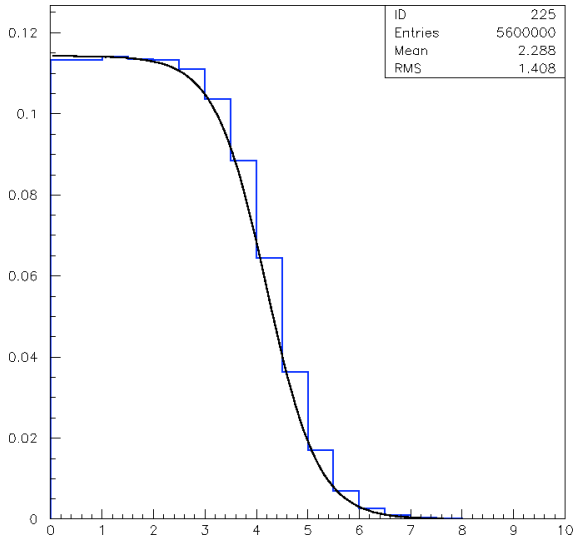

Figure 5.7: Comparison between the volume density distributions of an iron nucleus obtained from the present Monte Carlo code (histogram) and using the Woods Saxon form quoted in the text (full line).

5.2.3 Inelastic interaction cross section

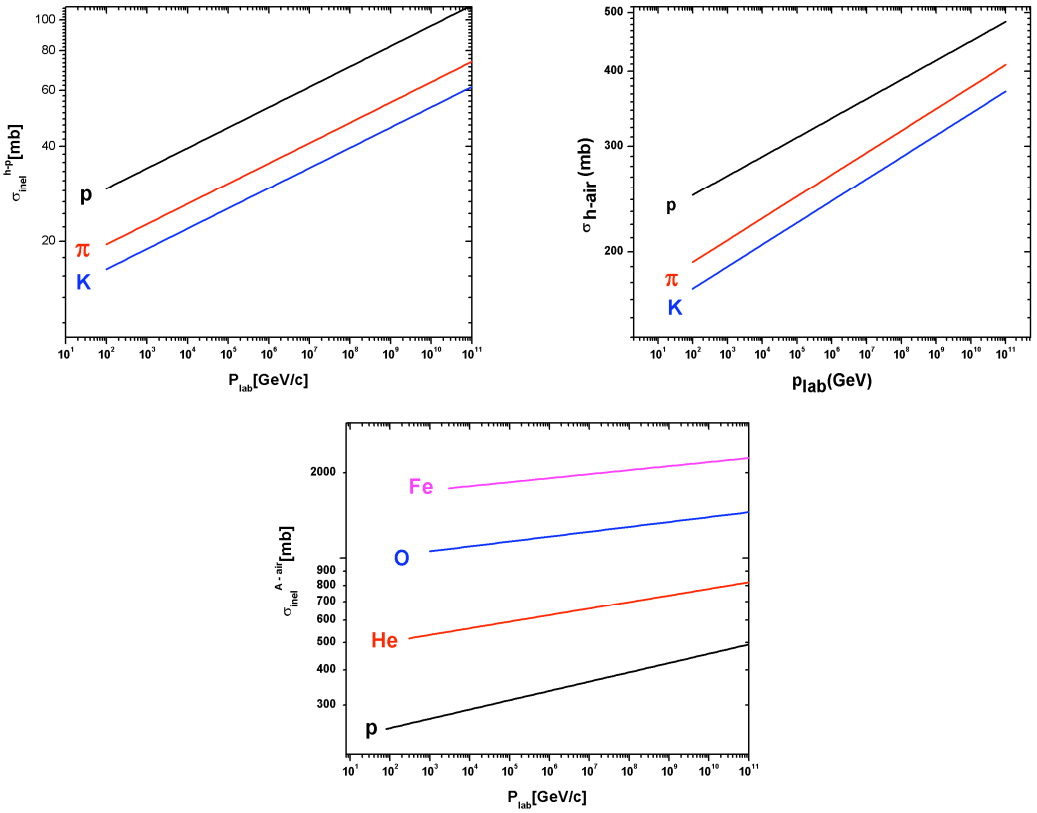

Figure 5.8: Energy dependence of inelastic cross sections as given in Reference 19. Left panel: p, π and K interacting with nucleons. Middle panel: p, π and K interacting with air. Right panel: p, He, O and Fe interacting with air.

The inelastic interaction cross sections calculated as described above are compared with those used in Reference 19. As mentioned above, small adjustments have been made in order to obtain the desired energy dependence which we recall below [19]:

Nucleon nucleon: $log_{10}\sigma\,[mb] = 1.340+0.0642\ log_{10}\,E_{inc}\,[GeV]$

Nucleon air: $log_{10}\sigma\,[mb] = 2.332+0.032\ log_{10}\,E_{inc}\,[GeV]$

Iron air: $log_{10}\sigma\,[mb] = 3.197+0.0142\ log_{10}\,E_{inc}\,[GeV]$

The data of Reference 19 of relevance to this evaluation are reproduced in Figure 5.8.

5.3. Shower development

5.3.1 Atmospheric model

An exponential dependence of the atmospheric pressure as a function of altitude of the form $p = p_0 exp(-z/\Delta z)$ has been retained. As illustrated in Figure 5.9, using Δz = 6.83 km and p_0 = 1100 g/cm^2 gives a good description of the standard atmospheric profiles mentioned in Reference 19.

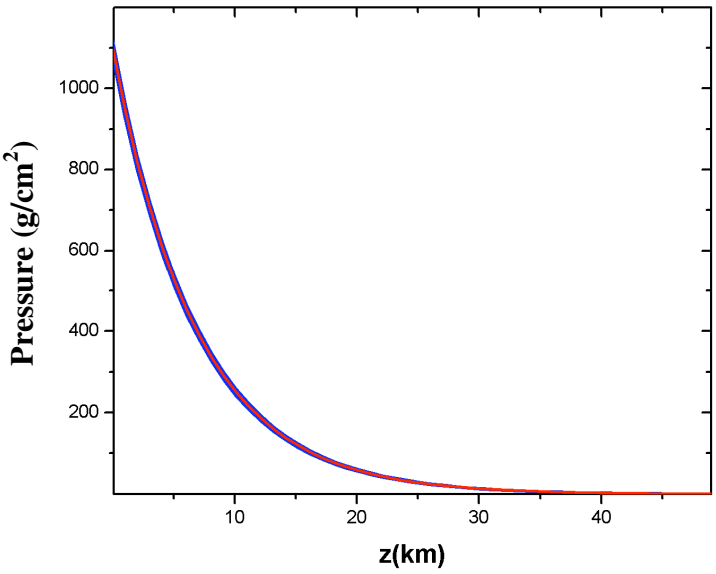

Figure 5.9: Dependence on altitude of the atmospheric pressure. The red curve is the exponential used in the present work: the blue curves are from Reference 19 for different seasons.

5.3.2 Energy losses and multiple Coulomb scattering

Two kinds of energy losses are taken into account: ionization losses and radiation losses. They are supposed to be the same when the incident energy E is equal to the critical energy E_{crit} taken as input parameter.

The differential ionization loss is taken to be 1.8 MeV g^{-1}cm^2 for $\beta\gamma$= 2. For $\beta\gamma > 2$ it increases by 0.11 MeVg^{-1}cm^2 for each unit of lnE. For $\beta\gamma < 2$ the

differential ionization loss is taken to be inversely proportional to E, therefore inversely proportional to $\gamma \approx \sqrt{(1+\beta^2\gamma^2)}$ and equal to $\sqrt{5}$ 1.8 MeV $g^{-1}cm^2 / \gamma$.

The differential radiation loss is equal to E/X^*_{rad} where X^*_{rad} is an effective radiation length. The factor $1/X^*_{rad}$ is calculated from the definition of the critical energy: $1/X^*_{rad} = 1.8\ MeV g^{-1}cm^2/E_{crit}$. The values retained for the critical energies are 74 000 GeV for protons, 1657 GeV for pions and 950 GeV for muons.

Multiple scattering in a slice of x g/cm^2 is calculated using a mean transverse momentum kick of $13.6\sqrt{(2x/X_{rad})}$ MeV where X_{rad} is the radiation length of air, 36.66 g/cm^2. Projection on two orthogonal planes containing the particle momentum gets rid of the factor $\sqrt{2}$: the transverse momentum kick in each plane is therefore taken to have a Gaussian distribution around 0 of variance $13.6\sqrt{(x/X_{rad})}$ MeV.

5.3.3 Decays

Charged pion decays are calculated in the pion cms where the decay muon has an isotropic distribution. Neutral pions are supposed to decay promptly before interacting. Note, however, that a 1.35 EeV neutral pion has a mean decay path of 250 m. At 20 km altitude, this corresponds to 1.6 gcm^{-2} compared to a collision length of 47 gcm^{-2}.

Electrons from muon decays are ignored; the muons are simply removed from the set of shower particles once they have decayed.

5.3.4 Thinning

For the time being, thinning is implemented following Hillas' method as described in Reference 78.

Let us consider the process $A \rightarrow B_1, B_2, \ldots, B_n,\ n \geq 1$
where a primary particle A generates a set of n secondaries $B_1, B_2, \ldots, B_n$. Let E_A (E_{Bi}) be the energy of A (B_i), and let E_{th} be a fixed energy called *thinning energy.*

In order to keep a secondary, the energy E_A is compared with E_{th}, and:

If $E_A \geq E_{th}$, every secondary is analyzed separately, and kept with probability

$$P = \begin{cases} 1 & \text{if } E_{Bi} \geq E_{th} \\ \dfrac{E_{Bi}}{E_{th}} & \text{if } E_{Bi} < E_{th} \end{cases}$$

If $E_A < E_{th}$ it means that the primary comes from a previous thinning operation. In this case only one of the n secondaries is kept. It is selected among all secondaries with probability

$$P = \frac{E_{Bi}}{\sum_{j=1}^{n} E_{Bj}}$$

This means that once the thinning energy is reached, the number of particles is no longer increased.

In both cases the weight of the accepted secondary particles is equal to the weight of particle A multiplied by the inverse of P_i.

In the present state of the code, thinning is applied to charged pions exclusively; nucleons are anyhow very few and neutral pions are immediately disposed of by substituting a Gaisser-Hillas profile.

In this very crude form, thinning is known to cause very large statistical fluctuations and a more refined treatment, such as used in Aires [20], will be necessary to avoid this problem.

5.4 First results

In its current state, the code is running without problem up to the highest energies (~100 EeV). Yet, it is far from being reliably usable: a running-in period will be required to perform all necessary acceptance tests, to eliminate possibly remaining minor bugs and to optimize the efficiency, in particular to refine the thinning algorithm which is presently very crude. Only then will one be able to use it for the purpose for which it has been designed.

I shall restrict the present paragraph to a few brief comments concerning the longitudinal profile and the muon density on ground.

The longitudinal profile is relatively independent from the details of the hadron dynamics. More precisely, calling Λ_{int} the interaction length, X_1 the depth of the first interaction and $X_{max}-X_1$ the depth of the shower maximum, the following relations are strictly obeyed, independently from the model used to describe shower development:

$\langle X_1\rangle=\Lambda_{int}= Rms(X_1)$, a result of the exponential distribution of X_1,

$\langle X_{max}\rangle=\langle X_{max}-X_1\rangle+\langle X_1\rangle$

$Rms(X_{max})=\{Rms^2(X_1)+Rms^2(X_{max}-X_1)\}^{1/2}=\{\Lambda^2_{int}+Rms^2(X_{max}-X_1)\}^{1/2}$.

The last relation results for the strict independence between X_1 and $X_{max}-X_1$. Taking as an example two 10^{18} eV showers, one induced by a proton and the other by an iron nucleus, the following results are obtained (units are gcm^{-2}):

Primary	Λ_{int}	$\langle X_{max}-X_1\rangle$	$Rms(X_{max}-X_1)$	$\langle X_{max}\rangle$	$Rms(X_{max})$
Proton	53	725	61	778	81
Iron	11	684	34	695	36

As can be seen from the table, the main contributions to $Rms(X_{max})$ and to $\langle X_{max}\rangle_P-\langle X_{max}\rangle_{Fe}$ are from the first interaction (Λ_{int}). The differences between proton and iron are 83 gcm^{-2} for $\langle X_{max}\rangle$ and 45 gcm^{-2} for $Rms(X_{max})$ compared with 115 gcm^{-2} and 40 gcm^{-2} respectively as predicted by common sophisticated shower simulation codes. Proton and iron elongation rates (per decade) are similar and equal to 60 gcm^{-2} for $\langle X_{max}\rangle$ and -4 gcm^{-2} for $Rms(X_{max})$ compared with 55 gcm^{-2} and -2 gcm^{-2} respectively as predicted by common codes (as shown in Figure 2.21).

The muon density on ground, calculated for muons having energy in excess of 500 MeV, is found to increase as a function of energy by a factor 13 per decade compared with 8 as predicted by common codes (as shown in Figure 2.25).

While the present results are qualitatively similar to expectation, and while the calculated shower profiles have the expected shapes, the quantitative differences with standard codes are important, in particular for what concerns the muon density on ground, and suggest that more work and more checks are necessary before gaining confidence in the reliability of the code. In particular, the muon density on ground is a much more sensitive test of the dynamics at play than the longitudinal profile: it results from a competition between the interaction length and the decay length, which both decrease with altitude, the former because of the increase of the density and the latter because of the decrease of the mean energy.

Chapter 6

SUMMARY AND CONCLUSION

The Pierre Auger Observatory has made a breakthrough in our understanding of the physics of Ultra High Energy Cosmic Rays (UHECR) by measuring the energy spectrum and revealing the GZK cut-off, by giving evidence for extragalactic counterparts and by shedding some new light on the mass composition. The present work has made contributions to the latter of these topics, which, to a large extent, remains an open question. It is inscribed in a collaborative effort of the PAO collaboration. In the recent years, major progress has been achieved in the analysis of FD data – mean value and *rms* deviation from the mean of the elongation rate – with results consistent with the predictions of hadronic models, providing evidence for a transition from proton-like to iron-like primaries over the energy range covered by the PAO. The same conclusion has been reached, with lesser accuracy, by the analysis of the azimuthal risetime asymmetry in the SD. Yet, SD analyses that are sensitive to the amplitude of the muon density on ground can only be made consistent (barely) with the predictions of hadronic models at the price of a 30% increase of the energy scale.

The present study has focused on this apparent mismatch. In a first part, it has performed a detailed analysis of the jump method, of its discriminating power and of its comparison with other possible discriminators associated with the muon density on ground.

A brief introduction was used to get some familiarity with the relation between the total jump and the properties of the FADC trace, showing in particular that in order to have a chance to learn something sensible about the number of muons contributing to an FADC trace, it was necessary to restrict the observation to tanks not too close to the shower axis. The correlation between the number of muons, the value of the total jump and the total charge of the FADC trace was scrutinized. From the study of the separation which could be expected from a measurement of the total jump between a sample of tanks detecting proton induced showers and a sample of tanks detecting iron induced showers, it was remarked that the iron-proton separation could in no case exceed 30%, providing a measure of the correlation between the nature of the primary and the density of muons on ground. This result implies that to make a statement on the identity of the primaries to three standard deviations requires a sample of at least 50 tanks. It was also remarked that if the energy of the primary were known, not only the value of the total jump but also the total charge and the number of jumps in the trace would be equally good proton-iron discriminators.

A major difficulty was identified as resulting from our ignorance of the energy of the primary, the difficulty to tell the difference between, say, two proton showers of different energies and proton and iron showers of the same energy. In order to overcome this difficulty, an energy-independent discriminator – the ratio of the jump to the total charge – has been used and the analysis has been restricted to tanks located within a range of distances to the shower axis depending on *S(1000)*,

(the quantity used as energy estimator). The method was shown to be successful on simulated events and applied to real PAO data, confirming the mismatch with the predictions of shower model simulations and showing that it cannot be resolved by a simple rescaling of the relation between *S(1000)* and energy. A possible cause of such a mismatch might be the inadequacy of hadronic models to reproduce the lateral distribution function of muons. Another possible cause might be the inadequacy of the detector simulation to describe the response to muons. The former of these is addressed in the second part of the present work, after having presented a jump analysis applied to UHECRs associated with Cen A that favours a proton origin.

Having illustrated the difficulty to identify the nature of the primary using SD data, the lack of consistency between data and simulation is a concern and more work is required to sort it out. One cannot be satisfied with blaming the models used in the simulation unless the physics mechanism of relevance is clearly understood. The sophisticated codes traditionally used to simulate shower development lack transparency and make it difficult to identify the phenomena of relevance. The second part of the present work is a step toward the development of a very crude, but transparent shower development simulation, in the hope that it could help us with the understanding of such phenomena.

Dealing with the electromagnetic component of the shower is relatively easy: to an excellent approximation, it is sufficient to consider bremsstrahlung and pair creation as exclusive elementary processes, to ignore any particle other than electrons, positrons and photons and to model simply ionization losses. Such simplicity allows for a straightforward treatment of the longitudinal development that has been presented and discussed in some detail. Parameterizations of the shower profile as a function of the energy of the primary, both mean values and *rms* fluctuations, have been given using a Gaisser-Hillas form. Three types of primaries have been considered: electrons, photons and neutral pions. The model allows to deal simply with very high energy showers. Applications to the Landau-Pomeranchuk-Migdal effect and to the Perkins effect have been presented as illustrations, with the result that both are nearly negligible in practice.

The development of the hadronic component of the shower is much more difficult to handle. It implies the production of mesons, mostly pions, the fate of which is governed by two competing processes: hadronic interactions with the atmosphere nuclei and weak decays into muons. The scales governing these two processes are different: the interaction cross-section depends weakly on energy but the interaction rate depends on atmospheric pressure, namely on altitude; on the contrary, the decay rate is independent of altitude but inversely proportional to energy, a result of Lorentz time expansion. This prevents using the iterative method that was shown to be so efficient in the electromagnetic case where a single scale, the radiation length, governs the dynamics.

The main problem in extrapolating accelerator data to UHECR showers is not so much energy than rapidity. Indeed 20 EeV in the lab correspond to 200 TeV in the cms, only two orders of magnitude above Tevatron energies and only one above LHC energies. The slow logs evolution of hadronic physics makes it unlikely that an extrapolation of lower energy collider data to the UHECR range be very

wrong. But in terms of rapidity, UHECR showers are dominated by forward production, a region that is inaccessible to collider data. In particular, no accurate measurement exists of the inelasticities and of the shape of the fall of the rapidity plateau, both of which are of utmost relevance to the development of UHECR showers. The model developed in the present work takes inelasticity as an adjustable parameter and the shape of the rapidity plateau is accessible in a transparent way.

Particular attention is devoted to features that allow for an identification of the primary, proton or iron. This concerns essentially the first interaction: once the primary nucleus has interacted, shower development involves only nucleon-air and meson-air interactions. Again, there exist no collider data on nuclei interactions in the relevant energy range and subsequent interactions involve pion-nuclei for which there exist no collider data. The very simple descriptions used in the present simulation allow for a transparent access to the parameters of relevance.

The presentation given here limits its ambition to a description and discussion of the simulation, leaving the study of muon densities on ground for a later phase. The emphasis is to show that the tool that has been developed is well suited to the task but performing the task is beyond the scope of the present thesis and will be the subject of future work.

References

[1] F.A. Aharonian *et al.*, Nature 432 (2004) 75;
F.A. Aharonian *et al.* (H.E.S.S. Col laboration) A&A 449 (2006) 223.
[2] Y. Uchiyama *et al.*, Nature 449 (2007) 576.
[3] E.G. Berezhko and H.J. Völk, A&A 419 (2004) L27.
[4] L.O'C. Drury, Rep. Prog. Phys. 46 (1983) 973;
R.D. Blandford and D. Eichler, Phys. Rept. 154 (1987) 1;
F.C. Jones and D.C. Ellison, Sp. Sc. Rev. 58 (1991) 259;
L.O'C. Drury, Contemp. Phys., 35 (1994) 232;
K. Greisen, Proc. 9th ICRC, 2 (1965) 609;
A.M. Hillas, Ann. Rev. Astron. Astrophys., 22 (1984) 425.
[5] The Pierre Auger Project Design Report, The Auger Collaboration, 2nd Edition, Fermi Laboratory, November 1996, Revised March 1997.
http://www.auger.org/admin/DesignReport/index.html
[6] J. Abraham *et al.*, Nucl. Instrum. Meth. A523 (2004) 50.
[7] R. Engel, presented at 40th Rencontres de Moriond, Italy (2005).
[8] A.M. Hillas, Proc. 17th ICRC, 8 (1981) 193.
[9] B. Dawson [Pierre Auger Collaboration], Proc. 30th ICRC, Merida, (2007) #0976, arXiv:astro-ph/0706.1105.
[10] D. Bird *et al.*, Nucl. Inst. Meth., A349 (1994) 592;
D. Bird *et al.*, Astrophys. J. 424 (1994) 491.
[11] T.K. Gaisser and A.M. Hillas, Proc. 15th ICRC, 8 (1977) 353.
[12] J. Linsley and L. Scarsi, Phys. Rev. 128 (1962) 2384;
J. Linsley, L. Scarsi and B. Rossi, Phys. Rev. Lett. 6 (1961) 458.
[13] M. Ave [Pierre Auger Collaboration], Proc. 30th ICRC, 4 (2007) 307.
[14] A.K. Tripathi, Nucl. Instr. and Meth. A 504 (2003) 1;
P. Ranin *et al.*, UCLA-Cosmic/2001-02;
A. Tripathi *et al.*, UCLA-Cosmic/2001-02 and GAP note 2002-013.
[15] S. Agostinelli *et al.*, Nucl. Instrum. Meth. A506 (2003) 250;
J. Allison *et al.*, IEEE Trans. Nucl. Sci. 53 (2006) 270.
[16] C. Pryke, GAP note 1996-008;
C. Pryke, Auger internal GAP note 1997-004;
T. McCauley and T. Paul, GAP note 2000-055;
W.E. Slater, A. Tripathi and K. Arisaka, GAP 2002-063;
T. Ohnuki, G. Rodriguez-Fernandez, D. Barnhill, A. Tripathi, T. McCauley and T.K. Arisaka, GAP note 2004-043;
M. Zha and J. Knapp, GAP note 2005-031;
A. Creusot and D. Veberic, GAP note 2007-073.
[17] N. Kalmykov, S. Ostapchenko and A. Pavlov, Nucl. Phys. Proc. Suppl. B52 (1997)17;
S. Ostapchenko, Phys. Rev. D74 (2006) 014026;
S. Ostapchenko, Nucl. Phys. Proc. Suppl. 151 (2006) 143;
S. Ostapchenko, Phys. Lett. B636 (2006) 40;
G. Battistoni *et al.*, AIP Conf. Proc. 896 (2007) 31.

[18] R. Engel, T. Gaisser, T. Stanev, and P. Lipari, Proc. 26th ICRC, 1 (1999) 415;
R. Fletcher, T. Gaisser, P. Lipari, and T. Stanev, Phys. Rev. D50 (1994) 5710;
K. Werner and T. Pierog, AIP Conf. Proc. 928, 111 (2007), arXiv:0707.3330.
[19] D. Heck *et al., Corsika: a Monte Carlo code to simulate extensive air showers*, Forschungszentrum Karlsruhe, Wissenschaftliche Berichte FZKA 6019 (1998).
[20] S. Sciutto, AIRES. http://www.fisica.unlp.edu.ar/auger/aires .
[21] K. Greisen, Phys. Rev. Lett. 16 (1966) 748;
G. Zatsepin and V. Kuzmin, JETP Lett. 4 (1966) 78.
[22] F. Shussler [Pierre Auger Collaboration], Proc. 31th ICRC, Lodz, Poland, 2009.
[23] R. U. Abbasi *et al.*, Phys. Rev. Lett., 100 (2008) 101101;
R. U. Abbasi *et al.*, Phys. Lett., B619 (2005) 271.
[24] J. Abraham *et al.* [Pierre Auger Collaboration], Astropart. Phys. 29 (2008) 188;
J. Abraham *et al.* [Pierre Auger Collaboration], Science 318. no. 5852 (2007) 938.
[25] J.D. Hague [Pierre Auger Collaboration], Proc. 31th ICRC, Lodz, Poland, 2009.
[26] M.P. Veron-Cetty and P. Veron, Astron. Astrophys. 455 (2006) 773.
[27] D. De Marco and T. Stanev, Phys. Rev. D72 (2005) 081301;
T. Wibig and A. W. Wolfendale, J. Phys. G31 (2005) 255.
[28] D. Allard, E. Parizot, and A. Olinto, Astropart. Phys. 27 (2007) 61, astro-ph/0512345.
[29] V. Berezinsky, S. Grigoreva, and B. Hnatyk, Nucl. Phys. Proc. Suppl. 151 (2006) 497.
[30] R.J. Glauber and G. Matthiae, Nucl. Phys. B21 (1970) 135;
K.G. Boreskov and A.B. Kaidalov, Sov. J. Nucl. Phys. 48 (1988) 367.
[31] T.K. Gaisser *et al.*, Proc. 16th ICRC 9 (1979) 258;
T.K. Gaisser *et al.*, Phys. Rev. D47 (1993) 1919;
J. Linsley and A.A. Watson, Phys. Rev. Lett. 46 (1981) 459;
J. Matthews, Astropart. Phys. 22 (2005) 387;
W. Heitler, "The Quantum Theory of Radiation", Oxford University Press, 1954.
[32] C. Bonifazi *et al.* [Pierre Auger Collaboration], Nucl. Phys. Proc. Suppl. 190 (2009) 20, arXiv:0901.3138.
[33] M. Unger *et al.*, Nucl. Instrum. Meth. A 588 (2008) 433.
[34] J. Abraham *et al.* [Pierre Auger Collaboration], Physical Review Letters 104 (2010) 091101.
[35] T. Bergmann *et al.*, Astropart. Phys. 26 (2007) 420.
[36] R. Walker & A.A. Watson, J. Phys. G7 (1981) 1279.
[37] D. Newton *et al.*, Astropart. Phys. 26 (2007) 414.
[38] H. Wahlberg [Pierre Auger Collaboration], Proc. 31th ICRC, Lodz, Poland, 2009.
[39] X. Bertou and P. Biloir, GAP note 2000-017;
X. Bertou, P.D. Silva and P. Biloir, GAP note 2002-074.
[40] M. Healy [Pierre Auger Collaboration], Proc. 30th ICRC, 4 (2007) 377.
[41] F. Schmidt *et al.*, Astropart. Phys. 29 (2008) 355.

[42] A. Castellina [Pierre Auger Collaboration], Proc. 31th ICRC, Lodz, Poland, 2009.
[43] P.N. Diep, VATLY internal note nr 33, "More on the jump method", August, 2009.
[44] J. Abraham *et al.* (Auger Collaboration), *Correlation of the highest energy cosmic rays with nearby extra-galactic objects*, Science 318 (2007) 938.
[45] M. Unger (Pierre Auger Collaboration), Proc. 30th ICRC (2007). See also Tere Dova's Power Point summary in preparation for the 2008 Lamar meeting.
[46] The Auger Collaboration, *The Pierre Auger Observatory Design Report*, 14 March 1997.
[47] X. Garrido *et al.*, GAP note 2007-060.
[48] Antonio Insolia, private communication.
[49] P. Billoir and P.T. Nhung, GAP note 2007-131 and references therein.
[50] A. Chou *et al.*, FNAL, GAP note 2004-057;
H. Salazar and L. Villasenor, GAP note 2005-043;
M. Ave *et al.*, GAP notes 2007-021 and 2007-051;
G. Navarra and A. Castellina, GAP notes 2006-065 and 2007-126.
[51] R. Engel [Pierre Auger Collaboration], Proc. 30th Int. Cosmic Ray Conf., Merida (2007) vol. 4, p. 377, and references therein;
M. Healy [Pierre Auger Collaboration], Proc. 30th Int. Cosmic Ray Conf., Merida (2007) vol. 4, p. 377, and references therein.
[52] A. Castellina [Pierre Auger Collaboration], Proc. 31st Int. Cosmic Ray Conf., Lódz (2009), *Comparison of data from the Pierre Auger Observatory with predictions from air shower simulations: testing models of hadronic interactions.*
[53] Data produced by X. Garrido from the Auger LAL-Orsay group and saved at Lyon in the following directory: /afs/in2p3.fr/group/pauger/users17/garrido/XSectLib/.
[54] VATLY internal note 25.
[55] J. Bellido [Pierre Auger Collaboration], Proc. 31st Int. Cosmic Ray Conf., Lódz (2009), *Measurement of the average depth of shower maximum and its fluctuations with the Pierre Auger Observatory*.
J. Abraham *et al.* [Pierre Auger Collaboration], Physical Review Letters 104 (2010) 091101.
[56] X. Garrido *et al.*, GAP note 2009-023.
[57] P.N. Diep, VATLY notes 27 (2008) and 33 (2009), GAP note 2008-136.
[58] J. Abraham *et al.* [Pierre Auger Collaboration], Nuclear Instruments and Methods, A523 (2004) 50.
D. Veberic and M. Roth Offline team, Offline reference manual, 2009 (based on GAP note 2005-035).
[59] X. Garrido, private communication.
[60] D. Semikoz, GAP notes 2008-091 and 092.
[61] D. Nosek *et al.*, GAP note 2010-007.
[62] H. Lyberis *et al.*, GAP note 2010-072.
[63] Nosek and Jana Nonosková, GAP note 2009-145.

[64] P.N. Diep, VATLY Internal note 21, December 2008 and references therein.
[65] Particle Data Group, S. Eidelman, *et al.*, Physics Letters B592 (2004) 1;
[66] P. Sokolsky, Am. Inst. Phys. Conf. Proc. 433 (1998) 65.
[67] L.Alio *et al.*, Comm. Phys. Vietnam, 2 (2010) 181.
[68] L.D. Landau and I.J. Pomeranchuk, Dokl. Akad. Nauk. SSSR 92 535 (1953); Dokl. Akad. Nauk. SSSR 92, 735. These papers are available in English in The Collected Papers of L. D. Landau, Pergamon Press, 1965;
A.B. Migdal, Phys. Rev. 103, 1811 (1956).
[69] P. L. Anthony *et al.*, Phys. Rev. Lett. 75 (1995) 1949.
[70] S. R. Klein, LBNL 41167, December 1997, arXiv:astro-ph/9712198v3 11 Dec 2000 and references therein.
[71] J. Abraham *et al.* [Pierre Auger Collaboration], Astrop. Phys. 31 (2009) 399.
[72] P.N. Diep and D. T. Hoai, *Reduced ionization from very high energy eklectron positron pairs,* VATLY Internal Note 35, October 2009.
[73] D.H. Perkins, Phil. Mag. 46 (1955) 1146.
[74] J. Iwadare, Phil. Mag. 3:31 (1958) 680.
[75] M. Urban, private communication.
[76] J.N. Capdevielle, J. Phys. G : Nucl. Part. Phys. 15 (1989) 909.
[77] G.J. Alner *et al.*, UA5 Collaboration, Phys. Rep. 154 (1987) 247.
[78] A. M. Hillas, *Nucl. Phys. B (Proc. Suppl.),* 52B, 29 (1997);
A. M. Hillas, *Proc. 19th ICRC (La Jolla),* 1, 155 (1985);
A. M. Hillas, *Proc. of the Paris Workshop on Cascade simulations,* J. Linsley and A. M. Hillas (eds.), p 39 (1981).